MODEL PREDICTIVE CONTROL OF HIGH-POWER WIND POWER CONVERTER: CONTROL DESIGN, STABILITY, AND IMPLEMENTATION

Lago, Pedro Catalán

DOI (link to publication from Publisher):
10.54337/aau747736361

Publication date:
2024

Document Version
Publisher's PDF, also known as Version of record

MODEL PREDICTIVE CONTROL OF HIGH-POWER WIND POWER CONVERTER: CONTROL DESIGN, STABILITY, AND IMPLEMENTATION

BY
PEDRO CATALÁN

PhD Thesis 2024

AALBORG UNIVERSITY
DENMARK

MODEL PREDICTIVE CONTROL OF HIGH-POWER WIND POWER CONVERTER: CONTROL DESIGN, STABILITY, AND IMPLEMENTATION

by

Pedro Catalán

AALBORG UNIVERSITY
DENMARK

PhD Thesis 2024

Submitted: May 2024

Main Supervisor: Professor Zhe Chen
Aalborg University

Co-supervisor: Associate Professor Yanbo Wang
Aalborg University

Assessment: Associate Professor Sanjay Kumar Chaudhary (Chair)
Aalborg University, Denmark

Professor Jose Rodriguez
Universidad San Sebastian, Chile

Associate Professor Sergio Vázquez Pérez
Universidad de Sevilla, Spain

PhD Series: Faculty of Engineering and Science, Aalborg University

Department: AAU Energy

ISSN: 2446-1636
ISBN: 978-87-94563-89-5

Published by:
Aalborg University Open Publishing
Kroghstræde 1-3
DK – 9220 Aalborg Øst
aauopen@aau.dk

Printed in Denmark by Stibo Complete, 2024

CURRICULUM VITAE

Pedro Catalán received the M.Sc. degree in telecommunications engineering from the University of the Basque Country, Bilbao, Spain, in 2007, and the professional master's degree in electrical energy from Mondragon University, Mondragon, Spain, in 2012. He is currently working toward the PhD degree in power electronic systems with the Department of Energy Technology, Aalborg University, Aalborg, Denmark.

Since 2007, he has been working for Ingeteam Power Technology S.A., Zamudio, Spain, where he developed embedded software for power converters in wind business division, comprising analysis, modelling, and validation of control structures for grid-connected VSCs, synchronization methods, grid code compliances, current controllers and stability assessment methods. His current research interests include offshore wind power, advanced control structures, and grid-friendly functionalities for high-power converters.

ENGLISH SUMMARY

The increase in wind energy utilization, particularly emerging offshore wind power generation, promotes the revolution of wind turbine toward high-power application. To exploit the offshore wind energy in an efficient and cost-effective way, the application of high-power wind turbine is being paid the increasing concerns. The development of high-power wind turbine undoubtedly poses new technical challenges. More complex power conversion architectures and advanced control strategies are then essential to ensure the secure and stable integration of high-power wind turbine into power system. The three-level Neutral Point Clamped (3L-NPC) converter has been developed as an attractive solution for high-power Wind Energy Conversion Systems (WECS). The 3L-NPC enables high-voltage operation and generates voltage waveforms of three levels, which increases the power rating and leads to reduced cabling and harmonic filter requirements. Meanwhile, Finite Control Set Model Predictive Control (FCS-MPC) has gained attention as an advanced control strategy appropriate for high-power converters. For instance, MPC exhibits fast dynamic response compared with classical linear controllers. Further, it is characterized by a straightforward design to address non-linear characteristics and to realize multiple control objectives within a single control loop. However, the technology readiness assessment of predictive control techniques in high-power wind power converter has not been fully reached.

The goal of this Industrial PhD Project is to develop a new FCS-MPC strategy, address the technical challenges for high-power operation, and investigate its implementation into Ingeteam commercialized power converter solution. This Industrial PhD Project investigates the application of FCS-MPC in 3L-NPC converter, and further analyzes its merits and design intricacies. The main work of this thesis is as follows. **Chapter 1** introduces the background and motivation. **Chapter 2** presents the proposed FCS-MPC strategy for grid-side control of 3L-NPC. The online tuning method for switching frequency control is proposed, and its capability to effectively regulate switching frequency during different grid conditions and transient operation is demonstrated. Furthermore, fault ride-through capability of 3L-NPC operated with FCS-MPC is developed, and compliance with most recent grid codes requirements in terms of reactive current provision during grid faults is validated. The robustness analysis of FCS-MPC is also performed, where MPC exhibits sensitivity to filter parameter mismatch. The robust FCS-MPC scheme is then proposed, where the MPC is augmented with state observer to identify grid filter parameters and enhance controller performance against parametric uncertainties or variations. **Chapter 3** analyzes stability of grid-connected 3L-NPC inverter with MPC. The frequency-scan

technique is proposed to obtain impedance characteristic under different controller design and operating conditions. The FCS-MPC shows an inherent capability to operate at low switching frequency with minimum control delay, which is advantageous for stability enhancement. Further, the offshore wind farm simulation model is developed, and the capability of proposed MPC strategy to mitigate instability phenomena is revealed. **Chapter 4** implements the proposed control strategy into Ingeteam power converter solution. The implementation of FCS-MPC framework into software package and converter control unit (CCU) is performed. Inherent intricacies of real-time implementation are addressed. An efficient implementation of FCS-MPC algorithm which reduces the number of candidate vectors is employed to optimize computational burden. Finally, the suitable performance of entire power converter solution of two paralleled active NPC (ANPC) conversion lines is verified by means of software-in-the-loop (SiL) and hardware-in-the-loop (HiL) validation. Main conclusions of this PhD Project are drawn, and future research topics are discussed in **Chapter 5**.

The main contributions of this PhD Thesis are summarized as follows. (1) An advanced FCS-MPC strategy is developed for high-power 3L-NPC converter, which ensures compliance with grid code specifications and demonstrates robustness, (2) The stability of 3L-NPC inverter with FCS-MPC is investigated, showcasing benefits of reduced sampling time for stability enhancement, (3) The proposed FCS-MPC strategy is implemented into Ingeteam commercialized power converter solution, which addresses the real-time implementation challenges in terms of industrial application. This PhD Project improves the operation performance of high-power wind power converters, enhances stability of offshore power system, and achieves a significant step forward in FCS-MPC industrial assessment.

DANSK RESUME

Stigningen i udnyttelsen af vindenergi og især den nye havmølle vindproduktion fremmer vindmøllernes revolution i retning af højeffektanvendelse. For at udnytte vindenergien på hav på en effektiv og omkostningseffektiv måde, bliver anvendelsen af højeffekt vindmøller en attraktiv løsning. Udviklingen af vindmøller med høj effekt giver uden tvivl nye tekniske udfordringer. Mere komplekse effekt-konverterings arkitekturer og avancerede kontrolstrategier er så afgørende for at sikre en sikker og stabil tilslutning af højeffekt vindmøller til elnettet. Tre-niveaus Neutral Point Clamped (3L-NPC) konverter er blevet udviklet som en attraktiv løsning til højeffekt vindenergi konverteringssystemer (WECS). 3L-NPC muliggør højspændingsdrift og genererer spændingsbølgeformer på tre niveauer, hvilket øger den nominelle effekt og fører til reducerede krav til kabelføring og harmoniske filter. I mellemtiden har Finite Control Set Model Predictive Control (FCS-MPC) fået opmærksomhed som en avanceret kontrolstrategi, der passer til højeffekt konvertere. For eksempel udviser MPC hurtig dynamisk respons sammenlignet med klassiske lineære kontrollere. Yderligere er det karakteriseret ved et ligetil design til at identificerer ikke-lineære karakteristika og til at realisere flere kontrol inden for en enkelt kontrolsløjfe. Imidlertid er vurderingen af teknologisk parathed af prædiktive styringsteknikker i højeffekts konverter ikke helt tilgængelige.

Målet med dette ErhvervsPhD-projekt er at udvikle en ny FCS-MPC-strategi, identificere de tekniske udfordringer for højeffekt drift og undersøge dens implementering i Ingeteam kommercialiseret effektkonverter løsning. Dette erhvervs PhD-projekt undersøger anvendelsen af FCS-MPC i 3L-NPC-konverter og analyserer yderligere dets fordele og designforviklinger. Hovedarbejdet i denne afhandling er som følger. **Kapitel 1** introducerer baggrunden og motivationen. **Kapitel 2** præsenterer den foreslåede FCS-MPC-strategi for styring af 3L-NPC på nettet. Online tuning-metoden til at skifte frekvensstyring er foreslået, og dens evne til at regulere koblingsfrekvensen effektivt under forskellige netforhold og transient drift er demonstreret. Ydermere udvikles kapaciteten af dynamisk spændingsvariation af 3L-NPC drevet med FCS-MPC, og overholdelse af moderne netkoders krav med hensyn til reaktiv strømforsyning under fejl er valideret. Robusthedsanalysen af FCS-MPC udføres også, hvor MPC udviser følsomhed over for filter parameter mismatch. Det robuste FCS-MPC-skema foreslås derefter, hvor MPC'en udvides med tilstandsobservatør for at identificere filter parametre og forbedre controllerens ydeevne mod parametriske usikkerheder eller variationer. **Kapitel 3** analyserer stabiliteten af nettilsluttet 3L-NPC inverter med MPC. Frekvensscanningsteknikken foreslås for at opnå impedans karakteristik under forskellige kontroller design og

driftsbetingelser. FCS-MPC viser en evne til at fungere ved lav koblingsfrekvens med minimal kontrol forsinkelse, hvilket er fordelagtigt for stabilitetsforbedring. Yderligere udvikles simuleringsmodellen for havvindmølleparker, og den foreslåede MPC-strategis evne til at afbøde ustabilitetsfænomener afsløres. **Kapitel 4** implementerer den foreslåede kontrolstrategi i Ingeteam Power Converter Solution. Implementeringen af FCS-MPC ramme i softwarepakke og konverter kontrol enhed (CCU) udføres. Forviklinger af realtids implementering behandles. En effektiv implementering af FCS-MPC-algoritme, som reducerer antallet af kandidat vektorer, anvendes til at optimere beregningsevne. Endelig verificeres den passende ydeevne af hele konverterings løsningen af to parallelle aktive NPC (ANPC) konverteringslinjer ved hjælp af software-in-the-loop (SiL) og hardware-in-the-loop (HiL) validering. Hovedopgaver af dette PhD-projekt er konkluderet, og fremtidige forskningsemner diskuteres i **Kapitel 5**.

Hovedbidragene i denne ph.d.-afhandling er opsummeret som følger. (1) En avanceret FCS-MPC-strategi er udviklet til højeffekts 3L-NPC-konverter, som sikrer overholdelse af netkodes specifikationer og demonstrerer robusthed, (2) Stabiliteten af 3L-NPC-inverter med FCS-MPC er undersøgt, hvilket viser fordele af reduceret samplingtid til stabilitetsforbedring, (3) Den foreslåede FCS-MPC-strategi er implementeret i kommercialiserede Ingeteams Power Converter Solution, som identificere implementerings udfordringerne i realtid med hensyn til industriel anvendelse. Dette PhD-projekt forbedrer drifts evnen af vindmølles konverter med høj effekt, forbedrer stabiliteten af havmølleparker og etablerer et væsentligt skridt fremad i FCS-MPC industriel evaluering.

ACKNOWLEDGEMENTS

The work presented in this dissertation is a summary of the Industrial PhD Project "Model Predictive Control of High-Power Wind Power Converter: Control Design, Stability, and Implementation," conducted at AAU Energy, Aalborg University. This Industrial PhD Project is supported by Ingeteam Power Technology. I would like to express my sincere gratitude to the above-mentioned institutions.

Special appreciation goes to my supervisor, Prof. Zhe Chen, and co-supervisor, Associate Prof. Yanbo Wang, along with company supervisor Joseba Arza from Ingeteam, for their unwavering dedication, guidance, and invaluable insights throughout my research journey. Thank you for the encouragement and motivation that helped me to complete this PhD Project.

I extend my thanks to Prof. Gonzalo Abad and Carlos Ruiz from Mondragon University for their cooperation and constructive comments on my research work. My appreciation also goes to the assessment committee for the PhD defense.

I am grateful to my colleagues at Ingeteam and AAU Energy for their continuous support during my PhD, with special mention to Qi, Danel, Joel, Eduardo, David, and Ignacio for their contributions and assistance during experimental validation.

Lastly, I want to express my deepest appreciation to my family and friends for their unwavering support and understanding throughout this academic pursuit.

"Sometimes going all the way is just a start."

Pedro Catalán
Ingeteam Power Technology, April 2024

Table of Contents

Table of Figures

ABBREVIATIONS

3L-ANPC	three-level active neutral-point-clamped
3L-NPC	three-level neutral-point-clamped
ATC	active thermal control
BPM	Basic Power Modules
CCU	converter control unit
CL	conversion line
DIBS	discrete-interval binary sequence
DLL	dynamic-link library
DSOGI	dual second order generalized integrator
DSP	digital signal processor
EKF	extended Kalman filter
EMT	electromagnetic-transient
FCS-MPC	finite control set model predictive control
FFT	Fast Fourier Transform
FPGA	field-programmable gate array
FPNSC	flexible positive and negative sequence control
FQSG	filtered quadrature signal generator
FRT	fault ride-through
GCI	grid-connected inverter
HiL	hardware-in-the-loop
HVRT	high-voltage ride-through
IGBT	insulated-gate bipolar transistor
LOS	loss of synchronism
LUT	look-up table
LVRT	low-voltage ride-through
MP^3C	model predictive pulse pattern control
MPC	model predictive control

NP	neutral-point
OPP	optimized pulse patterns
OSS-MPC	optimal switching sequence model predictive control
OWPP	offshore wind power plant
PCC	point of common coupling
PI	proportional-integral
PLC	programmable logic controller
PLL	phase-locked loop
PMSG	permanent magnet synchronous generator
PMM	power management module
PRBS	pseudo-random binary sequence
PWM	pulse width modulation
SCR	short circuit ratio
SHE	selective harmonic elimination
SiL	software-in-the-loop
SRF-PLL	synchronous reference frame phase-locked loop
SVM	space vector modulation
THD	total harmonic distortion
WECS	wind energy conversion system
WT	wind turbine

SYMBOLS

Variables

P_N	Rated active power
V_g	Rated voltage
v_g	Grid voltage
i	Grid-injected current
v_o	Power converter output voltage
s_{a1}, s_{b1}, s_{c1}	External *abc*-switching signals
s_{a2}, s_{b2}, s_{c2}	Internal *abc*-switching signals
v_{C1}, v_{C2}	DC-link capacitors voltage
i_{C1}, i_{C2}	DC-link capacitors current
i_{DC}, i_P, i_Z	DC branch currents
L_f, R_f	Grid filter inductance and resistance values
T_s	Sampling time
k	Sampling instant
V_{dc}	DC-link rated voltage
V_{BC_on}	Braking chopper switch-on voltage
V_{BC_off}	Braking chopper switch-off voltage
BC	Braking chopper activation order
R_{BC}	Braking chopper resistor
i_{BC1}, i_{BC2}	Braking chopper currents
I_{max}	Power converter maximum output current
I^+_{QMax}	Power converter maximum output current
$\|I\|$	Current vector magnitude
k	Reactive current injection gain
$\Delta\|v\|$	Voltage deviation
$limI$	Current limit
$\|U\|$	Power converter output voltage vector magnitude

J	Cost function of MPC controller
J_i	Cost of current control
λ_{dc}	Weight for current control
J_{dc}	Cost of neutral-point balance
λ_{dc}	Weight for neutral point balance
J_{sw}	Cost of average switching frequency control
λ_{sw}	Weight for average switching frequency control
f_{sw}	Switching frequency
T_w	Time length of sliding window for average switching frequency calculation
N_{sw}	Cumulative sum of switching actions in T_w
s_i	Switching state
ω	Angular frequency
θ_{PLL}	Grid voltage angle determined by PLL
ω_{PLL}	Grid voltage frequency determined by PLL
k_{FQSG}	Damping factor of the FQSG
k_{pPLL}, T_{iPLL}	Proportional gain and integral time of PLL tuning
P_0	Fundamental component of active power
Q_0	Fundamental component of reactive power
σ_L	Uncertain component of L_f
σ_R	Uncertain component of R_f
F_{k-1}	Partial derivative matrix
P_k	Error covariance matrix
H_k	Jacobian matrix
K_k	Kalman gain
$Z_{S_{dq}}$	Source impedance matrix in dq-domain
$Z_{L_{dq}}$	Load impedance matrix in dq-domain
$Y_{L_{dq}}$	Load admitance matrix in dq-domain
V_{inj}	Voltage disturbance injection
I_{inj}	Current response excited by V_{inj}

$Z_{conv}(j\omega)$	Measured power converter impedance
$Z_{conv}^{H}(j\omega)$	Complex-conjugate transpose (Hermitian transpose) of $Z_{conv}(j\omega)$
P_{sw}	Switching loss
P_{cond}	Conduction loss
T_j	Junction temperature

Subscript

P	Active component
Q	Reactive component
ref	Reference value
α	α-axis component
β	β-axis component
d	d-axis component
q	q-axis component

Superscript

$+$	Positive-sequence component
$-$	Negative-sequence component
$*$	Reference value
^	Predicted/estimated value

1. INTRODUCTION

The technology evolution of wind energy conversion systems (WECS) is driving the rapid development of wind power as a mainstream power source. Its level of grid penetration and impact on modern power systems is growing and wind energy is already competitive to traditional fossil energy sources regarding levelized costs. The cumulative installed wind power in the European Union increased from 80 GW in 2010 to 220 GW by 2023. It is expected that, following the current trend, the cumulative wind capacity would reach 400 GW by 2030. The offshore technology appears as main driver [1] due to its higher wind speeds, which produce more power per unit of capacity. The initial investments and maintenance costs of an offshore wind farm appear as the main drawbacks of the technology, but it also presents several advantages that can compensate for its higher costs. Firstly, offshore wind resources are relatively strong and steady, which means that power production can be notably increased, providing a more reliable energy source. Secondly, offshore wind farms could help to meet the energy demands of densely populated coastal areas, where the land price is highly expensive. Finally, the visual impact and noise caused by wind turbines would be mitigated. The development trend of wind turbine toward high-power is shown in Fig. 1.1.

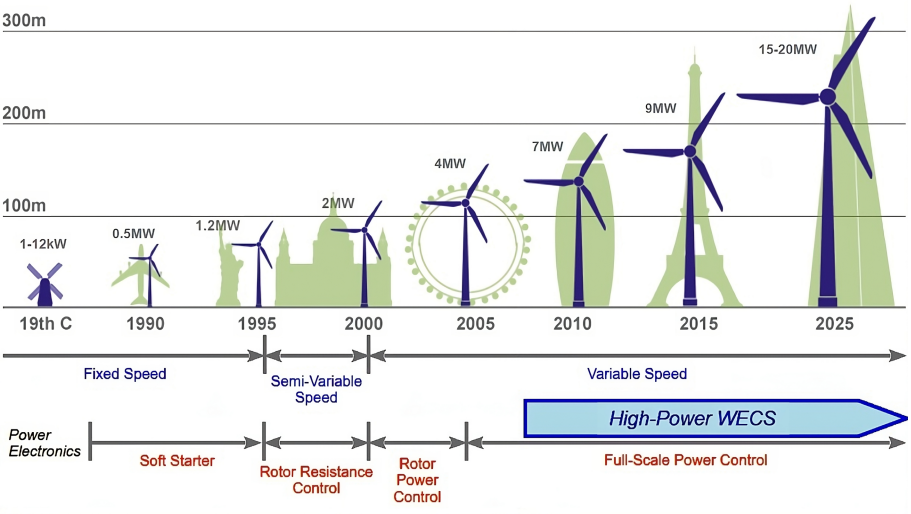

Fig. 1.1 The development trend of wind turbine. Source [J1].

The increase of wind energy utilization leads to an increasingly distributed power electronics-based power system. This new scenario brings promising novel architectures and great challenges for operating the power system with high security

and stability. Furthermore, the large-scale application of power electronics contributes to the growing complexity of power system with nonlinear and time-varying characteristics. Therefore, new advanced control methods of power electronic converter are of crucial importance to maintain security, efficiency, and robustness against disturbances and variations. Furthermore, in future power systems, WECS are expected to be grid-supportive, instead of simply grid-feeding elements. Consequently, new functionalities will be demanded by emerging grid codes to integrate the increasing penetration of power electronics-interfaced generation and enhance stability of electrical power system.

The high-power wind turbine is highly aligned with development of offshore wind farms [2]. This leads to a new scenario, where reliability, availability, and efficiency appear as key factors to overcome high maintenance costs of an offshore wind farm. The Type 4 WECS with permanent magnet synchronous generator (PMSG) [3] appears as the most suitable configuration for high-power wind turbines in offshore installations due to its high-power density and reliability. The use of a multi-pole PMSG can eliminate the need for a gearbox, resulting in reduced maintenance costs, downtime, and increased lifespan. Besides, direct-drive (gearless) systems are highly efficient [4]. High current and power loss at high power level are a design challenge for power electronic devices, cable, and passive elements. The power rating can be increased through paralleled structures to withstand high-current operation or through other multilevel topologies allowing a higher operating voltage. The three-level neutral-point-clamped (3L-NPC) converter is proposed as a cost-effective solution [5]. This converter is able to generate output voltage of three levels, leading to reduced harmonic filter requirement. The 3L-NPC converter is widely used in high-power application due to its simple implementation and proper performance. However, the 3L-NPC converter presents a technical limitation since power losses are unevenly distributed among switching devices [6]. Hence, the output power capability is limited by the most stressed switch. The active NPC (ANPC) converter [7] is an evolution of the 3L-NPC topology, where clamping diodes are replaced by active switches. These redundant switching states enable improved control of loss distribution and increased converter power capability [8]. In order to increase power rating of WECS, the 3L-NPC can be scaled up by adding more parallel-connected power conversion lines [9]. Fig. 1.2 shows the diagram of 3L-NPC with two conversion lines. The generator and transformer both feature two sets of three-phase windings configuration, ensuring electrical independence and facilitating isolation between the converters.

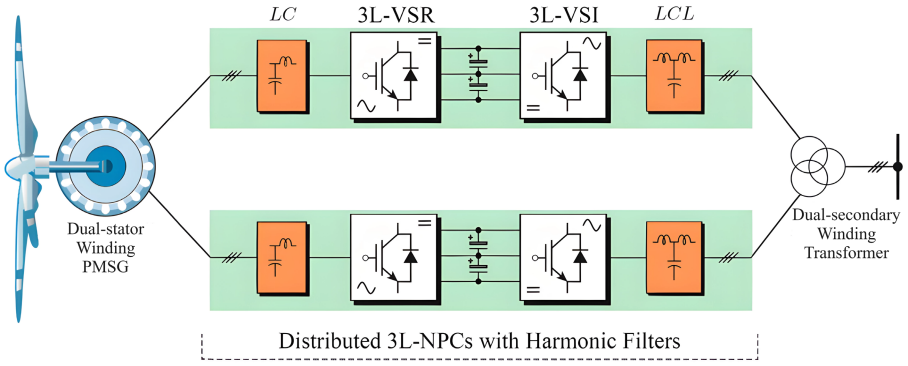

Fig. 1.2 Type 4 Direct Drive PMSG WECS with two 3L-NPC lines of conversion and two sets of three-phase windings configuration both in generator and transformer. Source [J1].

The advanced control theory is essential to optimize operational effectiveness of WECS, leading to improved efficiency, reduced costs, extended lifetime of components, minimized downtime, and superior dynamic and steady-state performance. In recent years, finite control set model predictive control (FCS-MPC) strategies have been frequently studied to improve operating performance of high-power wind turbine [10], being far superior to classical linear controls in terms of dynamic response and robustness against system uncertainties or parameter variations. In addition, the cost function definition in FCS-MPC gives a flexible criterion to incorporate multiple control objectives. However, the technology readiness assessment of predictive control techniques in high-power wind power converter, especially in industrial implementation, is not fully addressed.

This Industrial PhD Project initially investigates the application of FCS-MPC on a single 3L-NPC conversion line. The predictive control strategy is subsequently developed, and the operating performance is validated including dynamic response, robustness, and stability. Finally, the proposed control strategy is expanded to encompass two paralleled 3L-ANPC conversion lines of Ingeteam power converter solution for high-power offshore WECS.

1.1 State-of-the-art

Predictive control was first proposed in power electronics in the 1980s [11], but it was not further investigated before the 2000s due to the lack of sufficient computational capabilities. The development of powerful microprocessors renewed the interest of power electronics community in MPC. A wide range of predictive

control techniques have been developed since it is applied to control power electronic converters [12], [13].

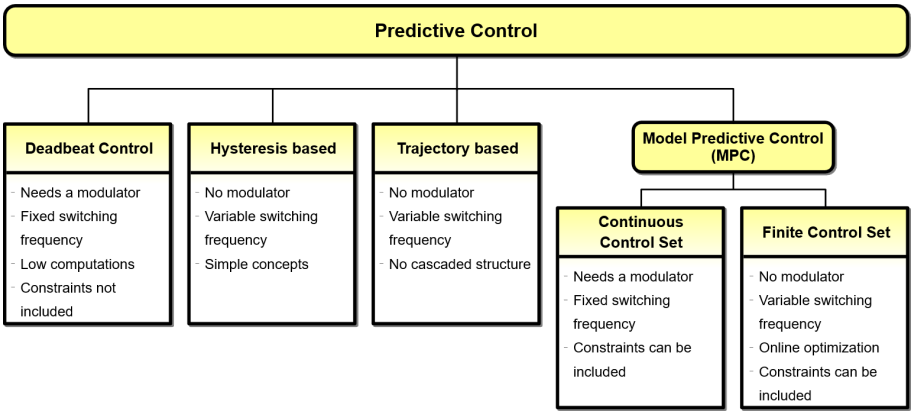

Fig. 1.3 Classification of predictive control methods used in power electronics.

The FCS-MPC, also known as direct MPC with reference tracking, is the most widely published MPC method [10], [14]. The FCS-MPC employs the finite set of possible switching states of the power converter and the system discrete-time model to predict the future behavior of the plant. The controller then implements the optimal control action based on predefined control objectives. The optimization problem thus consists of the evaluation of all possible states, and the selection of the one that minimizes the given cost function. The FCS-MPC [15], [16] is a closed-loop control method with implicit modulator, which imposes the switching of the converter through a cost-function minimization algorithm.

Cost function definition in FCS-MPC gives a flexible criterion for selecting optimal switching signals and the possibility to incorporate other requirements [15]. In this context, FCS-MPC provides the possibility of handling all control objectives in a single control loop, including non-linear features, such as constraints or parameter variations. FCS-MPC offers a faster dynamic response than that of the classical control techniques, ensuring a good steady-state reference tracking [16]. The discrete nature of the power converter fits perfectly with the modulator-free control structure of FCS-MPC. The FCS-MPC is then a flexible and intuitive approach for digital implementation, which allows constraints to be included in the design of the controller. Main characteristics of linear control with proportional-integral (PI) regulator and FCS-MPC are compared in Table 1.1.

Table 1.1: *Comparison of linear control with PI regulator and FCS-MPC [10].*

	Linear Control	FCS-MPC
Model	Linear Plant Model for PI and Converter Model for SVM	Discrete-Time Model of Complete System
Controller Design	PI Adjustment + Modulator Design	Cost Function Definition
Nature of Controller	Linear	Nonlinear
Modulation	PWM/SVM	Not Required
Switching Frequency	Fixed	Variable (but controllable)
Multivariable	Coupled	Decoupled
Constraints Inclusion	Not Possible	Easy to Include
Complexity of Concept	Medium with SVM	Simple and Intuitive
Steady-State Performance	Good in *dq*- frame	Good in *abc*-, *αβ*-, and *dq*- frames
Transient Performance	Moderate	Excellent
Computational Burden	Medium with SVM	High (regarding prediction horizon)

Thus, the FCS-MPC is a promising solution to enhance operating performance of high-power wind turbines [17], being far superior to classical linear controls in terms of dynamic response and robustness against system uncertainties or parameter variations. In addition, the cost function definition in FCS-MPC gives a flexible criterion to incorporate different control objectives to operate in a more reliable, stable, and efficient way. However, industry is commonly conservative to adopt new control methods if significant economic benefits are not provided.

The concerns related to FCS-MPC applied to high-power converter have been addressed in previous work.

(1) Real-time implementation: sampling time, computational complexity, and prediction horizon

The sampling time T_s in the real-time implementation of predictive control is selected based on the minimum execution time required to perform all control tasks. The ratio between sampling frequency and switching frequency is a key metric as FCS-MPC restricts switching transitions to discrete-time sampling instants [18]. Hence, the minimum sampling time is always recommended and switching frequency will be controlled by an additional control objective in cost function to meet specific application requirements. The number of calculations in each sampling interval is directly related to the number of switching states and the complexity of cost function. However, this can be mitigated by applying intelligent optimization algorithms which reduce computational time and ease real-time implementation of MPC. In [19], the vectors to be evaluated are constrained to offline-defined candidate subsets based on the modulation region of demanded reference voltage. In [20], the number of candidate switch states of 5L-ANPC inverter are reduced by limiting the output voltage to one-level jump.

FCS-MPC schemes with reference tracking have traditionally proposed a prediction horizon set to 1 [14]. However, it is expected that with more predictions in advance, more knowledge of the system is considered in cost function, and the controller is enabled to make better decisions. Then, long prediction horizons result in improved system performance [21]. However, for real-time implementation of FCS-MPC, long prediction horizons significantly increase the number of calculations caused by the combination of possible solutions. Therefore, the prediction horizon poses a trade-off between performance and computational effort. Then, the different techniques have been proposed in the literature to overcome the computational burden issues [22].

(2) Cost function design and weight tuning

The optimal switching to be applied is calculated by minimizing cost function. Therefore, cost function in the FCS-MPC strategy defines the desired system performance. Several control objectives can be handled if the corresponding control variables are included in cost function. Selecting an appropriate cost function is complicated when several control objectives are included in the optimization problem. Because of this, cost function increases its complexity, and the tuning process of weighing factors becomes more difficult. The weighting factor selection balances the contribution of control objectives to the cost function.

The adjustment of weighting factor values is not an easy task. Usually, the procedure consists in heuristic approaches that rely on trial-and-error, where the suitable values are found by a set of simulations [23]. This kind of empirical design

process requires a large number of tests and may not be exhaustive enough when the controller behavior depends on time-variant conditions. To avoid heuristics, other methods have emerged to automatize the tuning process and allow real-time setting for the weighting factors. In [24] the autotuning algorithm increases the cost function weights based on a predefined set of error thresholds, which makes the control algorithm robust to parameter variation and other uncertainties in the system. A similar approach is presented in [25], where the weighting factors are dynamically adjusted to prioritize the correction of the objective with the largest error. Moreover, other methods utilize techniques from artificial intelligence, such as Fuzzy Decision-Making [26]–[29], Artificial Neural Networks [30]–[33], and Genetic Algorithms [34].

(3) Switching frequency control and harmonic spectra

One of the main challenges for FCS-MPC is the resulting random switching frequency due to the absence of a modulator. If no action is taken, the spectrum of the converter output voltage is spread over a broad range up to half of the sampling frequency. The lack of control of switching frequency may cause some undesirable behaviors such as increased switching losses or resonances, and complicate harmonic filter design. The capability of FCS-MPC to operate at variable switching frequency and its impact on power loss and thermal stress of power modules should be further investigated [35]. The thermal characteristics of power devices require a rigorous analysis to ensure the reliable long-term operation of power converter.

The lack of modulation stage not imposing a periodic switching pattern implies dispersed harmonic spectra, which could be problematic for grid-connected inverters, where existing grid codes such as IEEE 519 standard [36] establish the voltage and current harmonic limits at the point of common coupling (PCC). The different harmonic shaping methods have been proposed, which incorporate penalties on specific frequency components [37]–[39] or combines MPC with selective harmonic elimination (SHE) modulation pattern [40]. In [41], there are reviewed some strategies that deal with the issue of random switching frequency and harmonic content for FCS-MPC. Furthermore, different strategies which combine predictive control with space vector modulation (SVM) are also considered to enable fixed switching frequency operation and maintain advantages of FCS-MPC, such as the modulated MPC (M^2PC) [42], [43] and the optimal switching sequence MPC (OSS-MPC) [44]. In [45], the Model Predictive Pulse Pattern Control (MP^3C) is presented for industrial application as a fast online predictive controller which directly modifies the optimized pulse patterns (OPP).

(4) Stability analysis of FCS-MPC

The closed-loop stability is a classical subject matter in control engineering. The purpose of digital control is to ensure that system converges to desired setpoint values, and thus maintains closed-loop stability and rejects disturbances that occur in the plant. With the increasing penetration of power electronic-interfaced wind turbines, the oscillation phenomena within a wide frequency range have been reported. Resonance problems are even critical in offshore wind farms because of the complex resonance frequency characteristic of long transmission cable and interaction between multiple converters [46]. Hence, the intensive efforts have been conducted to investigate the root causes of oscillation phenomena and instability issues.

Two analytical methods have been developed for stability analysis: the eigenvalue analysis based on the state-space model of the system in the time domain [47], [48], and the impedance-based analysis consisting of transfer functions of components in the frequency domain [49]–[51]. The eigenvalue approach is advantageous for identifying oscillation modes and instability roots of system variables, making it preferable for comprehensive systematic analysis. However, it requires all system information to perform stability analysis, which vendors may keep private. On the other hand, the impedance-based approach analyses the whole system based on the Input/Output characteristic (impedance) of each subsystem. Once the impedance of each subsystem is determined, system stability can be assessed by adding, removing, or modifying a subsystem. Changes in one subsystem will not affect the others, allowing for easy reformulation of the new system. This approach is particularly suitable for analyzing subsystem interactions. Furthermore, the impedance-based method offers a black-box feature, making it a powerful technique when detailed system information is unavailable. A comparison of the features of both system stability analysis tools is presented in Table 1.2.

Table 1.2: *Comparison of System Stability Analysis Tools. Source [52].*

Features	Eigenvalue method	Impedance method
Identification of oscillation modes	✓	–
Participation factor of state variables and sensitivity analysis	✓	–
Input-output dynamics	✓	✓
Design-oriented analysis	Moderate	High
Black-box modeling	–	✓
Modularity	–	✓
Scalability	Low	High

The MPC strategies exhibit several advantages compared to classical PI controls, since its modulator-free structure and reduced digital control delay further extend the stability region of power converter. This feature is particularly interesting for high-power operation, where the low switching frequency requirements severely limit the maximum available bandwidth of current control structures based on pulse width modulation (PWM) [53]. However, MPC formulates a complicated nonlinear problem when constraints and weighting factors are considered. Hence, the closed-loop stability analysis is difficult due to the absence of explicit mathematical model. Although infinite-horizon may guarantee stability [54] and Lyapunov stability criteria can be adopted in cost function design [55], closed-loop stability of FCS-MPC for grid-connected inverter in practical operation has not been fully addressed.

1.2 Research questions and objectives

As mentioned in section 1.1, the application of model predictive control in high-power converter offers advantages over conventional linear control strategies. Nonetheless, there exist technical challenges, which should be addressed to facilitate the widespread adoption of FCS-MPC in wind power conversion systems. The objective of this Industrial PhD Project is to explore the promising attributes of FCS-MPC, propose novel approaches to mitigate some of its practical limitations, and assess the integration of this predictive algorithm into Ingeteam power converter solution. The main research questions of this PhD Thesis can be summarized as follows.

(1) How can the random switching frequency, resulting from the carrier-less nature of FCS-MPC, be effectively controlled under diverse operating conditions to meet stringent high-power thermal requirements?

(2) How can the fast dynamic response of model predictive control be exploited to optimize fault ride-through operation and ensure compliance with the most recent grid codes?

(3) To what extent does the accuracy of the underlying model influence controller performance, and what strategies can enhance its robustness against parametric uncertainties?

(4) How can the stability of FCS-MPC be analyzed due to lack of explicit mathematical model? How to ensure stable operation of WECS by appropriately designing cost function?

(5) How can the predictive control algorithm be efficiently implemented in Ingeteam converter control unit (CCU) while addressing control platform specific limitations (e.g., computational burden, inherent delays…)?

The above research questions will be thoroughly addressed in the forthcoming chapters of this dissertation, which are built upon the published journal and conference papers.

1.3 Outline of thesis

The PhD Thesis consists of five chapters based on seven publications. The content of each chapter and corresponding publications are summarized as follows.

Chapter 1. Introduction.

State-of-the-art of high-power wind turbines and FCS-MPC application for high-power converter is presented. The research questions and goals of this PhD Project are explained.

The work in chapter 1 is based on publication J1

Chapter 2. The proposed FCS-MPC strategy for 3L-NPC inverter.

The FCS-MPC strategy for 3L-NPC inverter is developed. The cost function and the online tuning method is proposed to control switching frequency. Furthermore, the fault ride-through operation and grid-code compliance in terms of reactive current provision during grid faults is analyzed. In addition, the robustness of FCS-MPC against grid filter inductor variations is investigated.

The work in chapter 2 is based on publications C1, C2, J2, C3

Chapter 3. Stability analysis of 3L-NPC inverter with the proposed MPC.

The frequency-scan technique is proposed to obtain input impedance of 3L-NPC power converter operated with FCS-MPC. The impact of controller design on impedance characteristic is investigated. The integration of a wind turbine with MPC into offshore wind power plant (OWPP) is analyzed.

Based on publications C1, J3

Chapter 4. Implementation of the proposed control strategy in Ingeteam power converter solution.

The procedure of implementing the proposed FCS-MPC algorithm in the Ingeteam CCU is described in detail. Practical feasibility of MPC controller in the real control platform is demonstrated, and limitations of control unit are pointed out. Operating performance of two paralleled power conversion lines is analyzed in detail combining both simulation and hardware-in-the-loop verification.

Based on publication C4

Chapter 5. Conclusion.

Main contributions from the Industrial PhD Project are summarized, and future research aspects are given.

Fig. 1.4 shows the structure of the PhD Thesis, where the related publications are assigned to the different chapters.

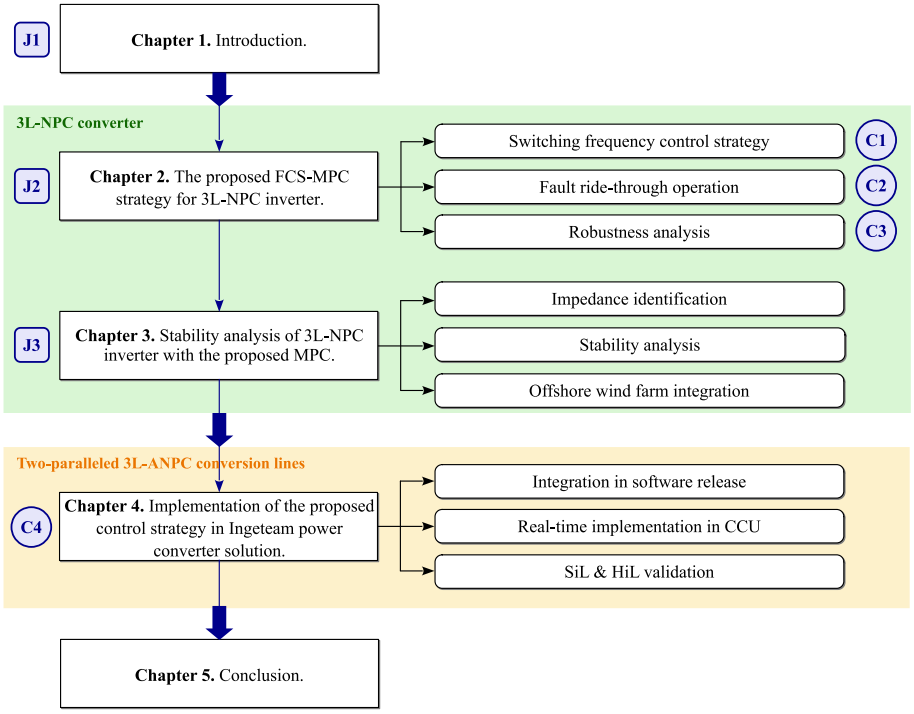

Fig. 1.4 Structure of the PhD Thesis.

1.4 Publication list

This thesis is based on the following papers in peer-reviewed conference proceedings and international journals.

Publications in Refereed Journals

J1. P. Catalán, Y. Wang, J. Arza and Z. Chen, "A Comprehensive Overview of Power Converter Applied in High-Power Wind Turbine: Key Challenges and Potential Solutions," in *IEEE Transactions on Power Electronics*, vol. 38, no. 5, pp. 6169-6195, May 2023.

J2. P. Catalán, Y. Wang, J. Arza and Z. Chen, "Advanced Fault Ride-Through Operation Strategy Based on Model Predictive Control for High Power Wind Turbine," in *IEEE Transactions on Sustainable Energy*, vol. 15, no. 1, pp. 513-526, Jan. 2024.

J3. P. Catalán, Y. Wang, C. Ruiz, G. Abad, J. Arza and Z. Chen, "Explicit Stability Assessment of High-Power Inverter with Model Predictive Control in Offshore Wind Farm," in *IEEE Journal of Emerging and Selected Topics in Industrial Electronics.* (under review).

Publications in Refereed Conferences

C1. P. Catalán, Y. Wang, Z. Chen and J. Arza, "Model Predictive Control Strategy for NPC Converter-based Wind Turbine with Switching Frequency Control," *2021 IEEE Southern Power Electronics Conference (SPEC)*, Kigali, Rwanda, 2021, pp. 1-7.

C2. P. Catalán, Y. Wang, Z. Chen and J. Arza, "Model Predictive Control-enabled Fault Ride Through Operation Strategy for High Power Wind Turbine," *2022 24th European Conference on Power Electronics and Applications (EPE'22 ECCE Europe)*, Hanover, Germany, 2022, pp. 01-10.

C3. P. Catalán, Y. Wang, Z. Chen and J. Arza, "Robust Predictive Control Strategy of 3L-NPC Wind Power Converter Against Filter Inductor Variations," *2023 25th European Conference on Power Electronics and Applications (EPE'23 ECCE Europe)*, Aalborg, Denmark, 2023, pp. 01-08.

C4. P. Catalán, Y. Wang, Z. Chen and J. Arza, "Model Predictive Control Strategy for High-Power Wind Turbine based on Paralleled Active Neutral Point Clamped Converter," *10th International Power Electronics and Motion Control Conference – ECCE Asia (IPEMC 2024-ECCE Asia)*, Chengdu, China, 2024, pp. 01-08. (Accepted).

2. THE PROPOSED FCS-MPC STRATEGY FOR 3L-NPC INVERTER

2.1 Discrete-time model of 3L-NPC inverter

In this section, discrete-time model of 3L-NPC inverter is established. This model is used to predict the response of the plant to a sequence of inputs. According to a discrete-time state-space representation the internal model can be formulated by

$$x(k+1) = f(x(k), u(k)) \tag{1}$$

$$y(k) = g(x(k)) \tag{2}$$

where $k \in \mathbb{N}$ indicates the discrete time step. The state vector $x \in \mathbb{R}^{n_x}$ stands for the system state variables (e.g., currents, voltages, etc.), and the output vector $y \in \mathbb{R}^{n_y}$ represents the system outputs to be controlled (e.g., output currents references). The control input vector $u \in \mathbb{Z}^{n_u}$ belongs to a finite control set (FCS) corresponding to the switch positions of the power converter.

In most cases, the power electronic system can be considered a Linear Time Invariant (LTI) system. Thus, the state-space model takes the form as (3)-(4).

$$x(k+1) = A_d x(k) + B_d u(k) \tag{3}$$

$$y(k) = C_d x(k) \tag{4}$$

The system matrix A_d, input matrix B_d, and output matrix C_d are derived from the continuous-time state-space model of the system by using a discretization method. Generally, the main control target is to track the desired output references, but additional targets can be included, such as switching frequency control, capacitor voltage balancing, or harmonic spectrum shaping.

Fig. 2.1 shows the per-phase configuration of the 3L-NPC converter. Each phase consists of two complementary pairs of IGBTs switching devices *(S_{a1}, S'_{a1}, S_{a2}, S'_{a2})* and two clamping diodes *(D_{a1}, D_{a2})*. The DC-link is composed of two series-connected identical capacitors *(C_1, C_2)* and their neutral-point is denoted as 0, and clamping diodes are connected to it.

The 3L-NPC converter allows three switching states to generate the three-level waveform at the output terminal. In this topology, only two switches conduct at any time and, to avoid forbidden states, there is a limiting condition that adjacent switches must be ON. The switching states are tabulated in Table 2.1. Furthermore, the switching sequence restrictions force that only one IGBT per phase can switch at once.

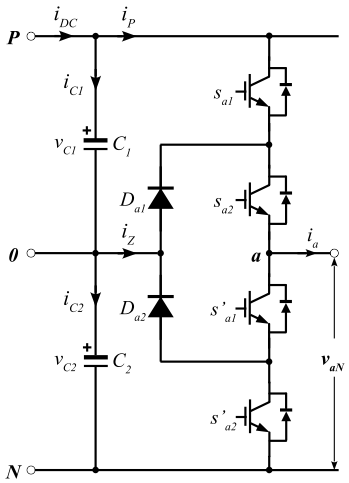

Fig. 2.1 Per-phase 3L-NPC converter.

Table 2.1: *3L-NPC switching states.*

Switching Vector	**Switching Orders**				**Output Voltage**
S_x	S_{a1}	S_{a2}	S'_{a1}	S'_{a2}	v_{aN}
[2]	1	1	0	0	$v_{C1}+v_{C2}$
[1]	0	1	1	0	v_{C2}
[0]	0	0	1	1	*0*

With three modes in each phase, the 3L-NPC converter presents 27 different switching states and 19 different voltage vectors *(V0 to V18)* [56]. The zero-voltage vector V0 has three redundancies and voltage vectors *V1* to *V6*, which form the inner hexagon, have two redundancies. Due to the presence of these redundancies, different switching states can be employed not only to synthesize the desired output voltage but also to balance the neutral-point voltage. The detailed space vector diagram for a three-phase balanced 3L-NPC converter is shown in Fig. 2.2. A complete summary of 3L-NPC output voltage vector and corresponding switching states is included in Table 2.3.

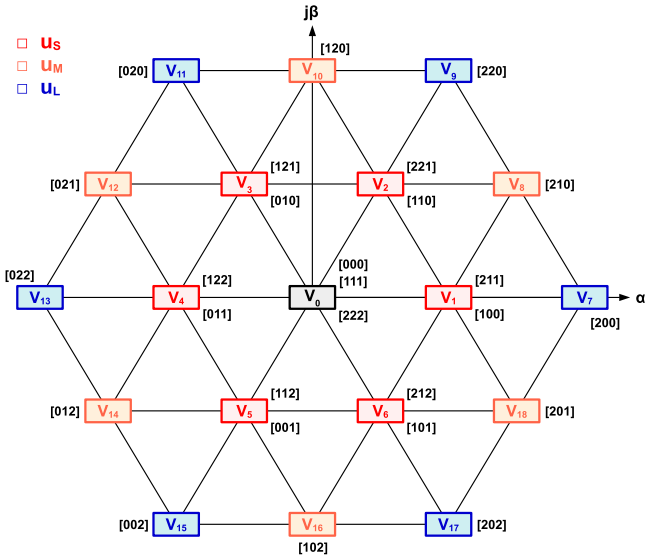

Fig. 2.2 Space vector diagram for 3L-NPC converter.

The output voltage of 3L-NPC converter is determined by gating signals and DC-link capacitor voltages as (5).

$$\begin{bmatrix} v_{aN} \\ v_{bN} \\ v_{cN} \end{bmatrix} = v_{C1} \cdot \begin{bmatrix} S_{a1} \\ S_{b1} \\ S_{c1} \end{bmatrix} + v_{C2} \cdot \begin{bmatrix} S_{a2} \\ S_{b2} \\ S_{c2} \end{bmatrix} \tag{5}$$

where S_{a1}, S_{a2}, S_{b1}, S_{b2}, S_{c1}, S_{c2} are the switching signals for the converter, and v_{C1} and v_{C2} are the DC-link capacitor voltage.

The grid current dynamics can be expressed in terms of inverter voltage, grid voltage, and filter inductance.

$$\frac{di(t)}{dt} = \frac{1}{L_f}\left[v_o(t) - R_f i(t) - v_g(t)\right] \tag{6}$$

where R_f and L_f are the output resistance and inductance of the power converter, respectively, v_o is the voltage generated by the inverter, v_g is the grid voltage, and i is the grid current.

The discrete-time form of (6) for a sampling time T_s can be used to predict the future value of grid current based on the measured voltage and current at the k_{th} sampling instant. The derivation with Backward-Euler discretization method is approximated as (7).

$$\frac{di(t)}{dt} \approx \frac{i(k) - i(k-1)}{T_s} \tag{7}$$

and replacing it in (6), the following expression is obtained for grid current.

$$i(k) = \frac{1}{R_f T_s + L_f}\left[L_f i(k-1) + T_s v_o(k) - T_s v_g(k)\right] \tag{8}$$

Shifting the discrete-time one step forward in (8), the future grid current is determined by (9).

$$i(k+1) = \frac{1}{R_f T_s + L_f}\left[L_f i(k) + T_s v_o(k+1) - T_s v_g(k+1)\right] \tag{9}$$

Equation (9) is used to obtain predictions for the future value of grid current $i(k+1)$, considering all possible voltage vectors v_o generated by the inverter.

In FCS-MPC, stationary reference *(αβ)* frame is extensively used to reduce computational burden. The variables are represented as two-phase variables, which exhibit a time-varying nature in a two-dimensional orthogonal space.

The 3L-NPC inverter terminal voltage is calculated in the *αβ*-frame as (10).

$$\begin{bmatrix} v_\alpha(k) \\ v_\beta(k) \end{bmatrix} = v_{C1}(k) \cdot \left[T_{abc/\alpha\beta}\right] \cdot \begin{bmatrix} s_{a1}(k) \\ s_{b1}(k) \\ s_{c1}(k) \end{bmatrix} + v_{C2}(k) \cdot \left[T_{abc/\alpha\beta}\right] \cdot \begin{bmatrix} s_{a2}(k) \\ s_{b2}(k) \\ s_{c2}(k) \end{bmatrix} \tag{10}$$

where

$$\left[T_{abc/\alpha\beta}\right] = \frac{2}{3}\begin{bmatrix} 1 & -\frac{1}{2} & -\frac{1}{2} \\ 0 & \frac{\sqrt{3}}{2} & -\frac{\sqrt{3}}{2} \end{bmatrix} \tag{11}$$

The DC-link capacitor voltages are expressed in terms of the DC-link capacitor current as (12).

$$\begin{aligned} \frac{d}{dt} v_{C1}(t) &= \frac{1}{C_1} i_{C1}(t) \\ \frac{d}{dt} v_{C2}(t) &= \frac{1}{C_2} i_{C2}(t) \end{aligned} \tag{12}$$

where i_{C1} and i_{C2} are the currents in DC-link capacitors C_1 and C_2, respectively.

The discrete-time model of the DC-link capacitor voltage is calculated by introducing (7) in (12) as follows.

$$\begin{aligned} v_{C1}(k+1) &= v_{C1}(k) + \frac{T_s}{C_1} i_{C1}(k) \\ v_{C2}(k+1) &= v_{C2}(k) + \frac{T_s}{C_2} i_{C2}(k) \end{aligned} \tag{13}$$

Currents through the capacitors are determined based on grid currents and the present switching state. Thus, no additional measurements are needed. The DC branch i_P and i_Z currents can be expressed in terms of the switching signals and measured currents.

$$\begin{bmatrix} i_P \\ i_Z \end{bmatrix} = \begin{bmatrix} s_{a1} \cdot s_{a2} & s_{b1} \cdot s_{b2} & s_{c1} \cdot s_{c2} \\ s_{a2} \cdot s'_{a1} & s_{b2} \cdot s'_{b1} & s_{c2} \cdot s'_{c1} \end{bmatrix} \cdot \begin{bmatrix} i_a \\ i_b \\ i_c \end{bmatrix} \tag{14}$$

The DC-link capacitor current is derived from i_{DC}, i_P and i_Z as (15).

$$\begin{aligned} i_{C1} &= i_{DC} - i_P \\ i_{C2} &= i_{C1} - i_Z = i_{DC} - i_P - i_Z \end{aligned} \tag{15}$$

(1) Back-to-back 3L-NPC modeling

The configuration of back-to-back 3L-NPC converter is shown in Fig. 2.3. The DC-link capacitor voltage is affected by switching actions of both 3L-NPC rectifier (machine-side-converter) and 3L-NPC inverter (grid-side-converter). Thus, equation (15) must be augmented by considering the effect of machine-side-converter for the precise control of neutral-point balance.

The DC-link capacitor current is derived from i_{Pr}, i_{Zi} , i_{Pi}, and i_{Zi} as (16).

$$\begin{aligned} i_{C1} &= i_{Pr} - i_{Pi} \\ i_{C2} &= i_{C1} + i_{Zr} - i_{Zi} \end{aligned} \tag{16}$$

where the contribution of 3L-NPC rectifier can be obtained in a similar approach as (14).

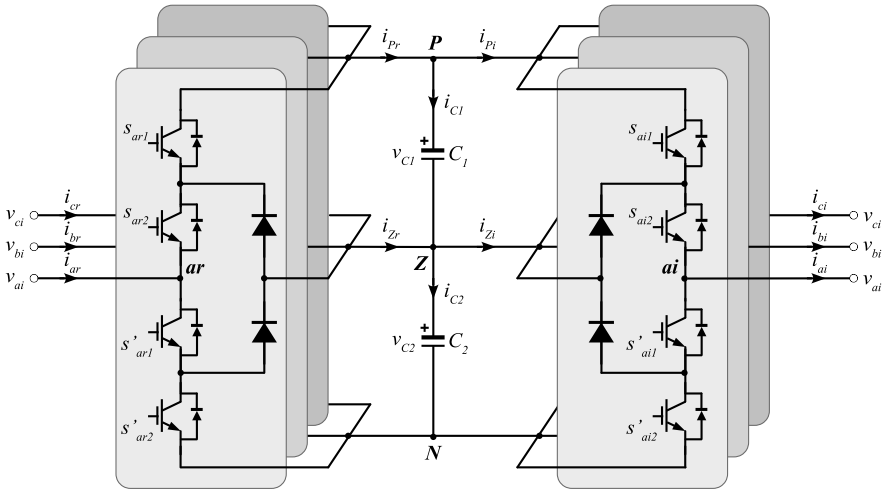

Fig. 2.3 Back-to-back 3L-NPC converter.

(2) DC-link protection

The transient power imbalance between machine-side converter and grid-side converter, mainly during grid faults, may result in voltage boost of DC-link. The DC braking chopper is then activated to dissipate the excessive energy and prevent overvoltage. Each DC capacitor is protected by a braking chopper circuit as shown in Fig. 2.4(a), which is operated by the hysteresis control of capacitor voltage as shown in Fig. 2.4(b). The switch-on threshold ensures the safe operating voltage of the components. Additionally, the voltage difference between hysteresis thresholds must be adequate to control the switching frequency of the braking chopper IGBT.

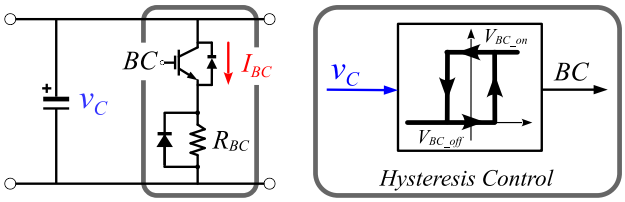

Fig. 2.4 The braking chopper protection circuit for each half bus of 3L-NPC converter operated with hysteresis control. (a) The diagram of DC chopper circuit. (b) Hysteresis control. Source [J2].

The activation of braking chopper must be considered for the precise estimation of capacitor currents.

$$i'_{C1} = i_{C1} - i_{BC1}$$
$$i'_{C2} = i_{C2} - i_{BC2} \tag{17}$$

where i_{BC1} and i_{BC2} are the currents through braking chopper circuits that can be estimated as (18).

$$i_{BC} = BC \cdot \frac{v_C}{R_{BC}} \tag{18}$$

where BC represents the activation order (0/1) of the braking chopper, v_C is the capacitor voltage, and R_{BC} is the braking chopper resistor value.

2.2 The proposed MPC control strategy

The predictive control strategy considers the finite number of possible switching states of power converter and predicts the behavior for each switching state based on the model of the system. A cost function is then evaluated for the predicted values of the variables to be controlled, and the switching state that minimizes the cost function is selected. Fig. 2.5 presents the proposed control strategy using a FCS-MPC scheme.

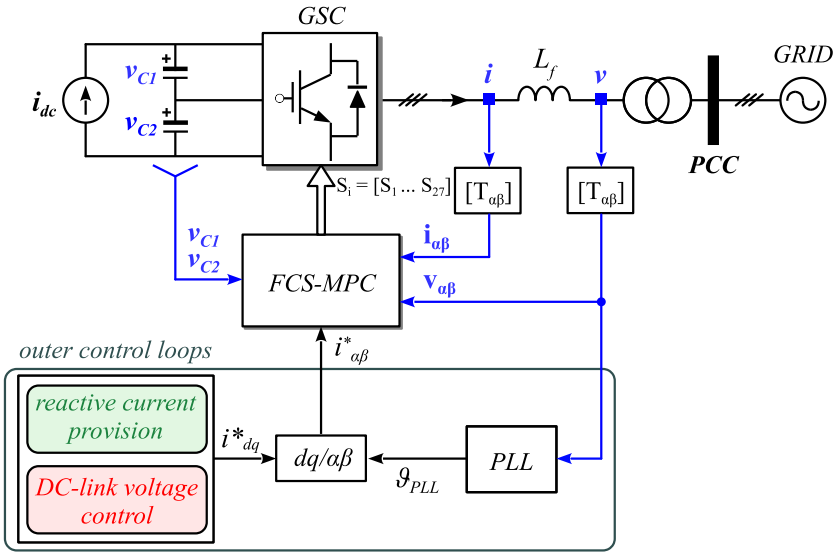

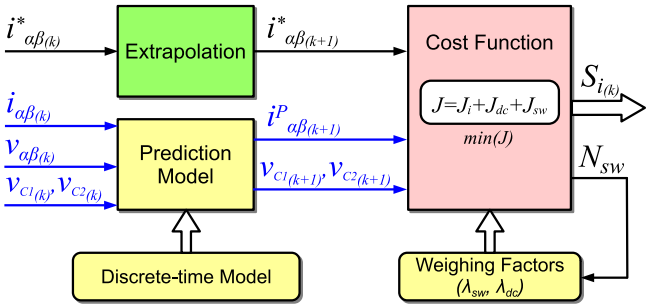

Fig. 2.5 The proposed control strategy. Source [J2].

2.2.1 Current regulation

Current regulation is widely employed in the inner control loop of power conversion applications. Currents can be controlled by defining a cost function incorporating the error between predicted currents $i(k+1)$ and extrapolated references $i^*(k+1)$. The squared 2-norm is recommended [57], where the current error grows quadratically, and sufficiently large current errors will always trigger a switching transition. Therein, it is demonstrated that when the squared 2-norm is used, good reference tracking and closed-loop stability is guaranteed. The current reference tracking control objective J_i is included into cost function as (19).

$$J_i = \lambda_i \cdot \left([i^*_\alpha(k+1) - i_\alpha(k+1)]^2 + \left[i^*_\beta(k+1) - i_\beta(k+1) \right]^2 \right) \qquad (19)$$

where i and i^* are predicted currents and extrapolated references to instant $(k+1)$, respectively. The associated weight is normally set as $\lambda_i = 1$.

2.2.2 DC-link voltage balancing

Neutral-point (NP) voltage balance of 3L-NPC converter is an important concern since the imbalance can cause distortion of AC output voltage and additional stress in power converter. When the small- or medium-size space vectors (u_S and u_M) are active, the current flows through the clamping diodes and the NP voltage can be affected [58]. Due to non-perfect symmetry in power converter and transient operating conditions, the average NP currents may take non-zero values, which can deteriorate the voltage balance of DC-link capacitors. Then, a NP balancing strategy is required to minimize capacitor voltage imbalance.

The DC-link capacitor voltage balancing control J_{dc} is added to the cost function as a secondary goal as (20).

$$J_{dc} = \lambda_{dc} \cdot [v_{C1}(k+1) - v_{C2}(k+1)]^2 \tag{20}$$

where v_{C1} and v_{C2} are DC-link capacitor voltages, and λ_{dc} represents the weighting factor.

2.2.3 Switching frequency control strategy

The simplest way to reduce switching frequency in FCS-MPC is the incorporation of a new element J_{sw} into the cost function, making switching transitions to another state less attractive [59].

$$J_{sw} = \sum_{i=1}^{N} \lambda_{sw_i} \cdot |s_i(k) - s_i(k-1)| \tag{21}$$

where $s_i(k)$ is the state of each switching element i, N is the total number of switching elements, and λ_{sw_i} represents the weighting factor for each switching element.

Since the change of state is penalized, the controller is encouraged to remain in the current state, leading to an overall reduction of average switching frequency. However, the effective timing of the switching is still out of control, so random switching pattern remains.

2.2.4 Cost function design of proposed MPC

The one-step prediction horizon is employed to minimize computational load. The cost function of the MPC controller, defined as (22), incorporates the aforementioned control objectives: current regulation, neutral-point voltage balancing, and control of average switching frequency.

$$J = J_i + J_{dc} + J_{sw} \tag{22}$$

The control system is required to deal with system disturbances such as time-variant grid conditions, parameters uncertainty, or time-varying passive components under long-term operation. Therefore, a self-tuning FCS-MPC with variable weighting factors can improve system performance. For this purpose, a proper performance metrics definition is required, where both steady state and dynamic

parameters need to be considered. Furthermore, the optimal method to tune the weighting factors must meet a trade-off between the exhaustiveness, the labor of design process, and the additional computational burden required for online calculations.

In this section, the impact of grid impedance and operating point on switching frequency and neutral-point balance is investigated. Also, the corresponding tuning method is proposed. The detailed parameters of the system are given in Table 2.2.

Table 2.2: *Parameters of the grid-connected inverter.*

Parameter	**Value**
Rated Power P_N	4 MW
Rated Voltage V_g	3100 V
DC-link voltage V_{dc}	5200 V
Average switching frequency f_{sw}	1 kHz
DC-link capacitors C_1, C_2	20 mF
Braking chopper resistor R_{BC}	1.0 Ω
Filter Inductance L_f	400 μH
Filter Resistor R_f	1.3 mΩ
Sampling Time T_s	50 μs

1) Average switching frequency weight λ_{sw} tuning

Fig. 2.6 shows the simulation analysis of grid impedance and operating point impact on switching frequency of the 3L-NPC converter, where the FCS-MPC is tuned with fixed weight factors (λ_{sw} = 0.01, λ_{dc} = 0.001). Switching frequency is derived from transitions of *a*-phase external IGBT (S1) and internal IGBT (S2) of the 3L-NPC inverter. Fig. 2.6(a) shows simulation results considering active power variation with fixed grid impedance (SCR = 10). Fig. 2.6(b) shows simulation results considering rated active power (P = 4.0 MW) and reactive power variation with fixed grid impedance (SCR = 10). It can be observed the minor influence of both active and reactive power level on switching frequency. Fig. 2.6(c) shows the simulation results for different grid short circuit ratio (SCR from 20 to 1.5) when power converter operates at rated active power (P = 4.0 MW, Q = 0).

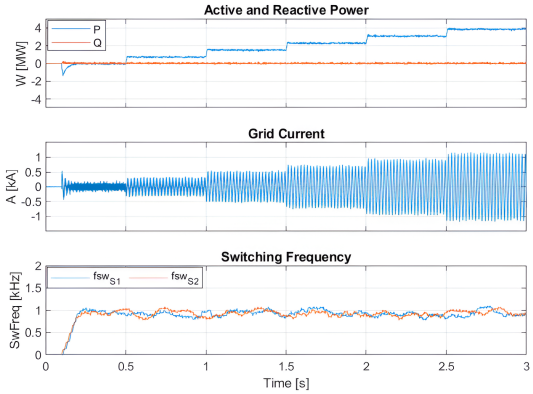

(a) Variations in active power.

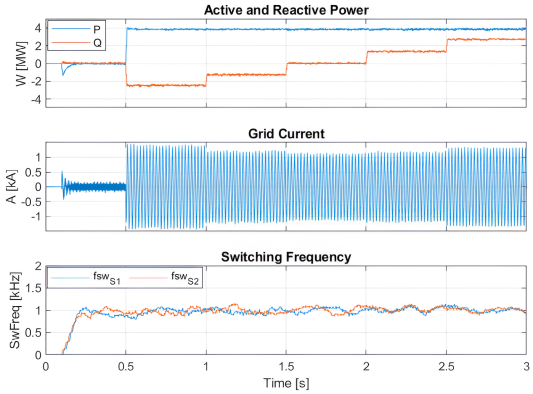

(b) Variations in reactive power.

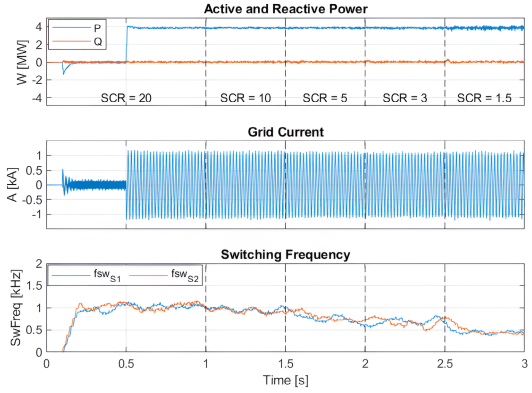

(c) Variations in SCR.

Fig. 2.6 Simulation results of 3L-NPC inverter with fixed weight for switching frequency (λ_{sw} = 0.01). Source [C1].

The simulation results reveal the strong influence of grid impedance on the average switching frequency of the power converter. The high-impedance grid causes a reduction in average switching frequency, which deteriorates power converter performance. Thus, the online tuning is required to maintain optimal performance under time-varying operating conditions.

The self-tuning strategy with variable weight λ_{sw_i} is employed to control switching frequency [60]. Fig. 2.7 shows the proposed online tuning strategy for λ_{sw_i}. The switching actions generated by MPC for each switching element are accumulated in a time-based sliding window of time length of T_w. Then, the cumulative sum of switching actions N_{sw_i} is multiplied by $2/T_w$ to calculate the average switching frequency f_{sw_i}. This value of f_{sw_i} is equivalent to that obtained with a carrier-based solution. The deviation between the estimated frequency f_{sw_i} and the reference f_{sw}^* is utilized as the error signal in a PI controller, which conducts online tuning of λ_{sw_i}. The average value of the switching frequency is then regulated to the desired reference.

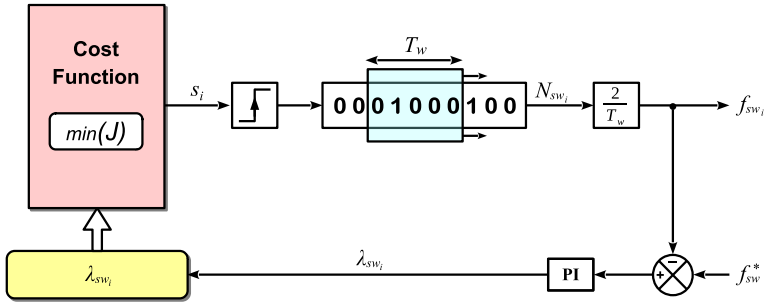

Fig. 2.7 Online tuning strategy for λ_{sw}.

Fig. 2.8 depicts the simulation results of 3L-NPC inverter under grid impedance variations when employing online tuning of λ_{sw}. In contrast to the fixed tuning case illustrated in Fig. 2.6(c), Fig. 2.8 demonstrates the effectiveness of the proposed switching frequency control method with adaptive weight λ_{sw} in regulating the average switching frequency against grid impedance variations. This capability thus ensures the sustained power quality of inverter.

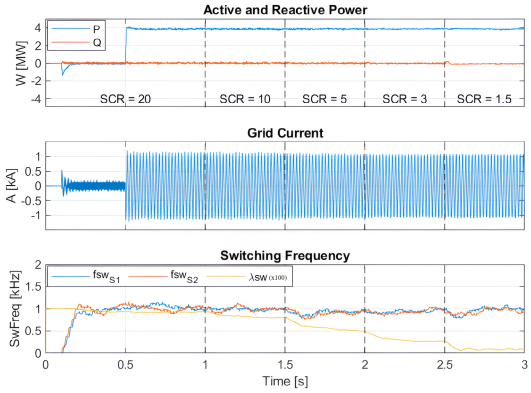

Fig. 2.8 Simulation results of 3L-NPC inverter against SCR variations with adaptive weight λ_{sw} for frequency control. Source [C1].

For situations causing distinct operating conditions of IGBTs, such as fault ride-through transient operation, the individual online tuning of λ_{sw_i} is needed for each of the controlled switching devices. Fig. 2.9 shows the simulation results of a 2-phase 0% low-voltage ride-through (LVRT). At 2s, *a*-phase and *b*-phase are short-circuited, and the grid fault lasts for 200ms. In Fig. 2.9(a), the fixed tuning of $\lambda_{sw} = 0.01$ is employed. The switching frequency is successfully controlled at the target value of 1kHz in steady state. However, fixed tuning of λ_{sw} proves ineffective for grid fault operation, where the switching frequency deviates and rises to $f_{swMAX} = 2.4\ kHz$ for IGBTs on the *a*-phase-leg. In Fig. 2.9(b), online tuning for switching frequency regulation is enabled. The increase in switching frequency, reaching a maximum value of $f_{swMAX} = 1.66\ kHz$ for the internal IGBT in the *a*-phase-leg, is mitigated by adapting values of λ_{sw}.

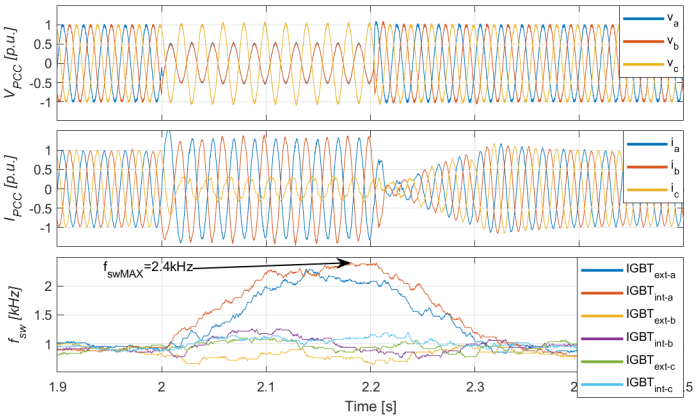

(a) Fixed tuning of $\lambda_{sw} = 0.01$.

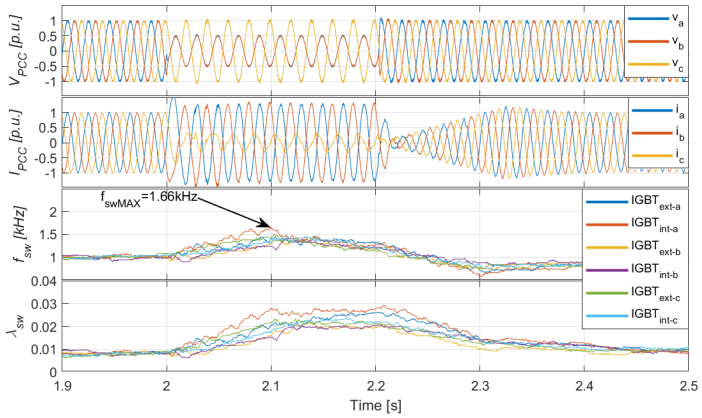

(b) Online tuning of λ_{sw}.

Fig. 2.9 The simulation results of 3L-NPC converter under 2-phase 0% LVRT. Source [J2].

In publications **C1** and **J2**, it is demonstrated that the fixed tuning of λ_{sw} may lead the power converter operating at different switching frequencies even among power devices. Further, a novel switching frequency control strategy is proposed based on the adaptive tuning of λ_{sw} and its effectiveness is validated under different time-variant conditions, such as grid impedance changes and fault ride-through transient operation. The proposed method is not only robust against variations in the plant, but also enables online switching frequency control. Fig. 2.10 shows the simulation results of online switching frequency control of 3L-NPC converter. The switching frequency reference f_{sw}^* is changed from rated value of $f_{sw}^* = 1kHz$ to $f_{sw}^* = 0.8kHz$ at 10s, and to $f_{sw}^* = 1.2kHz$ at 15s. The online tuning strategy dynamically adapts the value of λ_{sw} in order to control the average value of switching frequency to desired reference value as illustrated in Fig. 2.10(a). The output voltage and current waveforms of 3L-NPC converter are shown in Fig. 2.10(b). As observed, a higher switching frequency leads to a reduction in current total harmonic distortion (THD). However, the increase in switching frequency has an impact on switching losses and thermal stress on power devices. This capability may be further exploited to perform loss management and active thermal control (ATC) regarding the operating conditions, which optimizes power converter utilization.

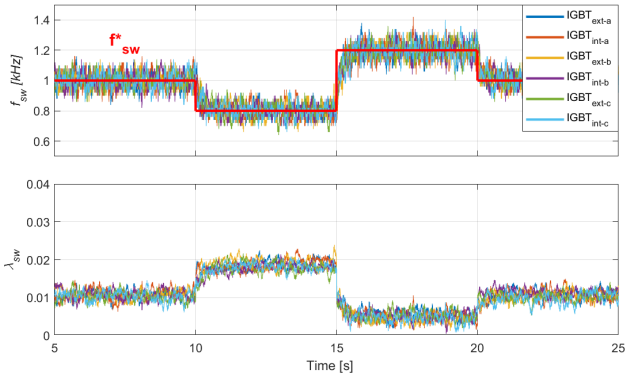

(a) Average switching frequency control.

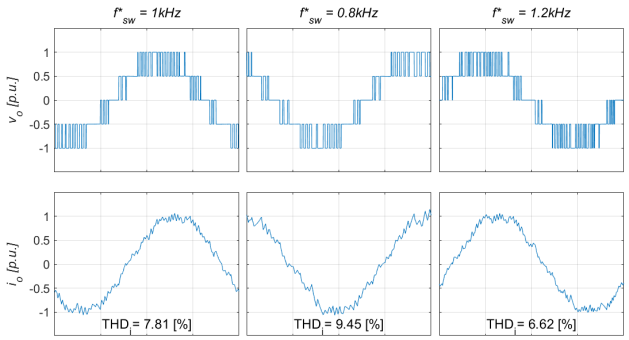

(b) 3L-NPC converter output voltage and current waveforms.

Fig. 2.10 The simulation results of online switching frequency control of 3L-NPC converter.

2) Neutral-point control weight λ_{dc} tuning

The neutral-point balancing issue is related to modulation index and power factor of power converter [61]. Thus, the optimal weight λ_{dc} for neutral-point control in FCS-MPC should be evaluated under different operating conditions. Once the adaptive frequency control method has been validated, the optimal value for λ_{dc} is determined by simulation-based heuristic approach: (1) the various simulations with a set of λ_{dc} values have been performed for different grid impedances and operating points, (2) the results obtained have been evaluated considering the DC-link voltage balance error and the output current THD as performance indicators, (3) the optimal λ_{dc} has been obtained for each test-case. The results obtained from heuristic approach show that optimal λ_{dc} is mainly determined by the operating point, whilst grid impedance has not a remarkable influence. Fig. 2.11 shows the obtained value of λ_{dc}, which mainly depends on the operating point. A look-up table (LUT) method can be used to

adapt the weight coefficient of the neutral-point balance control based on power converter operating point. The results show: (1) a tendency to big values for low currents, (2) a tendency to low values for medium-high currents, (3) there is a symmetrical behavior for ind/cap reactive points.

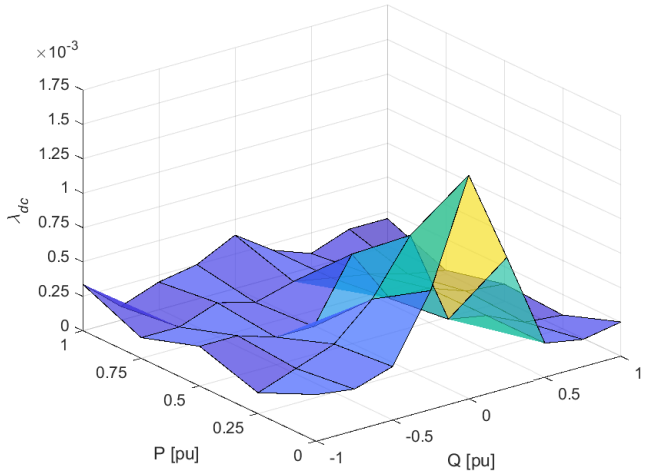

Fig. 2.11 Optimal λ_{dc} for different operating points.

2.3 Design of outer control loops

(1) Grid-synchronization structure

The phase-locked loop (PLL) is widely used for tracking grid angle and frequency from voltage measurement at PCC [62]. Significant efforts have been dedicated to enhance synchronization technology under unbalanced, faulty, or distorted grid conditions [63], [64]. The PLL plays a critical role in system stability [65], especially in weak grid conditions, which may cause negative damping within the low frequency range.

Compliance with modern grid codes necessitates the regulation of currents in both positive- and negative-sequence within a dual-decoupled control framework (check Section 2.4 for further details). To address this, a synchronization structure that can extract the positive- and negative-sequence of grid voltage is needed. The FQSG-PLL [66] depicted in Fig. 2.12 is the employed synchronization structure. It comprises a synchronous reference frame PLL (SRF-PLL) with a pre-filtering stage. The filtered quadrature signal generator (FQSG) estimates the instantaneous symmetrical components of the grid voltage in $\alpha\beta$-domain and provides additional harmonic

filtering capability. The impact of pre-filter on converter stability is analyzed in [67]. The positive-sequence component estimated by FQSG serves as input for the SRF-PLL.

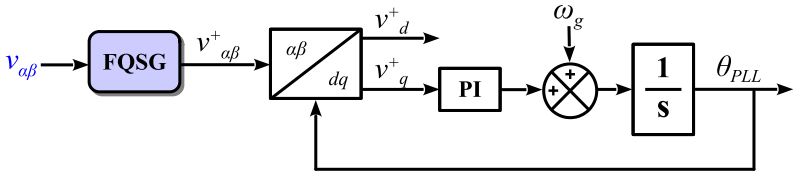

Fig. 2.12 Synchronization structure with pre-filter FQSG.

The dual second order generalized integrator (DSOGI) [62] has been extensively applied as sequence estimator, which offers a robust behavior against unbalanced and distorted grid voltages. The FQSG provides an equivalent dynamic but simplifies the structure of DSOGI. Fig. 2.13 shows the structure of the employed pre-filter FQSG.

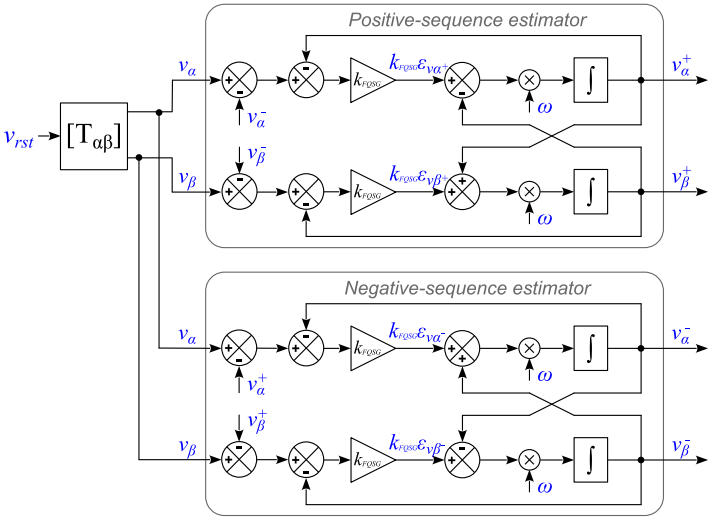

Fig. 2.13 Pre-filter FQSG structure.

The transfer function of FQSG is given as (23).

$$\begin{bmatrix} v_\alpha^+ \\ v_\beta^+ \\ v_\alpha^- \\ v_\beta^- \end{bmatrix} = \frac{k_{FQSG}\omega}{s^2 + 2k_{FQSG}\omega s + \omega^2} \begin{bmatrix} s & -\omega \\ \omega & s \\ s & \omega \\ -\omega & s \end{bmatrix} \begin{bmatrix} v_\alpha \\ v_\beta \end{bmatrix} \tag{23}$$

where the $v_{\alpha\beta}$ is the measured grid voltage in the $\alpha\beta$-frame, $v_{\alpha\beta}^{+}$ is the estimated positive-sequence, and $v_{\alpha\beta}^{-}$ is the estimated negative-sequence. ω is the grid frequency, and k_{FQSG} is the damping factor of the second-order filter.

Fig. 2.14 shows the frequency response of FQSG filter with different values of k for positive- and negative-sequence. The filtering capability of FQSG is modified by adjusting the gain k, which also limits the dynamic response of sequence estimation. A value of k = 0.35 is recommended as a trade-off between harmonic rejection and bandwidth of the FQSG pre-filter.

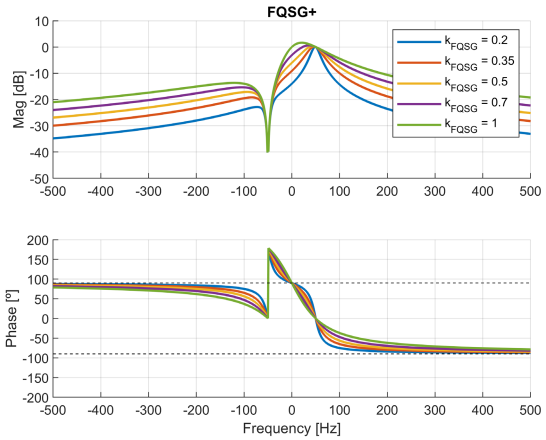

(a) Positive-sequence.

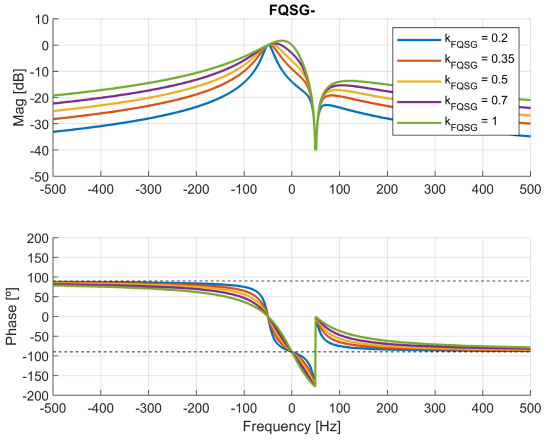

(b) Negative-sequence.

Fig. 2.14 Frequency response of FQSG filter.

The SRF-PLL tracks the grid voltage angle in order to establish the control *dq*-frame aligned with measured grid voltage vector in *d*-axis. This is achieved by considering *q*-axis component of measured grid voltage as the phase error of PLL, where the steady-state operation ensures $v_q = 0$. For a three-phase input signal, the phase detector is implemented by applying the park transformation as (24).

$$\begin{bmatrix} v_d \\ v_q \end{bmatrix} = V \begin{bmatrix} \cos(\theta - \theta_{PLL}) \\ \sin(\theta - \theta_{PLL}) \end{bmatrix} \tag{24}$$

where the signal v_q contains phase-error information and can be linearized as (25).

$$\varepsilon_\omega = v_q = V\, sin(\theta - \theta_{PLL}) \approx V(\theta - \theta_{PLL}) \tag{25}$$

The amplitude V appears as a gain in the phase error signal. Therefore, it is recommended to normalize the amplitude of input signal to maintain the dynamic characteristics of SRF-PLL. The v_q signal is then passed through PI controller to obtain the estimated frequency ω_{PLL}. Finally, phase angle is derived as (26).

$$\theta_{PLL} = \int \omega_{PLL} dt \tag{26}$$

The closed-loop transfer function of SRF-PLL can be derived from the linearized small-signal model as (27).

$$G_{PLL}(s) = \frac{\theta_{PLL}(s)}{\theta(s)} = \frac{k_p s + \frac{k_p}{T_i}}{s^2 + k_p s + \frac{k_p}{T_i}} \tag{27}$$

The closed-loop transfer function $G_{PLL}(s)$ is analogous to a second order system, which adds filtering capability to high-frequency noise in the input signal. Furthermore, the PLL tuning can be determined for a desired settling time $t_s = \frac{4.6}{\xi \omega_n}$.

$$\begin{aligned} k_{pPLL} &= 2\xi\omega_n = \frac{9.2}{t_s} \\ T_{iPLL} &= \frac{2\xi}{\omega_n} = \frac{t_s \xi^2}{2.3} \end{aligned} \tag{28}$$

(2) DC-link voltage controller

The DC-link voltage controller generates the active current reference $i^+_{P\_ref}$ for the power converter based on DC-link voltage error. Fig. 2.15 illustrates the configuration of the DC-link voltage controller, comprising: (a) the normalized DC-link voltage error with respect to the grid voltage, (b) the DC current feedforward action I_{dc},

determined by the active power generated on the machine side, and (c) the active current limitation $limI_P^+$, which will be discussed in the following section.

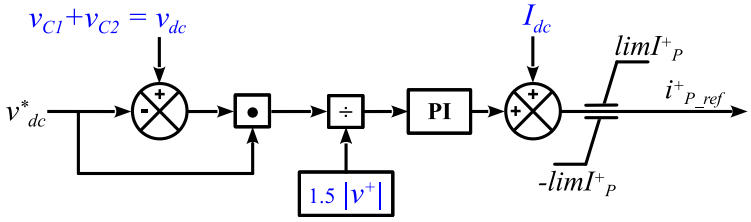

Fig. 2.15 DC-link voltage controller.

2.4 Development of fault ride-through capability

This section investigates the fault ride-through (FRT) capability of 3L-NPC inverter with proposed MPC strategy, which is based on publications **C2** and **J2**. The grid codes demand the wind turbine to stay operational and support the grid with reactive power under a temporary voltage drop. Reactive power requirements of modern grid codes involve current injection in both positive- and negative-sequence [68]. During the fault, priority may be given to reactive power, while active power output from the grid-side converter is drastically reduced. The slow response of the mechanical system makes the machine-side converter to maintain the active power injection to the power converter. The active power must be restored to pre-fault values once the voltage is recovered.

2.4.1 Generation of current reference

Current references are generated according to the flexible positive and negative sequence control (FPNSC) [69]. First, grid code requirements for reactive power provision are analyzed. Second, converter current and voltage constraints are considered to calculate the limiting values for current references. Finally, the dual-decoupled current references are transformed into the $\alpha\beta$-frame for current regulation.

During a voltage sag or swell event, reactive power should be supplied to enable FRT operation in both positive- and negative-sequence. The reactive current references are generated as (29).

$$\begin{aligned} i^+_{Q\_ref} &= k^+ \cdot \Delta|v^+| \\ i^-_{Q\_ref} &= k^- \cdot \Delta|v^-| \end{aligned} \tag{29}$$

where $i^{+}_{Q\_ref}$ is the reactive current reference in positive-sequence, $i^{-}_{Q\_ref}$ is the reactive current reference in negative-sequence, and k^{+} and k^{-} denote the gains for grid voltage deviations $\Delta|v^{+}|$ and $\Delta|v^{-}|$. Grid operators determine these proportional gains within the range of $0 \leq k \leq 6$ to configure grid voltage support capability. Fig. 2.16 shows the reactive current injection profile for dynamic voltage support.

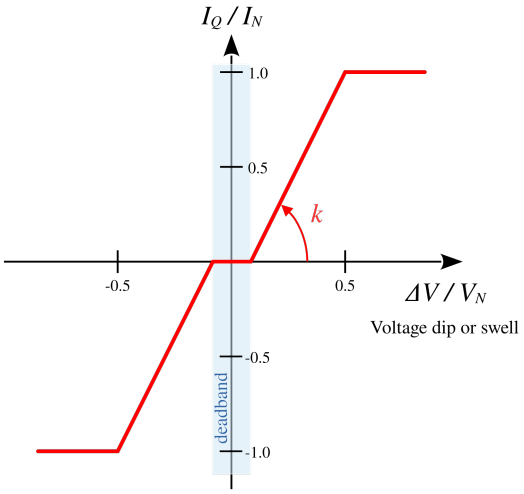

Fig. 2.16 Dynamic reactive current injection profile during over-voltage or under-voltage operation. Source [J2].

(1) Current reference boundaries

The power converter has both voltage and current limitations, which must be considered to grant the proper performance of the system. The thermal current limit I_{max} is determined by operating condition or supported overload [70]. This protection may be defined by a proper limitation of the current references to allow full current controllability of the grid-side converter. Current references in the positive- and the negative-sequence can be then specified within the current constraint as (30).

$$
\begin{aligned}
&|I^{+}| + |I^{-}| \leq I_{max} \\
&|I^{+}| = \sqrt{\left(I^{+}_{P\_ref}\right)^2 + \left(I^{+}_{Q\_ref}\right)^2} \\
&|I^{-}| = \sqrt{\left(I^{-}_{P\_ref}\right)^2 + \left(I^{-}_{Q\_ref}\right)^2}
\end{aligned}
\tag{30}
$$

where I_{max} is the maximum current, $|I^{+}|$ is the current reference amplitude in the positive-sequence, defined by its components for active current ($I^{+}_{P\_ref}$) and reactive

current ($I^+_{Q\_ref}$), and $|I^-|$ is the current reference amplitude in the negative-sequence, defined by its components for active current ($I^-_{P\_ref}$) and reactive current ($I^-_{Q\_ref}$).

As active current in negative-sequence is set to zero ($I^-_{P\_ref} = 0$), the equation (30) can be rewritten as (31).

$$\sqrt{\left(I^+_{P\_ref}\right)^2 + \left(I^+_{Q\_ref}\right)^2} + I^-_{Q\_ref} \leq I_{max} \tag{31}$$

The current references are prioritized to satisfy converter current constraint. Considering that grid-code compliance determines $I^+_{Q\_ref}$ and $I^-_{Q\_ref}$, the cascade-limits for current references are given as (32)-(34).

$$limI^-_Q = I_{max} \tag{32}$$

$$limI^+_Q = I_{max} - I^-_{Q\_ref} \tag{33}$$

$$limI^+_P = \sqrt{\left(limI^+_Q\right)^2 - \left(I^+_{Q\_ref}\right)^2} \tag{34}$$

where $limI^-_Q$ is the limit for the reactive current reference in negative-sequence $I^-_{Q\_ref}$, $limI^+_Q$ is the limit for the reactive current reference in positive-sequence $I^+_{Q\_ref}$, and $limI^+_P$ is the limit for the active current reference in positive-sequence $I^+_{P\_ref}$.

The power converter output voltage capability is determined by DC-link voltage as $|U| \leq \frac{V_{dc}}{\sqrt{3}}$. To maintain output voltage inside power converter limits, a maximum value I^+_{QMax} for positive-sequence reactive current is defined as (35).

$$I^+_{QMax} = \frac{1}{\omega L_f}\left(\frac{V_{dc}}{\sqrt{3}} - |v^+| - |v^-|\right) - I^-_{Q\_ref} \tag{35}$$

Fig. 2.17 shows the total current formed by addition of positive- and negative-sequences. The resulting asymmetrical current is represented as elliptical in $\alpha\beta$-frame.

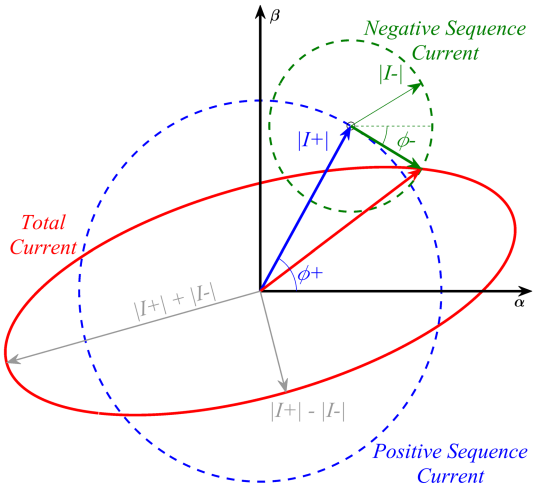

Fig. 2.17 Elliptical current reference in $\alpha\beta$-frame, formed by positive- and negative-sequence current. Source [J2].

(2) Operating condition during severe grid faults

The grid codes demand fault ride-through capability during zero-voltage situations, which further complicates the control strategy in terms of stability and grid synchronization. During severe grid faults, operating point of power converter is changed, and PLL needs to capture a new stable equilibrium point. The transient instability occurs when there is no stable point during the fault, and PLL is unable to maintain synchronization with the grid. This phenomenon, defined as loss of synchronism (LOS), is analyzed in [71]. Various strategies have been proposed to overcome this issue, including modifications to PLL control structure and optimizing current injection profiles [64].

During grid faults, the active current transfer limit depends on PCC voltage and grid reactance, which is unknown and time-varying with grid conditions. In [72], a reduction of active current is proposed to mitigate the risk of loss of synchronism during severe grid faults. To further improve performance, the modification of PLL parameters has been proposed in several studies. The simplest approach is the PLL freezing method [73], which nullifies the PLL control error when a severe fault is detected. This method ensures stable operation even under zero-voltage conditions.

2.4.2 Current controller reference

The fundamental components of instantaneous active and reactive power are defined as (36) by positive- and negative-sequence components of grid voltage and current injected into the grid by the power converter.

$$\begin{bmatrix} {P_0}^+ \\ {Q_0}^+ \end{bmatrix} = \frac{3}{2} \cdot \begin{bmatrix} v_d^+ & v_q^+ \\ v_q^+ & -v_d^+ \end{bmatrix} \cdot \begin{bmatrix} i_d^+ \\ i_q^+ \end{bmatrix}$$
$$\begin{bmatrix} {P_0}^- \\ {Q_0}^- \end{bmatrix} = \frac{3}{2} \cdot \begin{bmatrix} v_d^- & v_q^- \\ v_q^- & -v_d^- \end{bmatrix} \cdot \begin{bmatrix} i_d^- \\ i_q^- \end{bmatrix} \quad (36)$$

where P_0^+, Q_0^+, P_0^-, and Q_0^- are the active and reactive power fundamental components; v_d^+, v_q^+, v_d^-, and v_q^- are the grid voltage components obtained from the FQSG-PLL; and i_d^+, i_q^+, i_d^-, and i_q^- are power converter currents in *dq*-frame.

The active and reactive power can be derived from positive- and negative-sequence current reference as (37).

$$\begin{aligned} {P_0}^+ &= {}^3\!/_2 \cdot |v^+| \cdot i_{P\_ref}^+ \\ {Q_0}^+ &= {}^3\!/_2 \cdot |v^+| \cdot i_{Q\_ref}^+ \\ {P_0}^- &= 0 \\ {Q_0}^- &= -{}^3\!/_2 \cdot |v^-| \cdot i_{Q\_ref}^- \end{aligned} \quad (37)$$

The current reference in *dq*-frame can be obtained by combining (36) and (37), resulting in (38) and (39) for positive- and negative-sequence, respectively.

$$\begin{aligned} \begin{bmatrix} i_{d\_ref}^+ \\ i_{q\_ref}^+ \end{bmatrix} &= \frac{1}{{}^3\!/_2 \cdot |v^+|^2} \cdot \begin{bmatrix} v_d^+ & v_q^+ \\ v_q^+ & -v_d^+ \end{bmatrix} \cdot \begin{bmatrix} {P_0}^+ \\ {Q_0}^+ \end{bmatrix} \\ &= \frac{1}{|v^+|} \cdot \begin{bmatrix} v_d^+ & v_q^+ \\ v_q^+ & -v_d^+ \end{bmatrix} \cdot \begin{bmatrix} i_{P\_ref}^+ \\ i_{Q\_ref}^+ \end{bmatrix} \end{aligned} \quad (38)$$

$$\begin{aligned} \begin{bmatrix} i_{d\_ref}^- \\ i_{q\_ref}^- \end{bmatrix} = \frac{1}{{}^3\!/_2 \cdot |v^-|^2} \cdot \begin{bmatrix} v_d^- & v_q^- \\ v_q^- & -v_d^- \end{bmatrix} \cdot \begin{bmatrix} {P_0}^- \\ {Q_0}^- \end{bmatrix} &= \frac{1}{{}^3\!/_2 \cdot |v^-|^2} \cdot \begin{bmatrix} v_q^- \\ -v_d^- \end{bmatrix} \cdot {Q_0}^- \\ = \frac{1}{|v^-|} \cdot \begin{bmatrix} -v_q^- \\ v_d^- \end{bmatrix} \cdot i_{Q\_ref}^- & \end{aligned} \quad (39)$$

As the FQSG-PLL is synchronized with positive-sequence, the q-axis component can be disregarded ($v_q^+ \approx 0$), and (38)-(39) can be expressed as (40)-(41).

$$\begin{aligned} i_{d\_ref}^{+} &= +\frac{v_d^+}{|v^+|} i_{P\_ref}^{+} \\ i_{q\_ref}^{+} &= -\frac{v_d^+}{|v^+|} i_{Q_{ref}}^{+} \end{aligned} \tag{40}$$

$$\begin{aligned} i_{d\_ref}^{-} &= -\frac{v_q^-}{|v^-|} i_{Q\_ref}^{-} \\ i_{q\_ref}^{-} &= +\frac{v_d^-}{|v^-|} i_{Q\_ref}^{-} \end{aligned} \tag{41}$$

The MPC regulates grid currents in the $\alpha\beta$-frame. Therefore, current references are transformed from dual-decoupled control framework to $\alpha\beta$-frame using the inverse-Park transform with the positive-sequence voltage angle θ_{PLL} as (42)-(44).

$$\begin{aligned} i_{\alpha}^{*} &= i_{\alpha\_ref}^{+} + i_{\alpha\_ref}^{-} \\ i_{\beta}^{*} &= i_{\beta\_ref}^{+} + i_{\beta\_ref}^{-} \end{aligned} \tag{42}$$

$$\begin{aligned} i_{\alpha\_ref}^{+} + j \cdot i_{\beta\_ref}^{+} &= e^{+j\theta_{PLL}} \cdot \left(i_{d\_ref}^{+} + j \cdot i_{q\_ref}^{+}\right) \\ i_{\alpha\_ref}^{+} &= i_{d\_ref}^{+} \cdot \cos\theta_{PLL} - i_{q\_ref}^{+} \cdot \sin\theta_{PLL} \\ i_{\beta\_ref}^{+} &= i_{d\_ref}^{+} \cdot \sin\theta_{PLL} + i_{q\_ref}^{+} \cdot \cos\theta_{PLL} \end{aligned} \tag{43}$$

$$\begin{aligned} i_{\alpha\_ref}^{-} + j \cdot i_{\beta\_ref}^{-} &= e^{-j\theta_{PLL}} \cdot \left(i_{d\_ref}^{-} + j \cdot i_{q\_ref}^{-}\right) \\ i_{\alpha\_ref}^{-} &= i_{d\_ref}^{-} \cdot \cos\theta_{PLL} + i_{q\_ref}^{-} \cdot \sin\theta_{PLL} \\ i_{\beta\_ref}^{-} &= -i_{d\_ref}^{-} \cdot \sin\theta_{PLL} + i_{q\_ref}^{-} \cdot \cos\theta_{PLL} \end{aligned} \tag{44}$$

The current reference in $\alpha\beta$-frame can be obtained by combining (40)-(43) and (41)-(44), resulting in (45) and (46) for positive- and negative-sequence, respectively.

$$\begin{aligned} i_{\alpha\_ref}^{+} &= \frac{v_d^+}{|v^+|} i_{P\_ref}^{+} \cdot \cos\theta_{PLL} + \frac{v_d^+}{|v^+|} i_{Q\_ref}^{+} \cdot \sin\theta_{PLL} \\ i_{\beta\_ref}^{+} &= \frac{v_d^+}{|v^+|} i_{P\_ref}^{+} \cdot \sin\theta_{PLL} - \frac{v_d^+}{|v^+|} i_{Q\_ref}^{+} \cdot \cos\theta_{PLL} \end{aligned} \tag{45}$$

$$i_{\alpha\_ref}^{-} = -\frac{v_q^-}{|v^-|} i_{Q\_ref}^- \cdot \cos\theta_{PLL} + \frac{v_d^-}{|v^-|} i_{Q\_ref}^- \cdot \sin\theta_{PLL} \tag{46}$$

$$i_{\beta\_ref}^{-} = +\frac{v_q^-}{|v^-|} i_{Q\_ref}^- \cdot \sin\theta_{PLL} + \frac{v_d^-}{|v^-|} i_{Q\_ref}^- \cdot \cos\theta_{PLL}$$

where $i_{\alpha\_ref}^{+}$ and $i_{\beta\_ref}^{+}$ are current references in positive-sequence, $i_{\alpha\_ref}^{-}$ and $i_{\beta\_ref}^{-}$ are current references in negative-sequence, and i_{α}^{*} and i_{β}^{*} are the total current references in $\alpha\beta$-frame.

The flowchart diagram of the proposed FRT strategy is presented in Fig. 2.18.

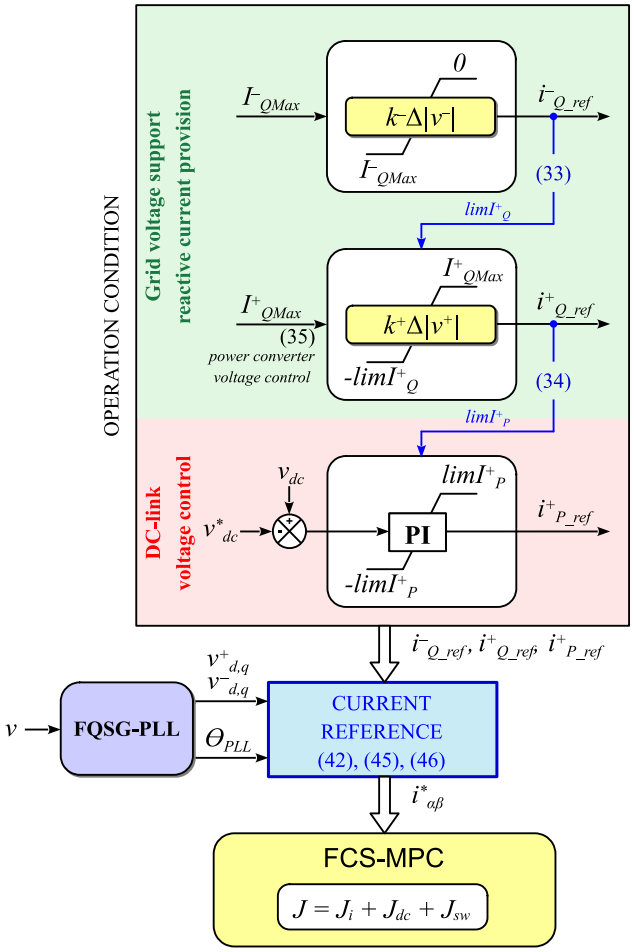

Fig. 2.18 Flowchart diagram of the proposed FRT strategy. Source: [J2].

2.4.3 Experimental results

The proposed FRT control strategy undergoes real-time hardware-in-the-loop (HiL) experimental verification to validate its effectiveness. The HiL experimental platform is depicted in Fig. 2.19. The controller is implemented within a *dSPACE DS1006* real-time digital processor with a sampling time of 50μs. The *PLECS RT Box* emulates the 3L-NPC converter and power grid with a step size of 10μs. Two peripheral boards connect the real-time digital processor and the *PLECS RT Box.* Specifically, the *DWO DS5101* generates gating signals produced by MPC, while the *ADC DS2004* handles measured signals, including grid voltage/current and DC-link voltages.

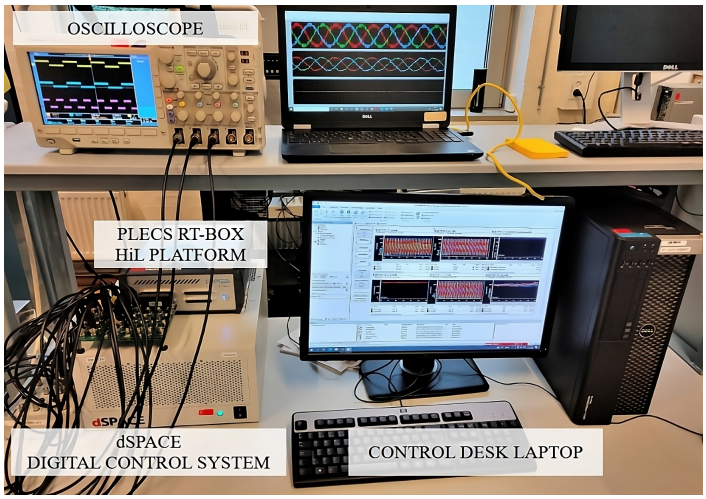

Fig. 2.19 Hardware-in-the-loop experimental platform. Source: [J2].

Fig. 2.20 presents the experimental results of both low-voltage ride-through (LVRT) and high-voltage ride-through (HVRT) operation. The grid phase voltages (V_g) and currents (I_g), the DC-link capacitor voltage (v_{C1}, v_{C2}), and the sequence components of grid current ($I_{g\text{-}seq}$) are displayed. In Fig. 2.20(a), the experimental results for a 3-phase 0% LVRT scenario reveal the injection of reactive current in the positive-sequence to support voltage restoration. Fig. 2.20(b) shows the experimental results for a 2-phase 0% LVRT scenario, where the control strategy reacts to the unbalanced grid fault by injecting reactive current in the positive sequence and absorbing reactive current in the negative sequence. During LVRT operation, active current reduction occurs, and the activation of braking chopper circuit limits the rise in DC-link capacitor voltage caused by power imbalance. In Fig. 2.20(c), the experimental results for a 3-phase 130% HVRT scenario reveal the absorption of reactive current in the positive-sequence to mitigate grid voltage swell. Fig. 2.20(d)

shows the experimental results for a 2-phase 130% HVRT scenario, where both positive- and negative-sequence reactive current are absorbed. During HVRT operation, there exists no power imbalance, as active power can be delivered into the power grid.

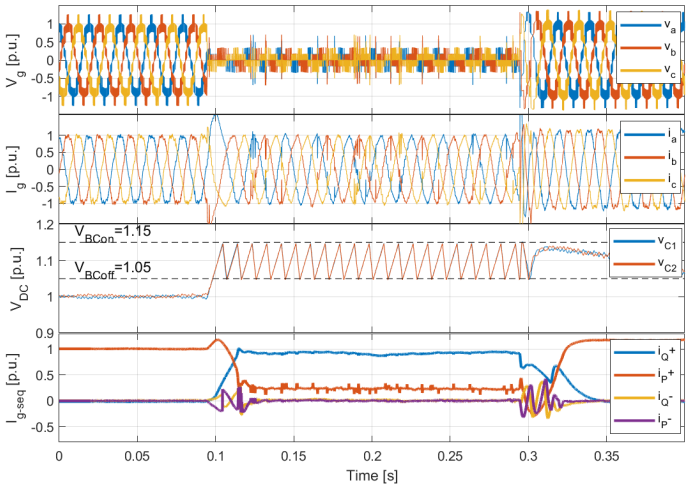

(a) 3-phase 0% LVRT.

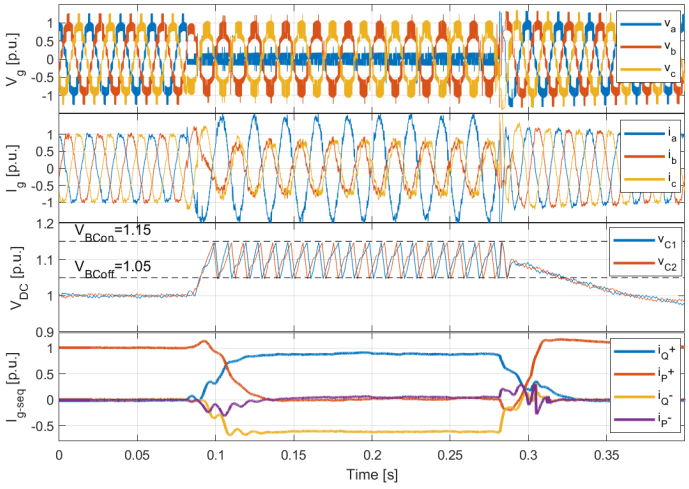

(b) 2-phase 0% LVRT.

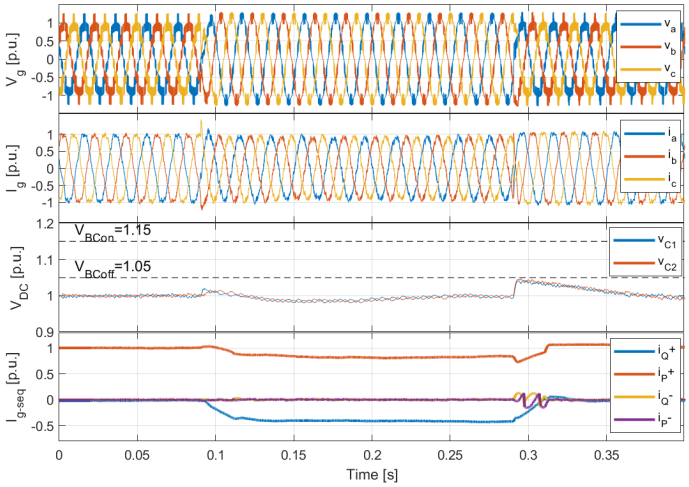

(c) 3-phase 130% HVRT.

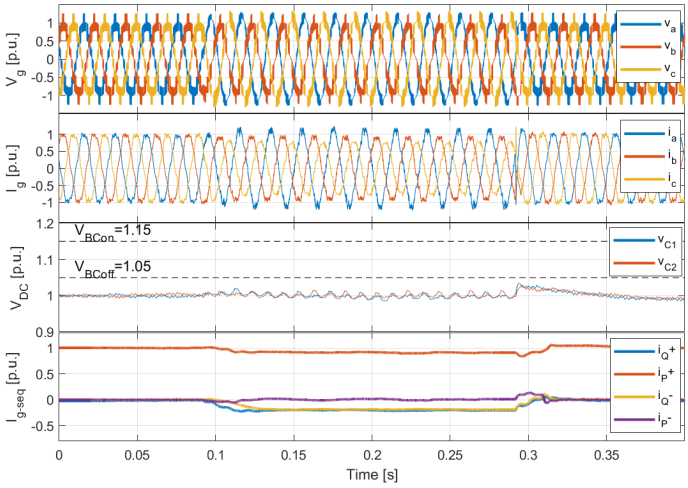

(d) 2-phase 130% HVRT.

Fig. 2.20 Grid voltage, grid current, capacitor voltage measurements, and sequence components of grid current in experimental platform during different grid faults. Source: [J2].

Both simulation and experimental results from publications **C2** and **J2** validate the effectiveness of the proposed operation strategy for LVRT and HVRT. The reactive current provision for grid voltage support aligns with the requirements of most recent grid codes. The capability of the MPC to perform fast and accurate FRT operation of high-power wind power converter is thus demonstrated.

2.5 Robustness analysis of FCS-MPC

This section analyzes the robustness of FCS-MPC, which is based on **C3**. The FCS-MPC strategy is dependent on the quality of the mathematical model of the system [74]. Therefore, the accuracy of derived discrete model will determine the performance of the controller. Despite some studies have proven that FCS-MPC is robust against system parameter variations and perturbations [75]–[77], parameter uncertainties and model inaccuracy may cause imprecise predictions. The prediction model of grid-connected inverters is primarily defined by grid filter inductor, whose characteristics can be altered by tolerances in the manufacturing process, temperature variations, magnetic saturation [78], and degradation over time [79].

2.5.1 Effect of grid filter parameter mismatch

The nonlinear nature of FCS-MPC complicates the robustness analysis. Therefore, evaluating the performance of FCS-MPC under uncertain conditions often relies on empirical assessment. However, the impact of filter inductor variations on current prediction error can be modeled in a similar approach as proposed in [80]. The current prediction model can incorporate uncertain terms to represent the influence of filter inductor variations as (47).

$$\hat{\imath}_{(k+1)} = \left(1 - \frac{T_s\left(\sigma_R R_f\right)}{\sigma_L L_f}\right) i_{(k)} + \frac{T_s}{\sigma_L L_f}\left[v_{o(k)} - v_{g(k)}\right] \tag{47}$$

where $\hat{\imath}_{(k+1)}$ is the predicted current when uncertain values of filter inductor are considered in control model. R_f and L_f are the real values for filter resistance and inductance, respectively, while σ_R and σ_L represent the uncertain components in controller parameterization.

The current prediction error Δi is defined in (48) as the difference between the prediction from the error-free model and that incorporating uncertain parameters.

$$\begin{gathered} \Delta i = i_{(k+1)} - \hat{\imath}_{(k+1)} \\ \Delta i = \frac{T_s}{\sigma_L L_f}\left[(\sigma_R - \sigma_L) R_f i_{(k)} + (\sigma_L - 1)\left(v_{o(k)} - v_{g(k)}\right)\right] \end{gathered} \tag{48}$$

The prediction error Δi is also influenced by the instantaneous values of grid current $i_{(k)}$ and the difference between converter output voltage $v_{o(k)}$ and grid voltage $v_{g(k)}$. Furthermore, employing a lower sampling period T_s leads to a decrease

in the magnitude of prediction error, enhancing the robustness of the predictive controller.

The variation in magnitude and relative angle of current and voltage vectors generates diverse scenarios for prediction errors. Fig. 2.21 shows the ratio of current prediction error $|\Delta i_k|/|i_k|$ for different parameter mismatches in the grid filter. In Fig. 2.21(a), magnitude of current prediction error is presented as function of relative angle when parameter uncertainty in grid filter inductance exists. In Fig. 2.21(b), magnitude and relative angle of voltage vectors are fixed to simplify the analysis. The results reveal a limited dependence on resistance mismatch, whereas variations in grid filter inductance present a stronger and asymmetric impact. Specifically, prediction error increases when the inductance parameter is lower than the actual value $(L_0 < L_f)$. Further, current prediction error varies with relative angle of voltage vectors, reaching its maximum value for angles close to π rad.

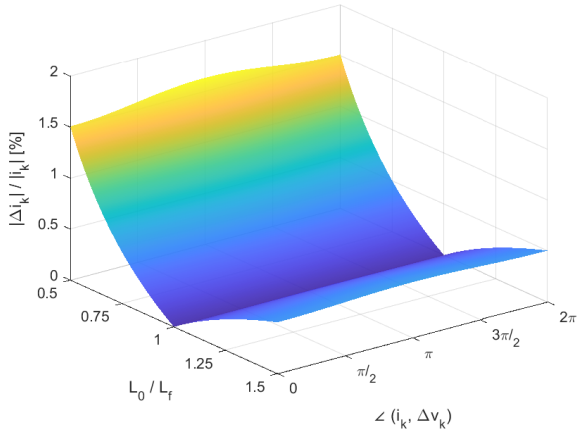

(a) Magnitude of current prediction error as function of relative angle between voltage vectors.

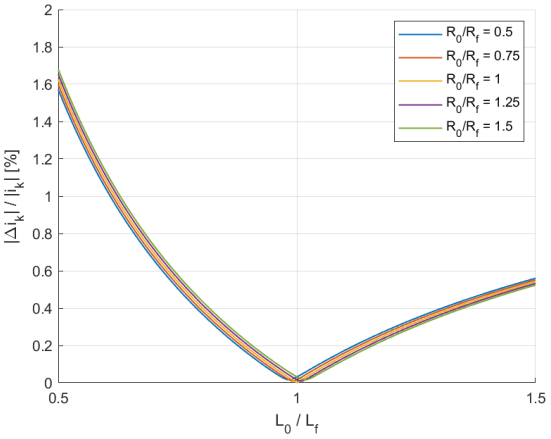

(b) Magnitude of current prediction error for fixed angle.

Fig. 2.21 The ratio of current prediction error for different levels of uncertainty in grid filter. Source [C3].

Grid-current THD is utilized as a metric to evaluate the performance of FCS-MPC in the presence of grid filter parameterization errors. Fig. 2.22 presents the simulation results for the converter operating at rated active power and various reactive power levels, when grid filter parametric errors are included. The actual values of grid filter resistance R_f and inductance L_f remain unaltered to preserve system plant configuration. The control model is parameterized with R_0 and L_0, whose values vary in the range from 50% to 150%. Fig. 2.22(a) reveals that a higher current THD is obtained when the controller underestimates grid filter inductance $(L_0 < L_f)$, exhibiting the asymmetric impact of current prediction error. Fig. 2.22(b) demonstrates the minimal influence of resistance value on current THD. In both cases, the reactive power level exhibits no impact on current THD.

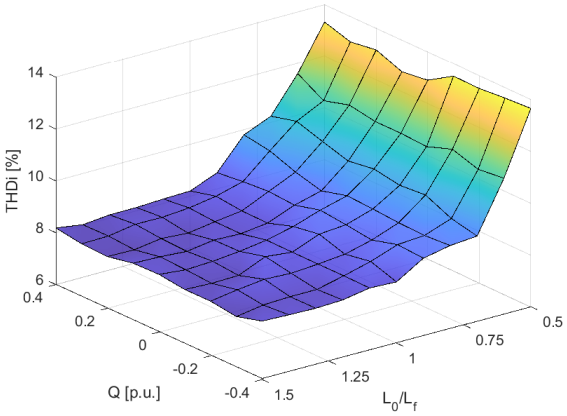

(a) Grid filter inductance parametric mismatch.

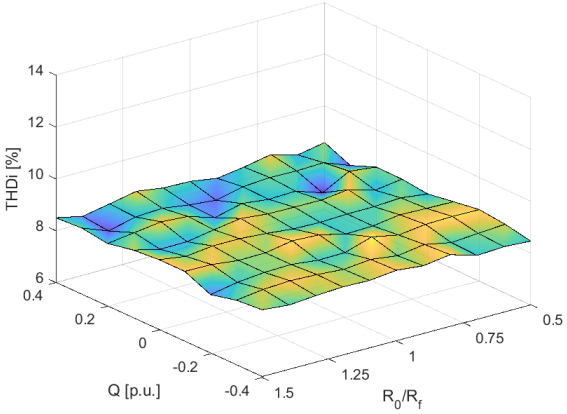

(b) Grid filter resistance parametric mismatch.

Fig. 2.22 The current THD of 3L-NPC converter with grid filter parameter error. Source [C3].

2.5.2 Design of grid filter inductor parameter observer

The use of a disturbance observer can mitigate performance degradation resulting from parameter mismatch. The extended Kalman filter (EKF) has been proven effective in power electronics as a robust state observer in the presence of parameter uncertainties [81]. The EKF extends the traditional Kalman filter to nonlinear systems by linearizing the system at a specific operating point, enabling the application of

linear estimation techniques [82]. Utilizing Kalman filtering for parameter estimation results in a system identification problem, where system equations depend on system parameters. The discrete-time system can be represented as (49).

$$\begin{aligned} \mathrm{x_k} &= \mathrm{f}(\mathrm{x_{k-1}}, \mathrm{u_{k-1}}) + \mathrm{w_k} \\ \mathrm{y_k} &= \mathrm{h}(\mathrm{x_k}) + \mathrm{v_k} \end{aligned} \tag{49}$$

where $x = \left(i_\alpha, i_\beta, R_f, L_f\right)^T$ is the state vector, $y = \left(i_\alpha, i_\beta\right)^T$ is the measurement vector, and $u = \left(v_o^\alpha - v^\alpha, v_o^\beta - v^\beta\right)^T$ is the input vector. The process and measurement noise are represented by w_k and v_k, respectively. Both are assumed to be independent random variables, exhibiting white noise characteristics and normal probability distributions. The process noise covariance matrix $Q := E\{w_k \cdot w_k^T\}$ and the measurement noise covariance matrix $R := E\{v_k \cdot v_k^T\}$ are treated as constants for simplicity. The measurement equation h links the state x to the measurement y. The function f is obtained from the discrete-time model of the 3L-NPC inverter as (50).

$$f(x,u) = \begin{bmatrix} i_\alpha \\ i_\beta \\ R_f \\ L_f \end{bmatrix} + T_s \begin{bmatrix} -\frac{R_f}{L_f} i_\alpha + \frac{1}{L_f}(v_o^\alpha - v^\alpha) \\ -\frac{R_f}{L_f} i_\beta + \frac{1}{L_f}\left(v_o^\beta - v^\beta\right) \\ 0 \\ 0 \end{bmatrix} \tag{50}$$

The EKF operates recursively to estimate the state vector x_k, which is not directly accessible. Kalman filter calculates *a posteriori* state estimation $\hat{x}_k^+$ by combining an *a priori* estimation $\hat{x}_k^-$ (prediction step) with a weighted difference between the actual measurement y_k and the predicted measurement (correction step). The accuracy of the predictions generated by Kalman filter depends on the precise formulation of the discrete-time model. Any unmodeled system dynamics (e.g., unexpected delays) are interpreted as process noise, resulting in poorer parameter identification.

The description of the discrete-time EKF algorithm. Source [C3].

The EKF algorithm

Initialization of the filter

$$\hat{x}_0^+ = E(x_0)$$
$$P_0^+ = E\left((x_0 - \hat{x}_0^+)(x_0 - \hat{x}_0^+)^T\right)$$

STEP I: Prediction (time update)

(1) Compute the partial derivative matrix.

$$F_{k-1} = \left.\frac{\partial f_{k-1}}{\partial x}\right|_{\hat{x}_{k-1}^+}$$

(2) Perform the time update of the state prediction.

$$\hat{x}_k^- = f_{k-1}(\hat{x}_{k-1}^+, u_{k-1})$$

(3) Perform the time update of the error covariance matrix prediction.

$$P_k^- = F_{k-1} \cdot P_{k-1}^+ \cdot F_{k-1}^T + Q$$

STEP II: Correction (measurement update)

(1) Computation of Kalman gain.

$$K_k = \frac{P_k^- \cdot H_k^T}{H_k \cdot P_k^- \cdot H_k^T + R}$$

(2) Perform the measurement update of the estate estimation.

$$\hat{x}_k^+ = \hat{x}_k^- + K_k(y_k - H_k\hat{x}_k^-)$$

(3) Perform the measurement update of the error covariance matrix.

$$P_k^+ = P_k^- - K_k \cdot H_k \cdot P_k^-$$

The Jacobian H_k defines the relationship between measurement y_k and state x_k. The Kalman gain K_k is computed to minimize the *a posteriori* error covariance.

It has been demonstrated that FCS-MPC is sensitive to variations in grid filter parameters. Therefore, precise model parameterization is crucial to prevent deterioration in control performance. An estimation algorithm should be then incorporated to overcome parameter uncertainties or variations. Fig. 2.23 shows the FCS-MPC strategy augmented with EKF observer. The EKF is utilized for estimating the actual values of grid filter parameters, and the FCS-MPC is then fed with the estimations $\hat{R}_f$ and $\hat{L}_f$.

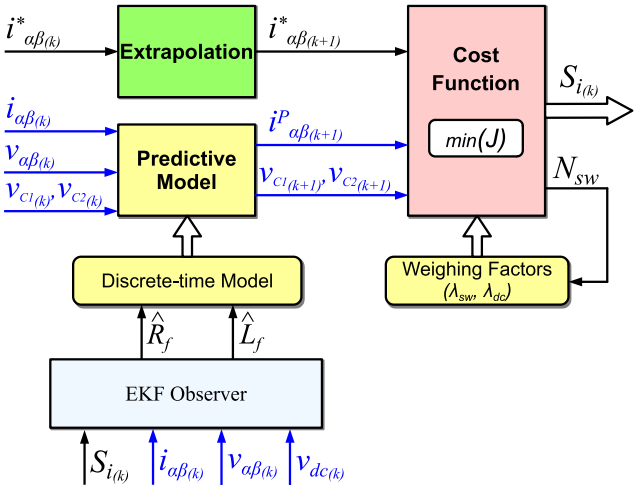

Fig. 2.23 The principle of FCS-MPC strategy with EKF observer. Source [C3].

The covariance matrices Q and R are adjusted from trial-and-error approach supported by tuning guidelines [83]. Multiple simulation tests are conducted to determine the parameter settings for matrices R and Q that yield satisfactory performance in estimating grid filter parameters.

Fig. 2.24 presents the results obtained when errors are introduced into the parameterization of the MPC controller. The 3L-NPC converter operates at rated active power with an initial parameter mismatch in the controller, set as $R_0 = 0.5R_f$ and $L_0 = 0.5L_f$. The EKF initiates background operation at $t = 1s$, and the MPC is enhanced by EKF estimations for $t > 3s$. Fig. 2.24(a) shows the converter operating point, DC-link voltage, and average switching frequency. Fig. 2.24(b) validates the performance of EKF as parameter estimator by successfully estimating the actual value of the grid filter. In Fig. 2.24(c), the current THD (*THDi*) and the current tracking error (e_α, e_β) are displayed for different time intervals. The results indicate that the parametric accuracy provided by EKF improves FCS-MPC performance, resulting in a reduction of *THDi* from *0.129* to *0.085*, as well as a decrease in both e_α (from *0.097* to *0.062*) and e_β (from *0.093* to *0.0615*).

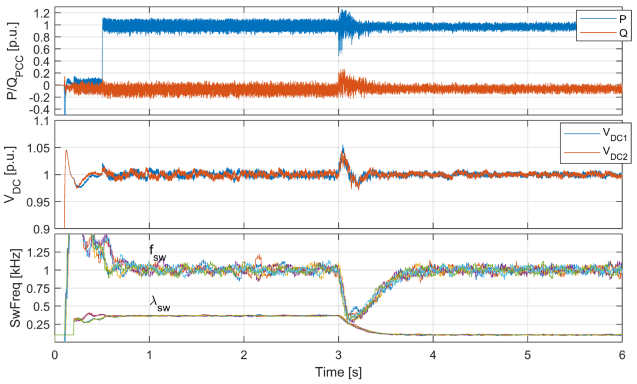

(a) Operating point of converter.

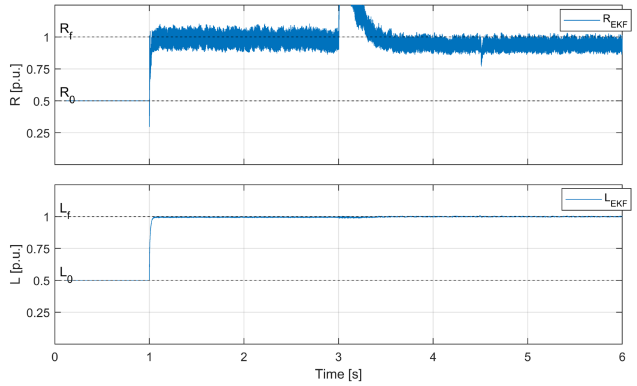

(b) Performance of EKF.

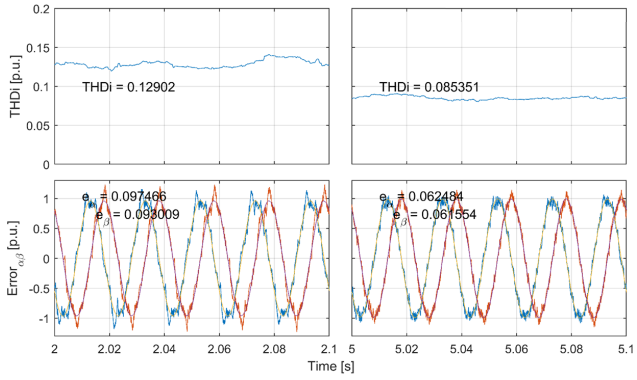

(c) Current waveform and THD.

Fig. 2.24 Simulation results for a parameterization error in the MPC controller. Source [C3].

2.6 Summary

In this chapter, the application of FCS-MPC to the grid-side control of 3L-NPC converter for high-power wind turbine is investigated. The multi-objective cost function of MPC controller is designed to perform current regulation, neutral-point voltage balancing, and control of switching frequency.

The novel switching frequency control strategy with self-tuning variable weight λ_{sw} is developed to maintain switching frequency at target value. Therefore, tuning process is simplified, limitations of fixed tuning of λ_{sw} are revealed, and time-consuming empirical methods are avoided. The proposed method is effective under time-variant conditions and enables online regulation of average switching frequency. This capability may be further exploited to optimize thermal stress of power converter.

The fault ride-through control strategy based on MPC is developed. The voltage support capability is demonstrated under symmetrical and asymmetrical grid faults and the fast dynamic response of MPC enables the reactive current injection in less than 20ms. Both simulation and hardware-in-the-loop experimental verification are implemented, and effectiveness of proposed MPC-based control strategy to improve FRT performance of high-power wind turbine during grid faults is validated.

The robustness analysis of FCS-MPC is performed. MPC exhibits sensitivity to uncertainties in model parameters and converter performance (e.g., current THD) can be degraded in presence of filter parameter mismatch. Therefore, model accuracy is essential to avoid deterioration in control performance. The FCS-MPC scheme is then augmented with Extended Kalman Filter as state observer to identify grid filter inductor parameters. The capability of proposed robust MPC strategy to enhance controller performance against parametric uncertainties or variations is verified.

Table 2.3: *Summary of 3L-NPC output voltage vector and corresponding switching states.*

	Voltage Vector	Switching Vector	Upper-leg switching orders						Num. adjacent vectors
No.	**V**	**s_{abc}**	**s_{a1}**	**s_{a2}**	**s_{b1}**	**s_{b2}**	**s_{c1}**	**s_{c2}**	**_NumEvalVect**
1	V0	[0 0 0]	0	0	0	0	0	0	4
2	V0	[1 1 1]	0	1	0	1	0	1	7
3	V0	[2 2 2]	1	1	1	1	1	1	4
4	V1	[1 0 0]	0	1	0	0	0	0	5
5	V1	[2 1 1]	1	1	0	1	0	1	6
6	V2	[1 1 0]	0	1	0	1	0	0	6
7	V2	[2 2 1]	1	1	1	1	0	1	5
8	V3	[0 1 0]	0	0	0	1	0	0	5
9	V3	[1 2 1]	0	1	1	1	0	1	6
10	V4	[0 1 1]	0	0	0	1	0	1	6
11	V4	[1 2 2]	0	1	1	1	1	1	5
12	V5	[0 0 1]	0	0	0	0	0	1	5
13	V5	[1 1 2]	0	1	0	1	1	1	6
14	V6	[1 0 1]	0	1	0	0	0	1	6
15	V6	[2 1 2]	1	1	0	1	1	1	5
16	V7	[2 0 0]	1	1	0	0	0	0	4
17	V8	[2 1 0]	1	1	0	1	0	0	5
18	V9	[2 2 0]	1	1	1	1	0	0	4
19	V10	[1 2 0]	0	1	1	1	0	0	5
20	V11	[0 2 0]	0	0	1	1	0	0	4
21	V12	[0 2 1]	0	0	1	1	0	1	5
22	V13	[0 2 2]	0	0	1	1	1	1	4
23	V14	[0 1 2]	0	0	0	1	1	1	5
24	V15	[0 0 2]	0	0	0	0	1	1	4
25	V16	[1 0 2]	0	1	0	0	1	1	5
26	V17	[2 0 2]	1	1	0	0	1	1	4
27	V18	[2 0 1]	1	1	0	0	0	1	5

_NumEvalVect is the number of adjacent vectors when only one switching action is allowed. This imposes the number of possible vector candidates employed for optimization.

3. STABILITY ANALYSIS OF 3L-NPC INVERTER WITH THE PROPOSED MPC

In this chapter, stability of grid-connected 3L-NPC inverter with the proposed MPC is analyzed, which is based on publication **J3**. First, the principle of impedance-based stability analysis is introduced. Second, the details of developed frequency-scan technique for impedance measurement are given. The use of single-tone frequency-scan approach and corresponding setup configuration is proposed. Third, the impedance characteristic 3L-NPC inverter with MPC is analyzed, and passivity concept is employed to evaluate the impact of controller design on stability. Finally, the simulation analysis of the offshore wind farm case study is conducted, and the advantages of the proposed control strategy for stability enhancement are clarified.

3.1 Principle of impedance-based stability analysis

The instability of grid-connected inverter can be caused by the dynamic interaction of inner control loops with time-varying power grid conditions [84]. The impedance-based stability analysis evaluates the stability of grid-connected inverter by identifying if the ratio of inverter output impedance (Z_0) to the equivalent grid impedance (Z_g) meets the Nyquist criterion. The impedance-based approach emphasizes the stability caused by the interconnections of system components by examining their terminal behaviors (e.g., impedance or admittance of inverter) [85]. The impedance models can be derived in *dq*-domain [86] and sequence-domain [87]. Their relationship as a linear transformation is demonstrated in [88] and the stability analysis is not affected by the choice of impedance domain. Much previous works on stability of power electronic converters have been performed in *dq* coordinates.

In impedance-based method, a system is divided into a source subsystem and a load subsystem. The source and load *dq*-domain impedance matrices are given by expression (51). Fig. 3.1 shows the equivalent diagram of the grid-connected inverter in synchronous *dq*-domain.

$$Z_{S_{dq}} = \begin{bmatrix} Z_{S_{dd}}(s) & Z_{S_{dq}}(s) \\ Z_{S_{qd}}(s) & Z_{S_{qq}}(s) \end{bmatrix}$$
$$Z_{Ldq} = \begin{bmatrix} Z_{Ldd}(s) & Z_{Ldq}(s) \\ Z_{Lqd}(s) & Z_{Lqq}(s) \end{bmatrix} \quad (51)$$

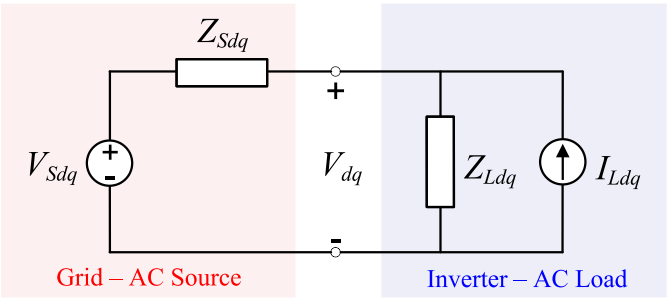

Fig. 3.1 The equivalent diagram of the grid-connected inverter in synchronous *dq*-domain.

The minor loop gain concept is applied in assessing the stability in interconnected power electronic systems [89]. The minor loop gain denotes the ratio of the upstream and downstream impedances. The closed-loop stability can be assessed by applying the Generalized Nyquist Criterion [90] to the eigenvalues of the minor loop gain derived from (52).

$$det\left(I + Z_{Sdq}(s) \cdot Y_{Ldq}(s)\right) = 0 \tag{52}$$

"For a closed-loop system to be stable, the encirclement, if any, of the $(-1,0)$ *point by the Nyquist plot of the open-loop transfer function (as s moves along the Nyquist path) must be anticlockwise, and the number of such encirclements must be equal to the number of poles of the open-loop transfer function that lie on the right-half-plane (RHP)".*

3.2 Impedance measurement technique

The existing impedance-based methods tend to require a detailed small-signal model of the power system and control system. However, detailed information of control architecture and parameters may be kept confidential by manufacturers. Then, data-based black-box approach provides a good solution, where models can be built based on measured output dynamics of components [91]. For non-linear controllers such as FCS-MPC, traditional modeling procedures are no longer effective, and frequency-scan method [92] is then proposed for the stability analysis. The frequency-scan analysis is able to derive the impedance-model of power converter from measurements at its terminals, without the need of detailed physical or control information. To accomplish this, the system is perturbed with a small disturbance and its response to this disturbance is measured. Then, impedance-model can be computed.

The series voltage injection is recommended for grid-connected inverter characterization [93]. Fig. 3.2 shows the circuit setup with voltage disturbance injection (V_{inj}). The injection of two linearly independent perturbation signals is required to calculate the 2x2 impedance matrix. The impedance characteristic of the converter (Z_0) and the grid impedance (Z_g) are obtained by measuring terminal voltages and currents (v_L, i_L, v_S, i_S).

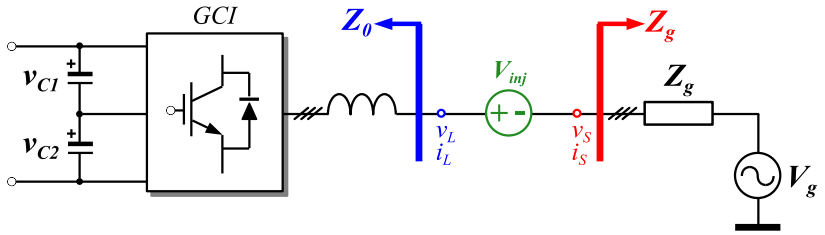

Fig. 3.2 The diagram of 3L-NPC with voltage disturbance injection. Source [J3].

3.2.1 Single-tone frequency-scan

In the single-tone frequency-scan approach, the system is perturbed by a single frequency signal each time, and its response is then captured to determine the impedance at the injection frequency. By repeating the measurement for a set of frequencies, the impedance characteristic is then obtained. The single-tone frequency-scan is the most intuitive and widespread method for impedance measurement. The sinusoidal injection method concentrates all the energy of the injection at a single frequency, which offers the highest noise immunity and highest signal-to-noise ratio and minimizes the cross-coupling between frequencies, so that the most accurate estimation of impedance is achieved. The drawback of this method is that the system needs to reach steady-state for each injected single-frequency before the frequency response can be captured, which is highly time-consuming and not recommended for real applications. The use of wideband perturbation signals is then proposed to reduce the overall experimentation time and guarantee constant operating conditions. Various types of wideband perturbation signals have been implemented for impedance measurement, such as the Chirp signal [94], the pseudo-random binary sequence (PRBS) signal [95], and the discrete-interval binary sequence (DIBS) signal [96]. However, broadband perturbation signals are more susceptible to background noise since power spectrum is spread over a wide frequency range and are prone to lose accuracy in the high-frequency range. Therefore, in this PhD Project, the single-tone frequency-scan technique is chosen to obtain the most precise impedance characteristics of the grid-connected inverter operated with FCS-MPC. The principle of frequency-scan technique is well established in [97], [98] as follows. (1) The grid-

connected inverter is operated at desired steady-state condition, (2) single-tone perturbation frequency sweep starts, (3) measured currents and voltages are transformed into *dq*-domain by applying Park transformation with fundamental voltage angle, (4) components induced by injected perturbation are extracted by Fast Fourier Transform (FFT), (5) impedance matrices at perturbation frequency are calculated. The flowchart of single-tone frequency-scan method is presented in Fig. 3.3, where the process to obtain impedance characteristic in *dq*-domain is given.

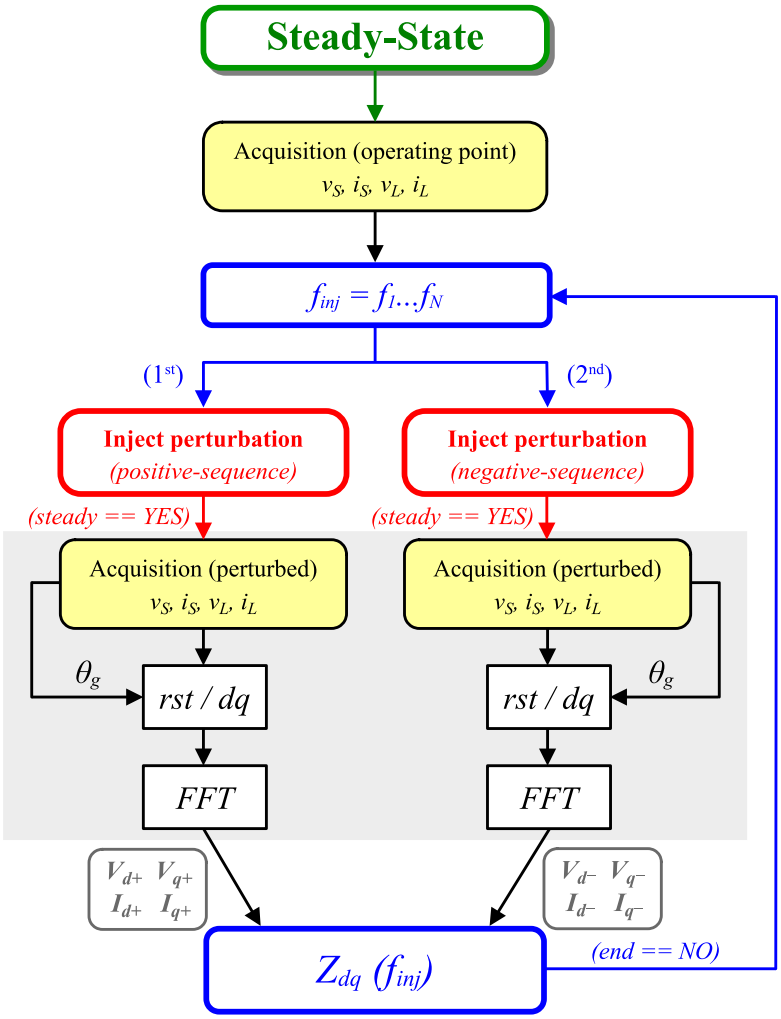

Fig. 3.3 Flowchart of the single-tone frequency-scan method in *dq*-domain.

The impedance of converter (Z_0) is computed for each injected frequency based on Fourier analysis as (53).

$$Z_0(j\omega) = \frac{F\left[V_{ppc_{inj}}\right]}{F\left[I_{ppc_{inj}}\right]} = \frac{V_{ppc_{inj}}(j\omega)}{I_{ppc\_inj}(j\omega)} \tag{53}$$

where F denotes the Fourier transformation, V_{pcc_inj} is the disturbance voltage injected at PCC, and I_{pcc_inj} is the current response excited by the disturbance voltage.

3.2.2 Recommended setup configuration for frequency-scan

This setup configuration is recommended to get accurate measurement of impedance of grid-connected inverter.

1) Simulation should be run with fixed-step size and the simulation time step must be sufficiently small to precisely capture the quickest dynamics. In this PhD Project, the time step of 10μs is employed as a tradeoff between accurate impedance identification and experiment duration.

2) The voltage perturbation signal is injected superposed on the operating condition. The magnitude of perturbation signal must be small enough to maintain system linearity, yet strong enough to provide useful feedback with a reasonable signal-to-noise ratio. There is no straightforward guideline for selecting the amplitude; typically, trial-and-error within the range of 1%-5% is employed.

3) The steady-state condition must be reached within the time span employed for FFT to deter impedance calculation from being corrupted by transients. The duration needed to reach steady-state depends on system dynamics.

4) The length of the voltage and current vectors sampled for FFT must be exactly an integer number of fundamental frequency periods to minimize spectral leakage effect.

5) The measured input and output data is processed to reduce impact of background harmonics and enhance impedance identification accuracy. This involves subtracting the steady-state quantities from the perturbed system voltage and current to isolate the small-signal delta change [99]. Additionally, a band-pass prefilter is applied to measurements, focusing on the frequency target of interest.

3.2.3 Impedance identification of series RL-circuit

The *dq*-domain impedance matrix of series RL-circuit is presented in Fig. 3.4. The results obtained from frequency-scan simulation are compared with analytical expression (54) in order to validate the proposed black-box method for impedance measurement.

$$Z_{RL_{dq}}(j\omega) = \begin{bmatrix} R & 0 \\ 0 & R \end{bmatrix} + \begin{bmatrix} j\omega L & -\omega_g L \\ +\omega_g L & j\omega L \end{bmatrix} \tag{54}$$

where ω is the angular frequency, $\omega_g = 2\pi \cdot 50$ is the rated angular frequency, and $R = 3.1\Omega$ and $L = 0.1\text{H}$ are the employed parameter values.

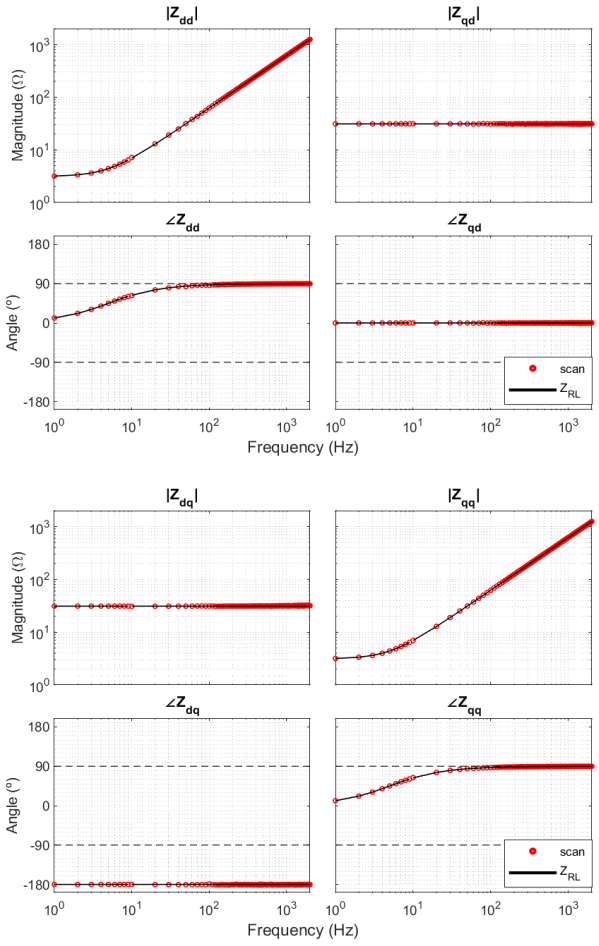

Fig. 3.4 *dq*-domain impedance matrix of series RL-circuit with R = 10, L = 10 mH.

3.3 The proposed impedance analysis of FCS-MPC

The frequency-domain impedance characteristics are derived from detailed electromagnetic-transient (EMT) models, which can be then employed to evaluate stability without using mathematical model. The single-tone frequency-scan defined in previous section is performed by means of time-domain simulation in *Matlab/Simulink*. The impedance characteristic of grid-connected inverter (GCI) with FCS-MPC is analyzed under different controller design conditions as shown in Fig. 3.5.

Passivity theory can be used to assess stability of power electronic-based power systems since passivity provides a sufficient stability condition for interconnected dynamic systems [100]. The passivity concept imposes specific requirements for each individual inverter to guarantee the overall system stability [101]. Considering the 2x2 input impedance matrix $Z_{dq}(s)$ representation, the power converter is passive if it is internally stable and $Z_{conv}(j\omega) + Z_{conv}^{H}(j\omega) > 0 \ \forall\omega$, where $Z_{conv}^{H}(j\omega)$ is the complex-conjugate transpose (Hermitian transpose) of $Z_{conv}(j\omega)$. Under these conditions, there is no negative real part of the impedance $Z_{conv}(j\omega)$, the phase response is limited within the range ±90º, and the power converter does not contribute to any possible resonance interaction in the system. To investigate the impact of FCS-MPC on stability, only Z_{dd} and Z_{qq} are evaluated, since power converter behavior is diagonal-dominant [102]. The studied frequency range extends from 200Hz to 2.5kHz since low-frequency instability is mainly caused by dynamic characteristics of outer control loops such as PLL and DC-link voltage controller.

(1) Impact of sampling time

Fig. 3.5(a) shows the stability impact of sampling time T_s, when J_i is the only control objective in cost function. To decouple the effect of sampling time from cost function design, the current control J_i is the unique control objective considered in MPC cost function. Under these conditions, there is no neutral-point balance control. Thus, DC-link capacitors are replaced by constant DC voltage sources and DC-link voltage controller must be then disabled. The GCI is operated at rated active power (*P = 5MW, Q = 0*) and SCR is *10.* The various frequency-scan tests have been performed to obtain the impedance of GCI when MPC controller is configured with different sampling time T_s *= 30, 50, 80, 100, 120, and 150μs*. For $T_s < 80\mu s$, the passive behavior of GCI is ensured for the whole frequency range as the phase response of Z_{dd} and Z_{qq} is kept within the range $\pm\frac{\pi}{2}$. However, for the case of $T_s = 150\mu s$, the passive region is limited up to *1.5kHz*. Therefore, the benefits of minimizing sampling time to expand the passive region of power converter are demonstrated. Furthermore, the uncontrolled switching frequency is obtained, where

the only limitation is the own sampling time T_s. For the case of $T_s = 50\,\mu s$, the switching frequency reaches up to *5kHz*, which is out of specification because of the increased switching losses.

(2) Impact of cost function

Switching frequency control J_{sw} and neutral-point balancing control J_{dc} are required for NPC operation. The addition of these control objectives in cost function imposes constraints, which weakens the preference of current tracking error term J_i. Thus, impedance characteristic and corresponding stability can be affected. Fig. 3.5(b) shows the impact of sampling time T_s on stability when all control objectives are considered in cost function. The GCI is operated at rated active power *(P = 5MW, Q = 0)* and SCR is *10.* The various frequency-scan tests have been performed to obtain impedance characteristic of GCI when the MPC controller is configured with different sampling time T_s *= 30, 50, 80, 100, 120, and 150*μs. Compared with results presented in Fig. 3.5(a), the cut-off frequencies for non-passive regions are similar. However, the shape of Z_{dd} and Z_{qq} varies when additional control objectives J_{sw} and J_{dc} are included in cost function. The main difference in impedance shape is exhibited when $T_s < 80\mu s$, while the slight difference coincides with the highest sampling time values. This behavior is mainly caused by switching frequency control J_{sw}, whose weight value within cost function is higher for low T_s.

(3) Impact of grid impedance

Grid impedance can affect performance of MPC as demonstrated in [60]. The self-tuning strategy of λ_{sw} is then required to maintain switching frequency at specified value of 1kHz, where the higher value of λ_{sw} is needed under high SCR conditions, and the lower value of λ_{sw} is needed under low SCR conditions. Fig. 3.5(c) shows the influence of SCR on impedance characteristic of GCI. The sampling time is set as $T_s = 50\mu s$ and the GCI is operated at rated active power *(P = 5MW, Q = 0).* The various frequency-scan tests have been performed under different *SCR = 1.2, 1.5, 2, 3, 5, 10, and 20.* The passive condition of GCI operated by FCS-MPC is maintained for the whole SCR range. The value of Z_{dd} presents significant variations for the lowest values of SCR, when the weight of the switching frequency control J_{sw} is lower. The impact of SCR on Z_{qq} is lower, where it can be observed for values of $SCR < 3$.

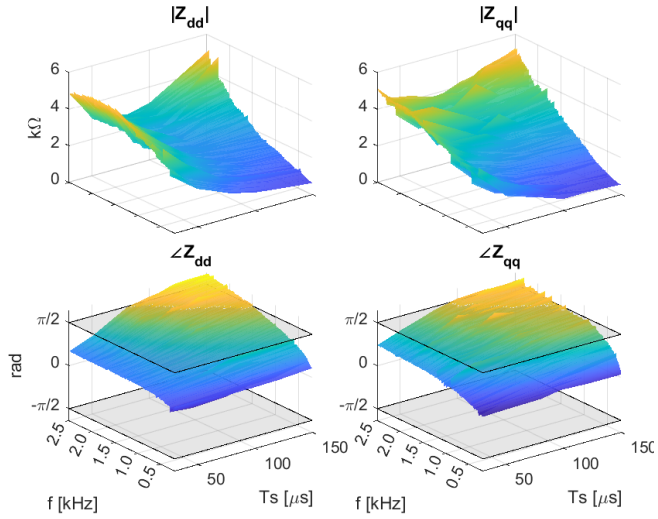

(a) Different sample time (T_s), when the current control (J_i) is the only control objective in cost function.

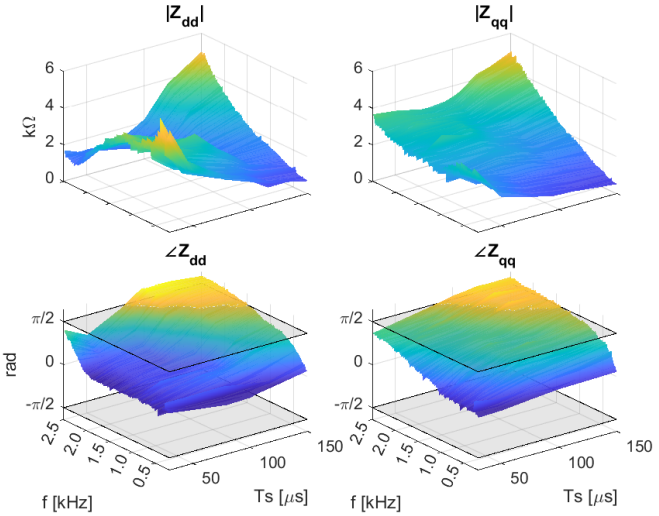

(b) Different sample time (T_s), when all constraints are considered in cost function.

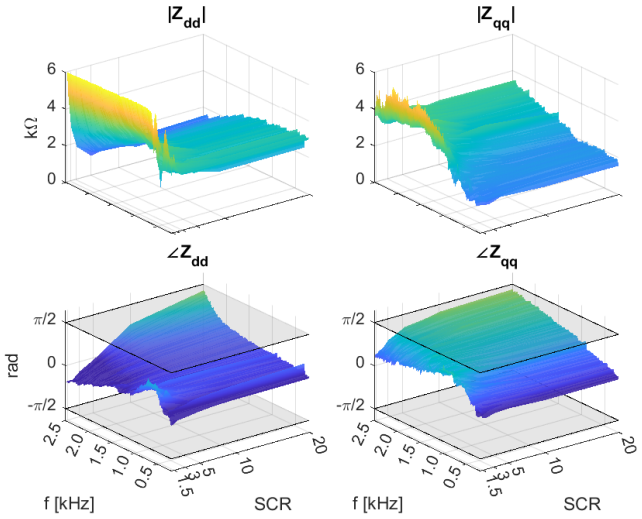

(c) Different grid impedance (*SCR*).

Fig. 3.5 The *dq*-domain impedance characteristic of GCI with FCS-MPC obtained by frequency-scan under different conditions. Source [J3].

3.4 Simulation analysis of the proposed control strategy

In this section, time-domain simulation is implemented to validate the proposed MPC strategy. The advantage of the proposed control strategy for stability enhancement is investigated in Alpha Ventus OWPP [103]. Fig. 3.6 shows the diagram of Alpha Ventus OWPP. The offshore wind farm has a total capacity of 60 MW, which consists of 12 type-4 wind turbines (WT). Eleven WTs consist of 3L-NPC converter and LCL filter with RL damping circuit. These WTs are controlled by classical PI current controller in *dq*-frame with PWM modulation. The WT No. 3 is enabled by the proposed solution. The detailed information on modeling approach and parameters for this scenario can be seen in [104]. To emulate the performance of long transmission cable, the Frequency-Dependent π-equivalent model and parameterization process shown in [105] is adopted.

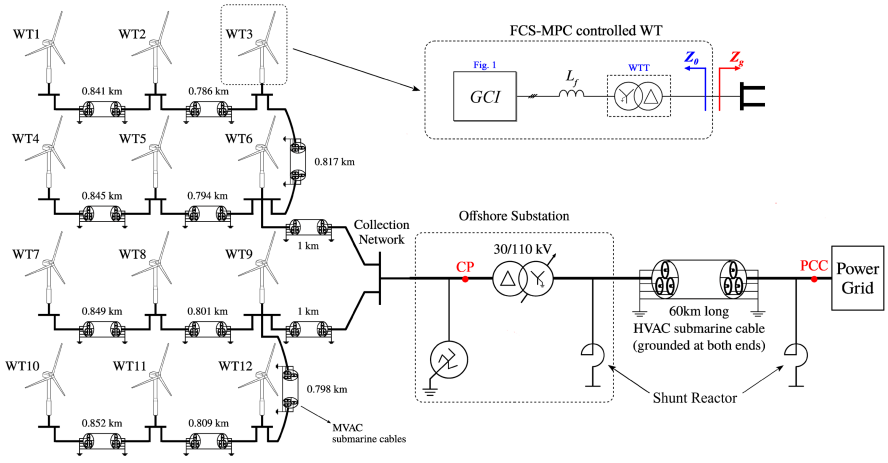

Fig. 3.6 Diagram of Alpha Ventus offshore wind farm with the proposed control solution. Source [J3].

The simulation results of Alpha Ventus OWPP are presented in Fig. 3.7. The Alpha Ventus OWPP is initially operated with 11 classical PI-controlled WTs, where the power rating of each WT is 5MW. At *0.4s*, the WT No. 3 with the proposed MPC control is enabled to deliver active power as shown in Fig. 3.7(a). WT No. 3 can be stably operated without resonance phenomenon in output voltage and current. Fig. 3.7(b) shows the steady-state operation of Alpha Ventus OWPP when all the WTs are operated at rated active power. The results show that whole OWPP can be stably operated. The voltage V_{PCC} and current I_{PCC} waveforms at PCC exhibit no resonance phenomenon. Almost the 60MW generated by the 12 WTs are delivered to power grid, and the 5MVAR are absorbed.

The increase in rated power or transmission impedance reduces SCR and grid strength, potentially leading to instability [106]. When all the 12 WTs are operated by classical PI current controller and grid impedance is increased at *0.6s*, the resonance is triggered and the behavior of OWPP is unstable as shown in Fig. 3.7(c). However, the advantage of MPC for stability enhancement is validated when some of the WTs are replaced with the proposed MPC-based solution. Fig. 3.7(d) shows the simulation results when 6 WTs (WT No. 1, 2, 3, 7, 8, and 9) are operated with MPC. It can be seen that there are no resonance phenomena in output voltage and current. The case study shows that stability of OWPP under weak grid condition can be enhanced by the proposed MPC control strategy.

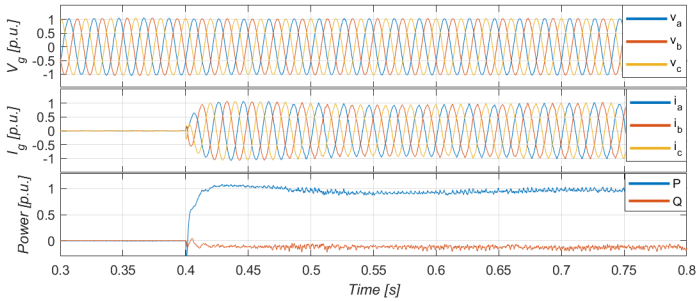

(a) System dynamics after WT No. 3 is enabled.

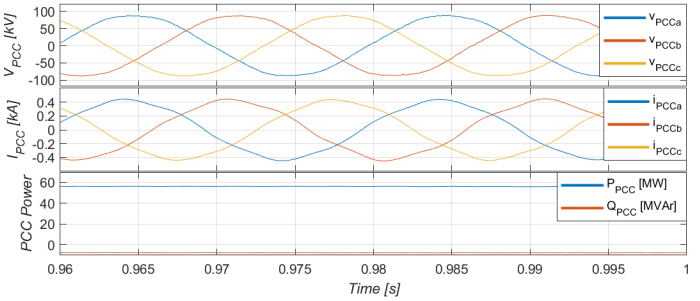

(b) Steady-state operation at rated power of Alpha Ventus OWPP.

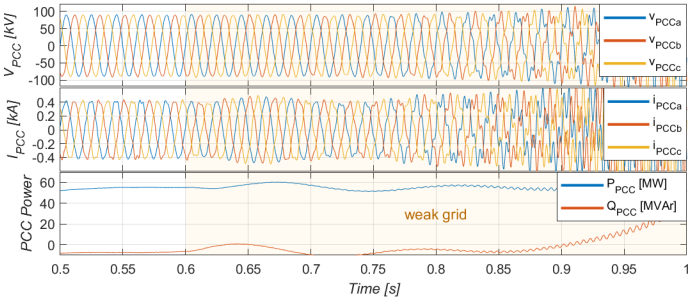

(c) Weak grid operation with 12 PI-controlled WTs.

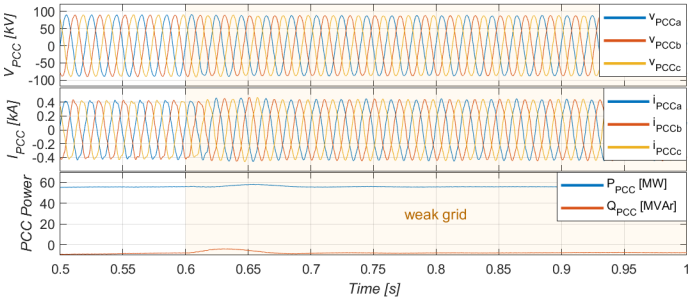

(d) Weak grid operation with 6 PI-controlled WTs and 6 MPC-controlled WTs.

Fig. 3.7 Simulation results of Alpha Ventus OWPP. Source [J3].

3.5 Summary

In this chapter, the stability issue of FCS-MPC and its application in offshore wind farm is explored. Since FCS-MPC lacks explicit mathematical model, the frequency-scan technique is proposed to derive impedance characteristic of MPC from terminal response of EMT simulations. The impedance analysis shows that reduction of sampling time in MPC can extend passive region of control system.

The case study of Alpha Ventus OWPP with proposed MPC control strategy is provided. The verification results show that MPC enables operating at low switching frequency with reduced sampling period. The inherent capability of MPC to perform multi-sampled control minimizes digital delays, which is especially advantageous for stability enhancement of high-power application with low switching frequency. Hence, the proposed control is a promising solution to improve stability of offshore high-power wind converter.

4. IMPLEMENTATION OF THE PROPOSED CONTROL STRATEGY IN INGETEAM POWER CONVERTER SOLUTION

In this chapter, the proposed control strategy is implemented and demonstrated in Ingeteam commercialized power converter solution, which is reported in publication **C4**. Fig. 4.1 shows the employed electrical drive train topology, which is based on two paralleled conversion lines. This configuration extends the power rating and enhances system robustness and reliability, which is a key factor in offshore market.

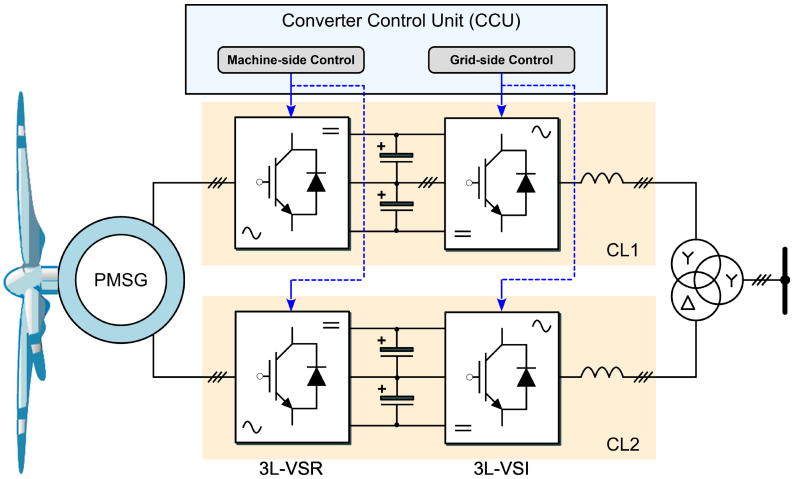

Fig. 4.1 Type 4 PMSG WECS with two ANPC conversion lines. Source [C4].

Ingeteam has developed a product line for high-power wind turbines designed to meet the stringent requirements of the offshore market, the *INGECON®WIND 7.5 MW FC MV power converter* shown in Fig. 4.2. Initially, the converter is designed with a power rating of 6 MW using a 3L-NPC topology. However, to extend the power rating up to 7.5 MW without external changes, the topology of Basic Power Modules (BPM) was evolved into the ANPC. The ANPC converter replaces the clamping diodes of the 3L-NPC with active switches, leading to an optimal distribution of power losses and improved junction temperature uniformity among the semiconductor switches.

The proposed predictive control strategy is applicable for both the 3L-NPC and 3L-ANPC solutions, as the 3L-NPC can be considered as a simplified variant of 3L-ANPC. A detailed description about the combability of developed predictive control strategy for both power converter topologies is given in Section 4.1.5.

Fig. 4.2 *INGECON®WIND 7.5 MW FC MV power converter* [107].

Ingeteam is a world-leading independent solution provider for OEMs (Original Equipment Manufacturers), utilities and asset owners in the wind energy sector. The company is committed to providing high-quality and reliable power converters, Indar generators, control cabinets, SCADA systems, overhaul projects, Ingeteam spare parts, repairs, and technical support, as well as multibrand repair and refurbishment services for onshore and offshore wind turbines up to 18 MW.

4.1 Implementation of proposed FCS-MPC algorithm in Ingeteam wind controller firmware

The power electronic converter is a key component which is continuously evolving with new control strategies to comply with new requirements and improve overall performance. Thus, the adequate integration, validation, and testing of these algorithms within converter firmware becomes crucial. The robust firmware development methodology by Ingeteam [108] must be adopted to ensure the appropriate behavior of new firmware prior to be loaded in the converter control unit.

The software-in-the-loop (SiL) validation process emerges as an indispensable tool to evaluate the performance of new algorithms before implementation in actual firmware. The EMT modeling provides detailed representations of electrical and electronics components, which replicates the accurate dynamic behavior of power system during transient conditions. The software routines are encapsulated into an executable dynamic-link library (DLL) with the exact same source code that is deployed in the converter. This way, the control strategies can be thoroughly assessed and optimized. The simulated environment enables flexible modeling and avoids hardware limitations, thereby facilitating the investigation of interactions between control system and power electronics. Furthermore, detailed representation of power converter by means of DLL-EMT models is demanded by grid operators for their integration within wide-area power grid models, where the behavior of power converter can be evaluated without disclosing internal details on the control system architecture. However, SiL validation is limited as non-real-time control system is employed and source code is partially covered (mainly control algorithms). To overcome limitations of SiL, the validation procedure incorporates hardware-in-the-loop (HiL) testing. The Ingeteam HiL platform [Fig. 4.16] employs the actual CCU [Fig. 4.5] and the tested firmware is exactly the same as the one released to production. Therefore, HiL validation assesses the real-time performance of the power converter and provides the complete coverage in firmware testing.

In this chapter, the integration process of the FCS-MPC algorithm into the existing firmware is described. The new MPC-based control algorithm is built upon a foundation from an official firmware release while preserving the software structure of the product. The incorporation of the FCS-MPC algorithm is achieved through C-code programming of DSP. To ensure the robust real-time implementation, a comprehensive validation strategy is adopted, combining both SiL and HiL approaches. Furthermore, constraints posed by the CCU are addressed, such as computational burden or additional delays, which necessitate careful attention during the integration process.

Fig. 4.3 illustrates the comprehensive flowchart for transitioning from a research environment to an industrial product with specific emphasis on integrating the new algorithm into the official software release. The five steps have been followed to properly integrate the newly developed FCS-MPC algorithm into the software package within CCU.

(1) The FCS-MPC algorithm undergoes research and development within simplified EMT simulation environment, where modeling of entire system and control platform constraints (e.g., computational burden, delays, coding intricacies…) are overlooked. Within this context, the predictive control strategy is progressively

evolved to permit an exploration of its strengths. Also, weaknesses can be investigated under favorable conditions. Enhanced controller functionalities and system constraints can be gradually incorporated for individual impact assessment.

(2) The developed predictive control strategy is integrated into the software architecture. The new algorithm is coded using C programming language and replaces concerned code segment within DLL layer 2 (matching with DSP). Fig. 4.4 shows the real application firmware architecture and identifies the specific code segment, where the new FCS-MPC algorithm replaces both the linear current controller and the modulation stage within the grid-side control.

(3) The SiL validation process starts with the new algorithm incorporated into the DLL, which precisely represents CCU characteristics. The entire application, comprising the power converter, as well as generator, transformer, and grid, is modeled and validated in the DLL-EMT simulation environment. This step facilitates the validation and optimization of complete software containing the developed control strategy. The new controller performance is validated for the complete test routine according to application requirements.

(4) The HiL validation procedure involves the compilation of upgraded C-code for target DSP and the generation of complete software package for the CCU. This step holds significant importance due to the critical computational burden associated with predictive control approach. The CCU must run the entire program flow to assess computational workload and precisely adjust the task period. Step 2, Step 3, and Step 4 must be combined to refine code routines and achieve the most optimized software implementation (refer to Section 4.1.3 for further details), supporting the minimum task period required for predictive controller operation.

(5) The complete testing procedure is executed, culminating in the delivery of the fully validated software package for real-world application.

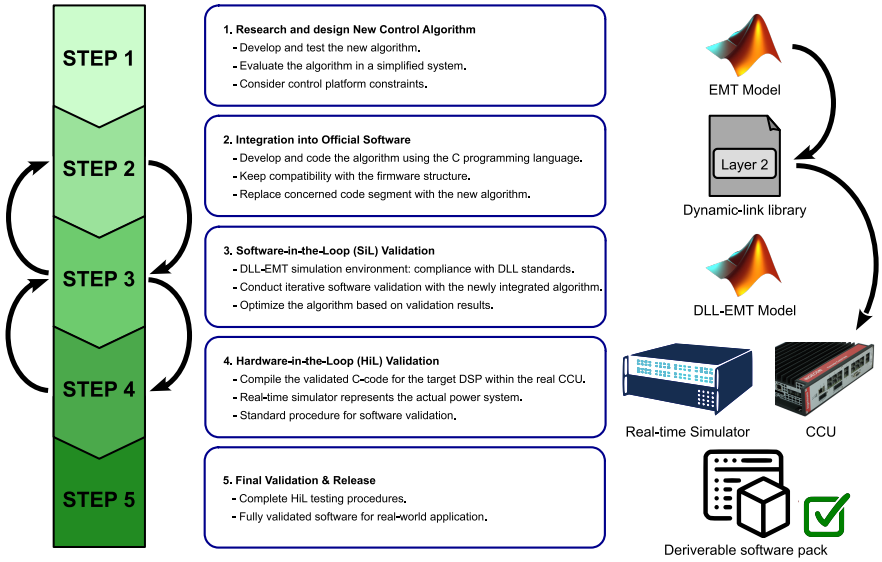

Fig. 4.3 Software development procedure employed in this project.

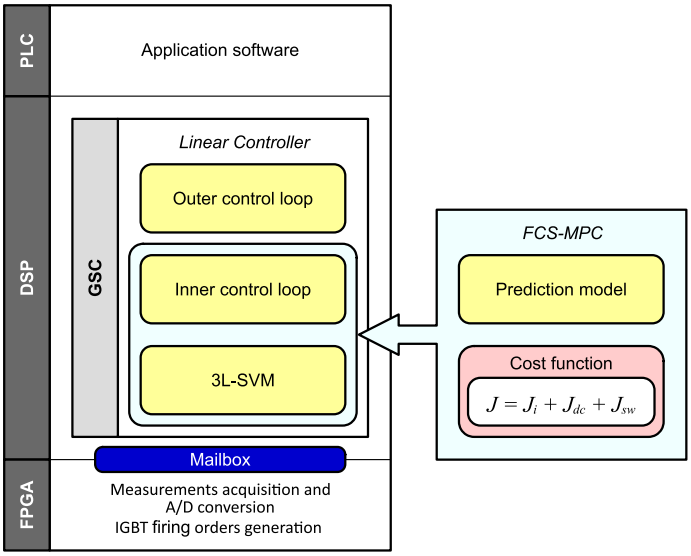

Fig. 4.4 Ingeteam CCU firmware architecture.

4.1.1 Description of Ingeteam control architecture

The control electronics for this converter are based on a distributed control topology comprising one CCU and four Power Management Modules (PMM). Distributed configuration enables redundancy under faulty conditions and availability of the turbine is thus maximized. The single CCU operates the two paralleled conversion lines presented in Fig. 4.1. The CCU accommodates two independent grid-side controllers, and unique machine-side controller, which regulates the dual-stator winding multiphase machine [109]. Further, the CCU encompasses not only the essential controlling elements but also other functionalities such as protections and operation logics, which are comprehensively embedded within firmware. Each of the grid-side controllers comprises reactive current provision functions, outer control loops such as PLL and DC-link voltage controller, and incorporates the proposed FCS-MPC strategy for precise current control.

The PMMs are located within power conversion line cabinets. PMMs mainly digitize electrical measurements and send them upwards to the CCU, and generate trigger signals for IGBT gate drivers based on the orders received from the CCU.

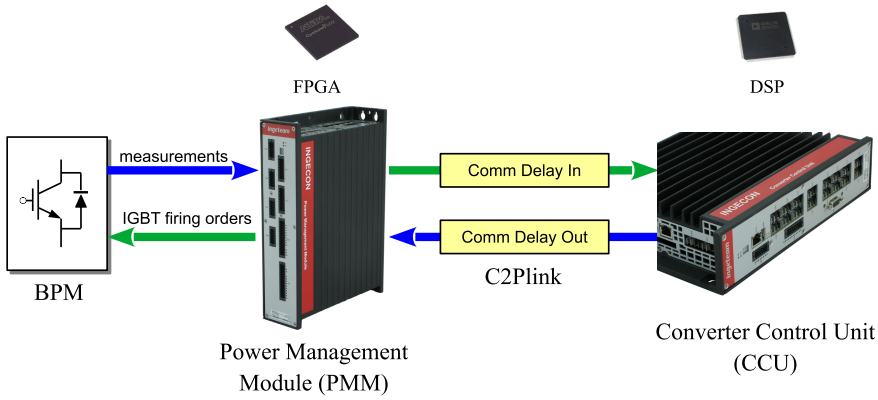

Fig. 4.5 Ingeteam control architecture.

One of the major tasks in this Industrial PhD Project is to embed the proposed FCS-MPC framework in the existing control architecture. Both the CCU and software structure are designed for traditional PWM-based control strategies and the consistent incorporation of MPC approach is not straightforward.

To meet real-time requirements, the different control functionalities within DSP are distributed into a task-based structure with different priorities and their corresponding periods. This task-based structure is equally applied within DLL

employed for SiL validation, and pertinent sampling time is then rigorously emulated. Table 4.1 describes the different control tasks that constitute the DSP application, along with the associated period and covered functionalities. In order to enhance FCS-MPC algorithm performance, grid-side controller is placed at the highest priority task with minimum possible period.

Table 4.1: *DSP control tasks.*

Task	Period	Main Functions
Task 0	136μs	- Grid-side controller - Fast protection supervision
Task 1	1.088ms	- Machine-side controller
Task 2	6.12ms	- Background calculations

4.1.2 Description of software-in-the-loop (SiL) platform

The DLL-EMT model is a good approach to maintain protection of intellectual property and reproducibility of results in different simulation environments. The DLL incorporates the Extended Simulation Environment (ESE)-interface, which meets compatibility requirements for different simulation environments. Its data structures and functions are described in the IEC61400-27-2 standard. The control DLL includes the original control algorithms which represent the behavior of the CCU firmware used in the real power converter. The DLL is built up replicating the same three layers structure of real firmware. Table 4.2 describes the layer representation of control DLL and includes the main functionalities performed by each layer and the corresponding time step. The existing differences between real system and simulation environment force FPGA (DLL layer 1) and PLC (DLL layer 3) to be emulated. The original source code of these two layers is adapted to be compiled into the control DLL, which precisely represents the real system performance. On the other hand, the actual source code (C-code) processed by the CCU DSP in real application is directly compiled into control DLL. Therefore, the DLL layer 2 is constructed without any code modification and the complete control strategy can be fully developed and tested by means of the DLL-EMT simulation models.

Table 4.2: *Layer representation of control DLL.*

DLL layer	Description	Time Step	Main Functions
DLL layer 1	FPGA emulation	Simulation time step (1µs - 10µs)	- Primary signal acquisition - Ultra-fast protections - IGBT firing orders generation (PWM)
DLL layer 2	DSP actual source code (C-code)	(>100µs)	- Fast protections - Control strategy
DLL layer 3	PLC emulation	(≈5ms)	- Peripheral communications - Operation logics - Slow supervisory algorithms

4.1.3 Proposed delay compensation method

The physical constraints of practical setting cause time delay between sampling measurements and applying updated control action. The encountered sources of delays can be summarized as follows:

- $\mathbf{T_{Delay\_IN}}$**:** delay between the sample and the instant when the control algorithm is computed in the control unit. *Measurement delay* (sampling and filtering) and *Uplink communication delay* (serial link).
- $\mathbf{T_{s\_DSP}}$ **(~100µs):** *computation delay* of control-algorithm, which processes the predictive controller, outer control loops, and monitoring tasks.
- $\mathbf{T_{Delay\_OUT}}$**:** *Downlink communication delay* referring to the time required to send the newly computed switch position back before its application.

The presence of delays in a discrete-time control system implies that when the new switching state is applied, the plant has evolved in time and no longer aligns with the sampled values. The delayed application of switching actions increases the current ripple and degrades the closed-loop performance of the controller. Then, the predictive controller is augmented with an initial estimation stage to compensate delays [110]. The operation of predictive control with compensated delays is shown in Fig. 4.6. The control algorithm estimates the value of measurements at application instant SW_k considering the previously applied switching vectors. The estimation process is divided into different steps, considering the total delay length and the control task period T_s, as the applied switching state could vary for each control task

interval. Once measurements are properly estimated at acting instant SW_k, predictions for all switching states are established, and cost function is evaluated. The optimal switching state that minimizes cost function is then selected and stored to be applied at next acting instant.

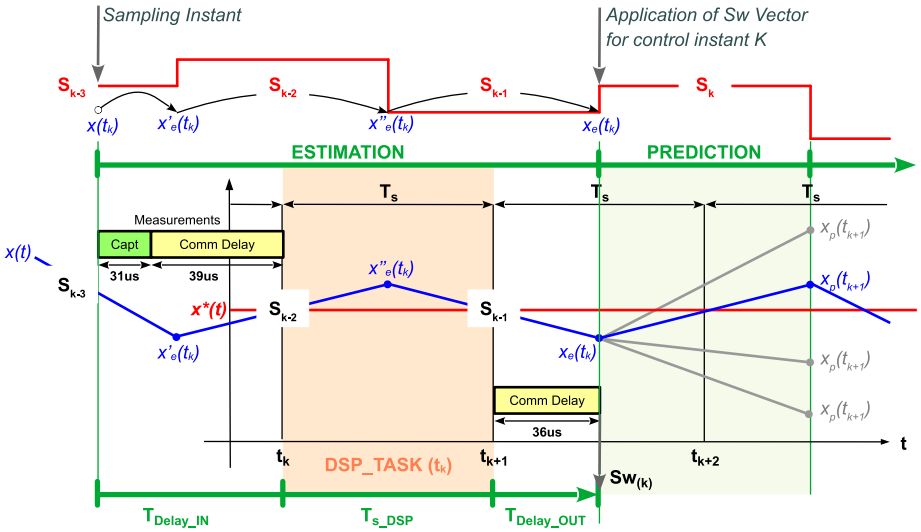

Fig. 4.6 Ingeteam CCU delay. Source [C4].

4.1.4 FCS-MPC algorithm optimization

The computational complexity and the high sampling frequency requirement present the big challenge for real-time implementation of FCS-MPC algorithm, where exhaustive search is common practice for solving MPC optimization problem. For the 3L-NPC power converter, there are a total of 27 possible output switching states. However, FCS-MPC algorithm can be simplified if the number of candidate vectors is reduced. The proposed optimization approach determines the optimal sequence for evaluating vectors by considering both voltage proximity and minimizing the number of switching transitions. This criterion dictates that adjacent vectors are more likely to be employed during continuous sampling intervals. Furthermore, the controller is constrained to allow only one switching transition each sampling time, limiting the number of vectors to be evaluated. This reduction in vector evaluations leads to a minimized computation load dedicated to MPC algorithm.

The proposed optimization approach can be summarized as follows. First, a table is constructed with an offline defined optimal vector sequence. This sequence establishes the order where vectors are evaluated according to a proximity criterion.

Second, the vector applied in the previous sampling interval establishes the sequence of vectors to be employed and the number of vectors to be evaluated. Finally, the optimization problem is solved with a reduced set of candidate vectors and the computation efficiency of MPC algorithm is then enhanced.

4.1.5 Adaptation of FCS-MPC algorithm to ANPC topology

In the 3L-ANPC configuration, the clamping diodes are replaced by active switches (S_{a5} and S_{a6}), which allows determining the current path by four different switching states when output voltage is set at 1-level, as shown in Table 4.3. These redundant switching states enable an improved control of loss sharing among power devices, and the output power capability of the power converter is thus increased [111]. The 3L-ANPC configuration is employed to further extend the power rating up to 15MW of the *INGECON® WIND FULL CONVERTER MV* solution. This PhD Project was initially focused on 3L-NPC topology. However, during its progress, the industrial landscape shifted toward the 3L-ANPC topology as preferred solution. The transition to 3L-ANPC required new software and HiL platform configurations. To streamline compatibility, it is determined that harmonizing the developed FCS-MPC strategy with the ANPC system represented the most straightforward approach. As a result, the predictive control strategy was integrated into the 3L-ANPC software release, ensuring a cohesive and effective approach to experimentation and research within this updated framework.

Table 4.3: *3L-ANPC switching states.*

Switching Vector	**Switching Orders**					
S_x	S_{a1}	S_{a2}	S_{a3}	S_{a4}	S_{a5}	S_{a6}
[2]	1	1	0	0	0	1
$[1]_{U2}$	0	1	0	0	1	0
$[1]_{U1}$	0	1	0	1	1	0
$[1]_{L1}$	1	0	1	0	0	1
$[1]_{L2}$	0	0	1	0	0	1
[0]	0	0	1	1	1	0

The essential framework of the predictive control structure is integrated into the 3L-ANPC solution firmware with the addition of a software adaptation layer. This adaptation layer accommodates the switching vector provided by controller to the IGBTs switching orders required by 3L-ANPC solution, where the use of redundant

switching states prompts the equal loss distribution among power devices. With this architecture, the FCS-MPC algorithm considers only the switching states inherent to 3L-NPC configuration, while mentioned adaptation layer performs the conversion to 3L-ANPC. Therefore, the developed FCS-MPC algorithm can be straightforwardly employed for the 3L-ANPC solution.

In chapter 2.2.4, the switching frequency control method employed by FCS-MPC is described. In the case of the 3L-ANPC configuration, the usage of redundant switching states results in an average value f_{sw} that is half of what is targeted by controller.

4.2 Software-in-the-loop (SiL) validation

In this section, time-domain simulation is performed in *Matlab/Simulink* to validate the proposed MPC-based control strategy under different scenarios. Fig. 4.7 shows the DLL-EMT model of the power system, which is built with components from *SimPower Systems* library and control solution is run by DLL. The discrete solver with fixed-step size of 8.5µs is selected to accomplish the accurate simulation results. The detailed parameters of the system are given in Table 4.4.

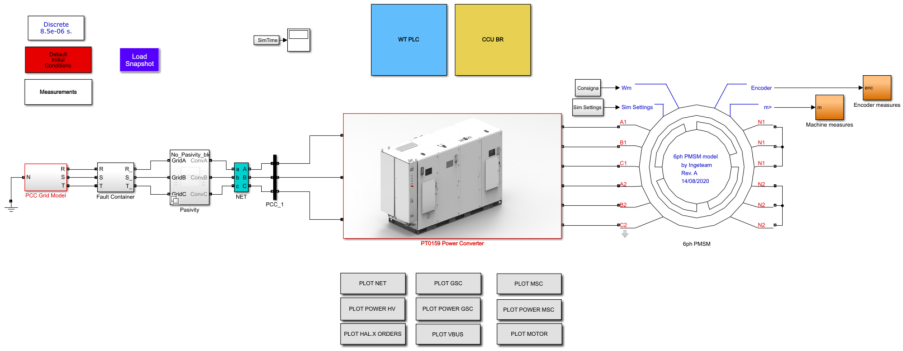

Fig. 4.7 Matlab/Simulink model of power converter solution with two ANPC conversion lines.

Table 4.4: *System parameters.*

Parameter	Value
Rated Power P_N	14 MW
Secondary Rated Voltage V_g	3100 V
Primary Rated Voltage V	66000 V
DC-link voltage V_{dc}	5600 V
Average switching frequency f_{sw}	1 kHz
Filter Inductance L_f	400 µH
Filter Resistor R_f	1.3 mΩ
MPC Sampling Time T_s	136 µs

4.2.1 Steady-state operation analysis

The steady state performance of power converter solution is presented in Fig. 4.8. The active power reference in machine-side converter control is set to 14MW. The dual-secondary winding step-up transformer uses *Yyd* connection, which causes a 30-degree phase-shift in voltage waveforms between the conversion lines. This configuration reduces low-order harmonic content in the primary winding and helps to optimize filter design. Each of the conversion lines *Conv. line No. 1* and *Conv. line No. 2* injects into grid half of generated active power to control the DC-link voltage, and reactive power to compensate the reactive power drawn by step-up power transformer, as shown in Fig. 4.8(a). Fig. 4.8(b) shows the behavior of switching frequency control, where weights λ_{sw} are adapted to maintain switching frequency of all power devices at desired reference value. The average switching frequency f_{sw}, which is derived from activation orders for power devices, is controlled around 500Hz. The voltage and current waveforms, and DC-link capacitor voltage are shown in Fig. 4.8(a), which verifies the neutral-point balancing control strategy. Fig. 4.8(d) validates current reference tracking accuracy of MPC algorithm in both $\alpha\beta$-axis and dq-axis, which further ensures the proper response to outer control loops demands.

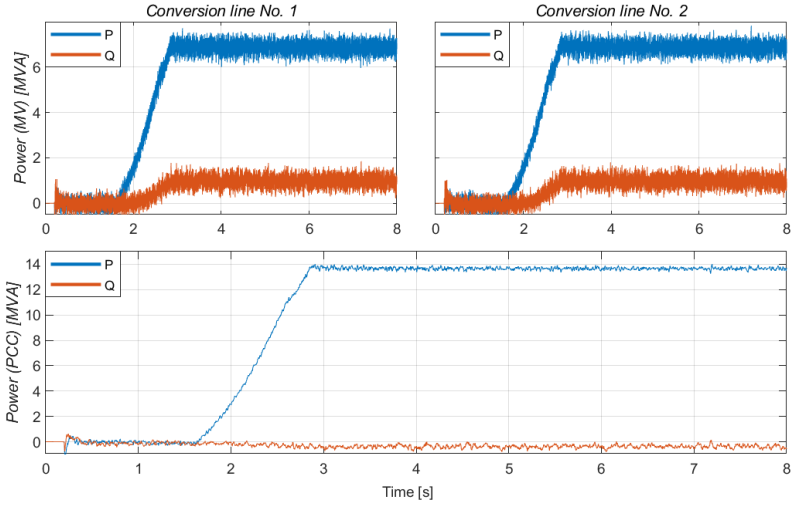

(a) Generated power.

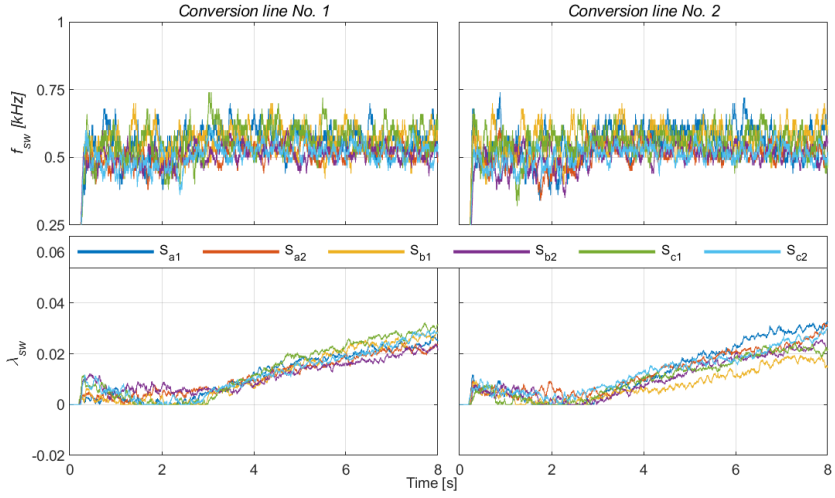

(b) Switching frequency control.

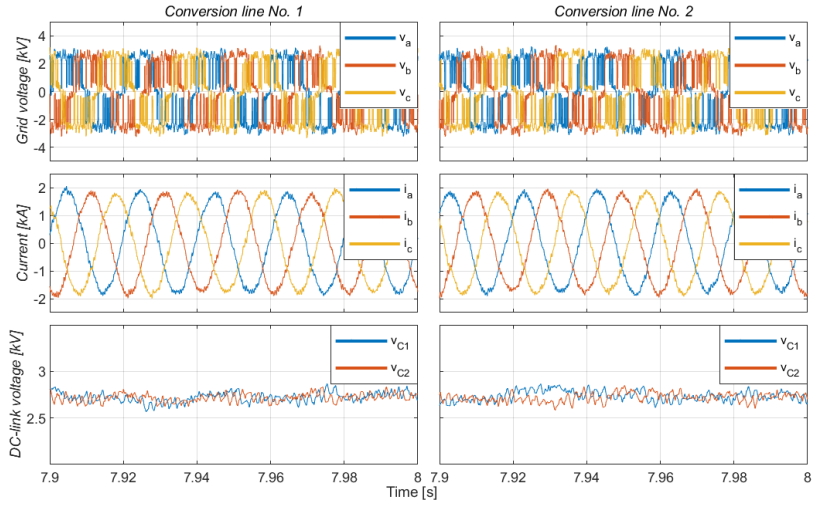

(c) Voltage, current, and DC-link voltage waveforms.

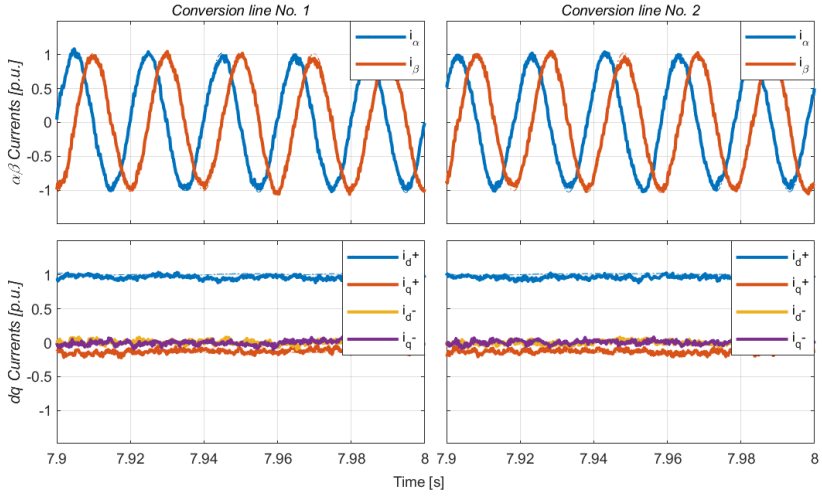

(d) Current reference tracking.

Fig. 4.8 Steady-state operation at 14MW of two paralleled conversion lines.

1) Harmonic emission requirements

The level of harmonic distortion generated by the wind turbine must be assessed to comply with the harmonic limits imposed by grid codes. The harmonic emission analysis requires detailed modeling of all components in the power system under study to obtain the accurate measurement of harmonic current and voltage levels at the PCC. The most extended standards are the IEEE 519 [36] and the IEC 61000-3-6 [112], which define the compatibility levels for individual harmonic currents and

voltages respectively. Fig. 4.9 shows the waveform and harmonic spectrum of grid current and voltage measured at PCC for the two paralleled conversion lines operation. The operating conditions is that both conversion lines are operated at rated active power for a grid impedance of SCR = 10. Further, the harmonic limits imposed by the standards are also presented. Results show that harmonic current emissions almost comply with the IEEE 519 requirements. Fig. 4.10 shows the waveform and harmonic spectrum of power converter output current for each conversion line. Current harmonic content is detailed in Table 4.5.

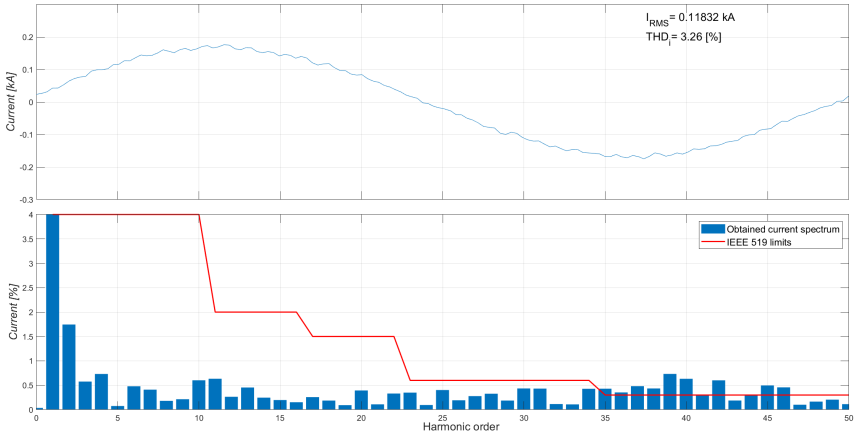

(a) Current spectrum.

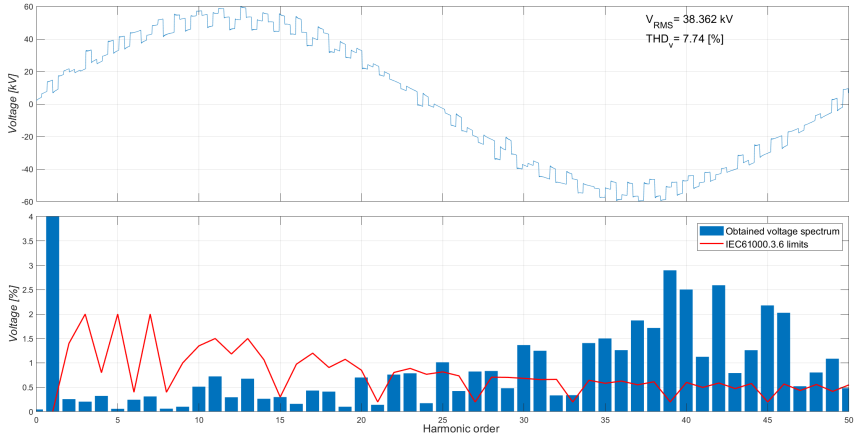

(b) Voltage spectrum.

Fig. 4.9 Spectrum of grid current and voltage at PCC for the FCS-MPC controlled two paralleled conversion lines.

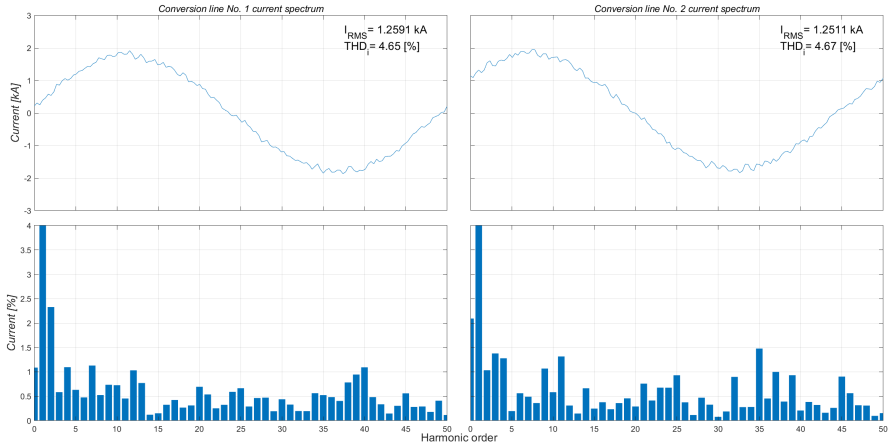

Fig. 4.10 Current spectrum of each conversion line measured at MV-side.

Table 4.5: *Current harmonic content summary.*

	CL No. 1	**CL No. 2**	**PCC**
I_{RMS} [kA]	1.259	1.251	0.118
THD_i [%]	4.65	4.67	3.26

2) Thermal analysis of power device

Thermal analysis of power devices is a critical aspect in the design of power converters. The accurate estimation of junction temperatures in power devices holds immense significance to ensure the system reliability under diverse operating conditions. For that purpose, the specialized simulation tools developed by Ingeteam are used for estimating thermal characteristics of power electronic modules. The first tool *TL0007 – POWER LOSSES ESTIMATOR* calculates power losses within power modules based in semiconductor specifications and voltage and current measurements. The second tool *TL0009 – TEMPERATURE ESTIMATOR* obtains the temperature profiles by utilizing the thermal network of power devices and the power loss data generated by *TL0007*. Fig. 4.11 presents the operating scheme for the thermal evaluation. The datasheet parameters of power module and device measurements are employed to obtain the junction temperatures for certain operating conditions evaluated in simulation. This thermal validation approach detects overheating risks and potential device failures.

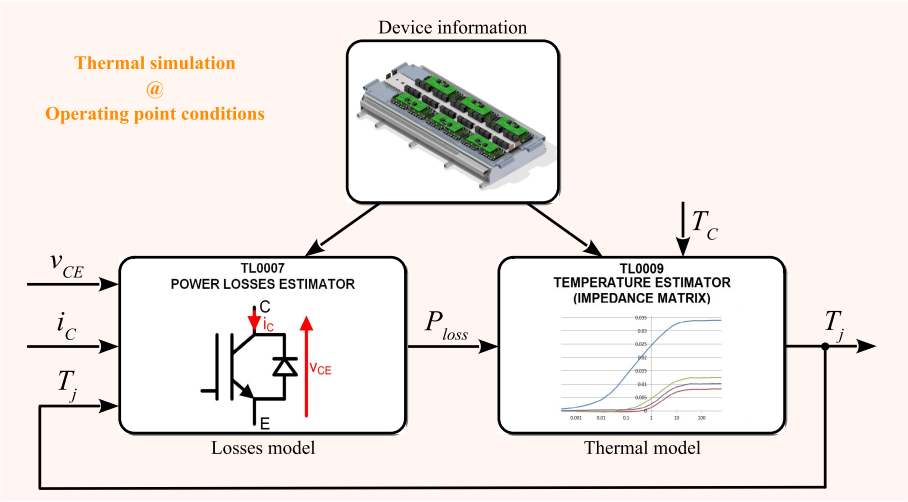

Fig. 4.11 Thermal evaluation tools operating scheme.

The power converter is operated at rated active power to conduct the loss and thermal evaluation. The specialized simulation tools are configured for BPM of *INGECON®WIND 7.5 MW FC MV power converter*. The simulation time step is reduced to 1.0625μs in order to improve accuracy of thermal evaluation. Fig. 4.12 shows the loss and thermal analysis of power converter at rated conditions. The grid-side power stack produces 6.9MW and 980kVAR, which are required to deliver the generated active power to the grid and compensate the reactive power consumption of step-up transformer. Under these operating conditions, the output current is 1260A.

The loss distribution of all switching devices within one phase is shown in Fig. 4.12(a). It can be seen that switching loss is dominant compared to conduction loss in all devices. Inner switches T_2, T_3 have higher losses and clamping switches T_5, T_6 have the lowest losses. Thermal cycling of each switching device is shown in Fig. 4.12(b). The cycling frequency is 50Hz. The most stressed devices are the inner switches, while the mean junction temperature in clamping switches is the lowest. The difference in junction temperature of IGBT and freewheeling diode is more noticeable for outer switches. Table 4.6 summarizes the power loss P_{sw} and P_{con}, the junction temperature mean value T_{jmean} and maximum value T_{jMAX} for each of the power devices.

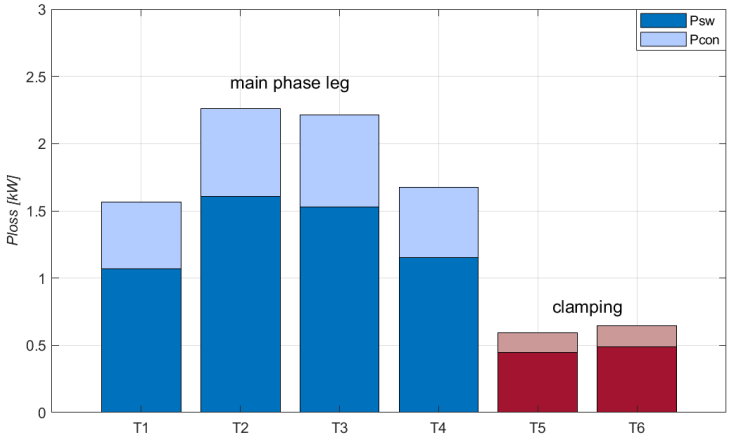

(a) Loss distribution.

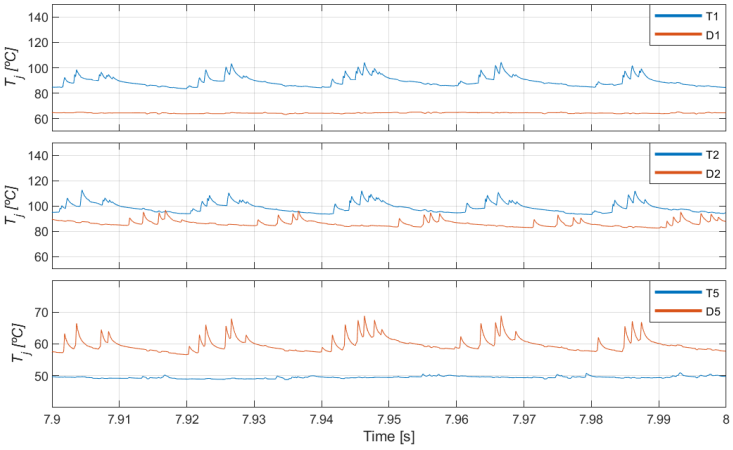

(b) Junction temperature distribution.

Fig. 4.12 Loss and thermal analysis of BPM at rated conditions.

Table 4.6: *Thermal results summary.*

	P_{sw} [W]	P_{con} [W]	T_{jmean} [ºC]		T_{jMAX} [ºC]	
			IGBT	FWD	IGBT	FWD
T_1	1216	512.3	89.2	64.4	104.3	65.3
T_2	1657.2	682.6	98.6	86.1	112.6	96.6
T_5	484.2	154.3	49.5	59.8	50.9	68.9

4.2.2 Fault ride-through operation

The power converter operates steadily at rated active power, and a 200ms grid fault is triggered at the PCC at t = 3.5s. The simulation tests include three-phase and two-phase 0% voltage faults. The active power generated on the machine-side remains constant. The braking chopper limits voltage boost caused by power imbalance between generated power and power injected into the grid. The maximum allowed current overload is $I_{max} = 1630\ A$. The requirements for reactive current injection are specified using voltage-time profiles with a gain $k^+ = 2$ for positive-sequence and $k^- = 1$ for negative-sequence, prioritizing reactive current injection in the positive-sequence.

Fig. 4.13 presents the simulation results during a 3-phase 0% LVRT event. As shown in Fig. 4.13(a), symmetrical current is supplied as the fault is balanced. Due to the significant reduction in active power output during the fault event, the braking chopper circuit is activated to maintain the DC-link capacitor voltage within operational thresholds. Fig. 4.13(b) shows the adaption of λ_{sw} to regulate the switching frequency, reaching a maximum value of $f_{swMAX} = 0.86\ kHz$ during the fault. PCC phase voltages and currents with sequence components are displayed in Fig. 4.13(d). The magnitude of the measured grid voltage in the positive-sequence is $|v^+| = 0.1\ pu$, which establishes the reference for reactive current provision to its rated value as $k^+ = 2$. The results indicate that capacitive current in the positive-sequence $i_Q^+ = 0.96\ pu$ is injected into the grid, while current in the negative-sequence is zero.

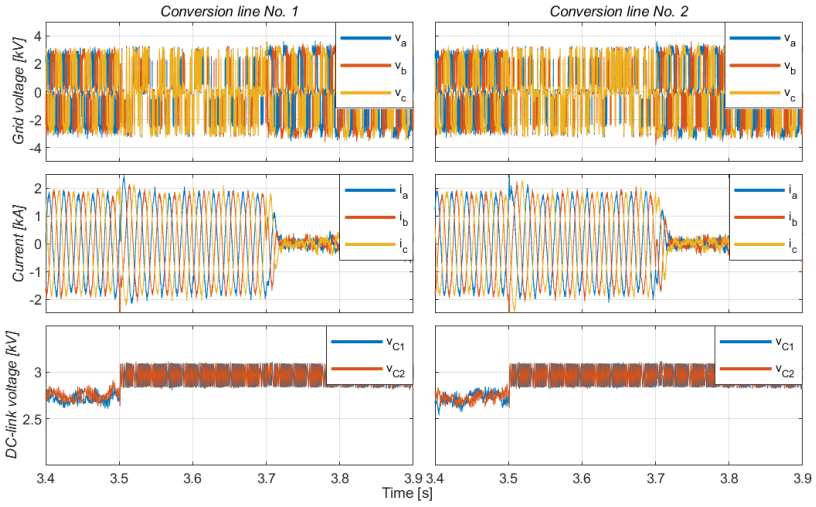

(a) Voltage, current, and DC-link voltage waveforms.

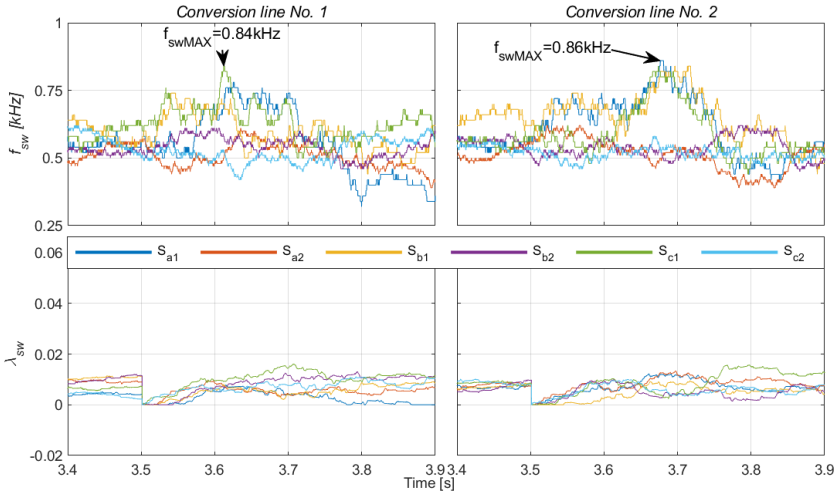

(b) Switching frequency control.

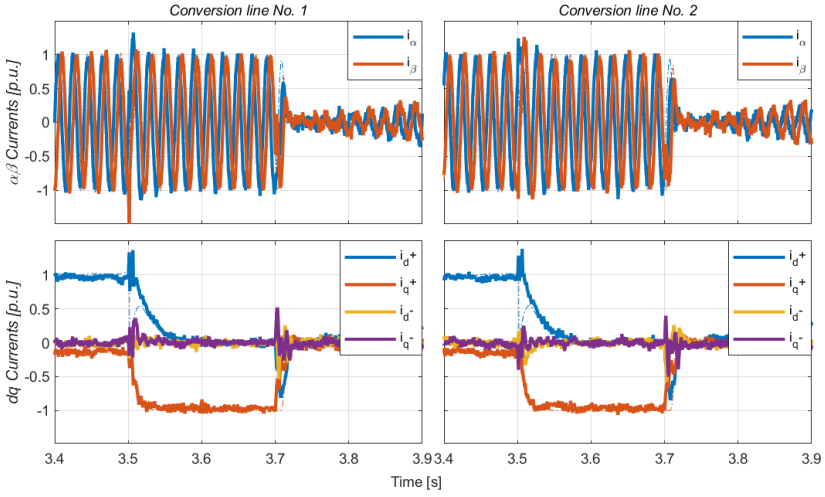

(c) Current reference tracking.

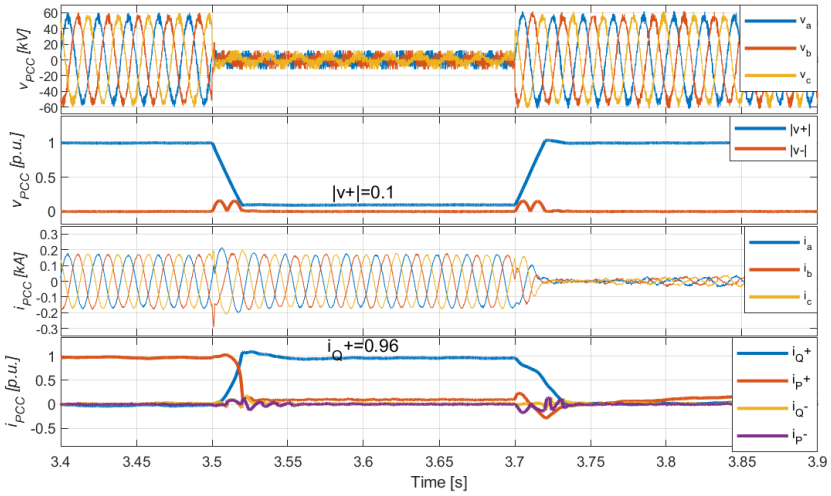

(d) PCC phase voltages and currents with sequence components.

Fig. 4.13 The simulation results of 3L-ANPC converter under 3-phase 0% LVRT.

Fig. 4.14 presents the simulation results during a 2-phase 0% LVRT event. As shown in Fig. 4.14(a), asymmetrical current is supplied as the fault is unbalanced. During the fault, power converter current limit is reached due to reactive current injection, setting the active current to zero and activating the braking chopper circuit. Fig. 4.14(b) shows the distinct values of λ_{sw} needed for each IGBT. In Fig. 4.14(c), it is revealed that the dq-frame currents in both conversion lines are comparable in the positive-sequence, but differ in the negative-sequence. This discrepancy is attributed to the phase-shift between secondary windings, which alters the angle of negative-sequence voltage and thus impacts the dq-axis components in the current control reference framework. The measured sequence components for grid voltage are $|v^+| = 0.59\ pu$ and $|v^-| = 0.47\ pu$ as displayed in Fig. 4.14(d). As the fault is unbalanced, inductive current in the negative-sequence $i_Q^- = -0.25\ pu$, and capacitive current in the positive-sequence $i_Q^+ = 0.95\ pu$ are injected into the grid to support FRT.

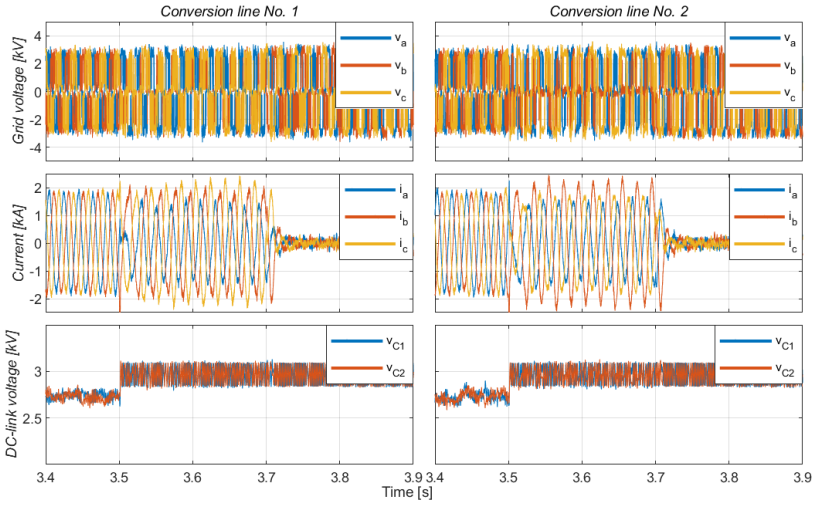

(a) Voltage, current, and DC-link voltage waveforms.

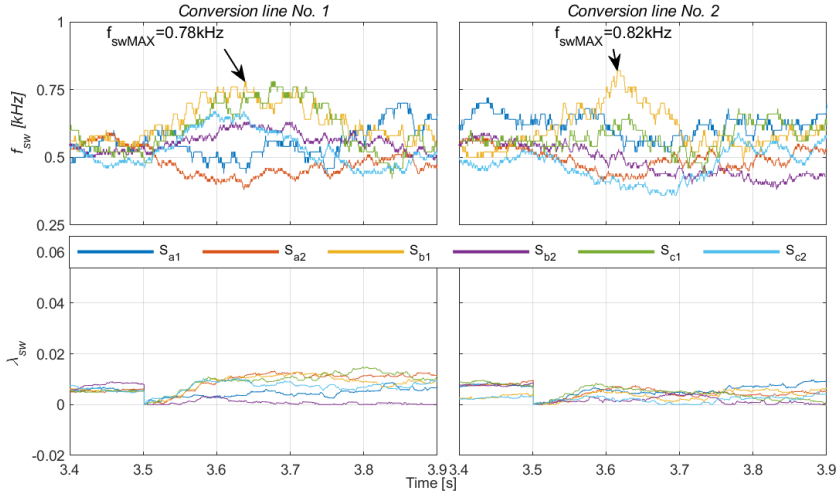

(b) Switching frequency control.

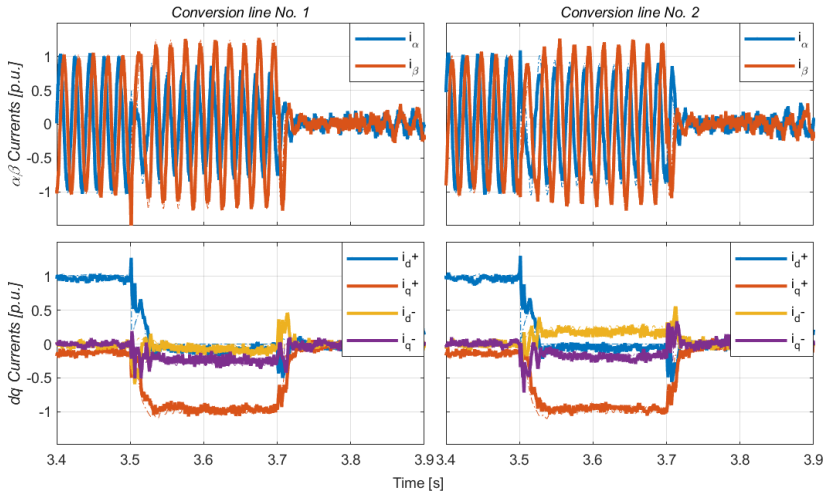

(c) Current reference tracking.

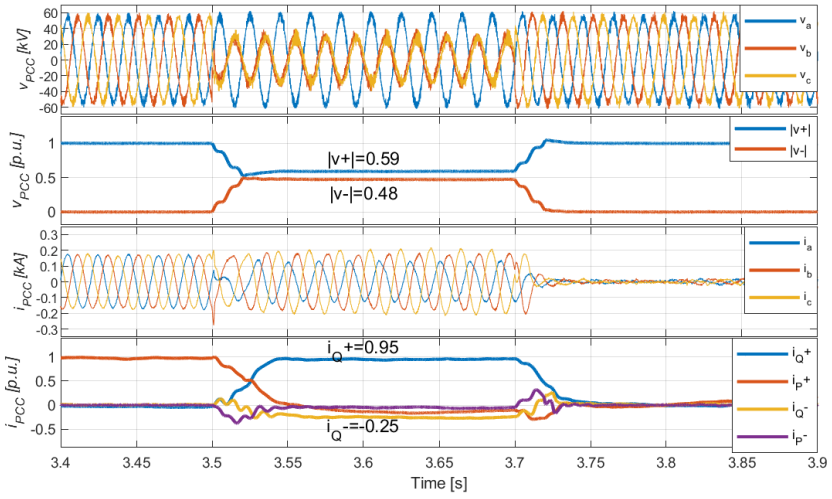

(d) PCC phase voltages and currents with sequence components.

Fig. 4.14 The simulation results of 3L-ANPC converter under 2-phase 0% LVRT.

4.2.3 Operating performance under weak grid

The instability issue of power system is greatly challenged in weak grids. A weak grid is defined as a power grid with low SCR, which can cause voltage fluctuations and grid-connected inverter instability. Hence, operational capability under weak grid condition is a major concern to guarantee the stable operation of the wind turbine.

The operating performance of power converter solution under weak grid condition is presented in Fig. 4.15. The power converter operates at rated power and grid SCR is 10. At instant t = 4.0s, grid impedance is drastically increased, and SCR reaches a value of 1.3. The power converter maintains continuous operation under weak grid condition. After the transient event, active power generation level is sustained and reactive power injection level is increased to support voltage drop caused by new grid condition, as it can be seen in Fig. 4.15(a). Fig. 4.15(b) shows the voltage and current waveforms, and DC-link capacitor voltage, which confirms the good performance of current and neutral-point balancing control. The voltage and currents at PCC are shown in Fig. 4.15(c). Because of current flow through increased grid impedance, voltage level at PCC is reduced from rated value to $|v^+| = 0.87\ pu$. Active current level is then raised to $|i_P^+| = 1.11\ pu$ in order to sustain active power generation level. In Fig. 4.15(d), PCC phase voltages and currents waveforms are displayed. As grid impedance is increased, current THD is reduced from 3.72% to 1.26%. However, grid voltage waveform is more distorted as impact of switching component from power converter is higher.

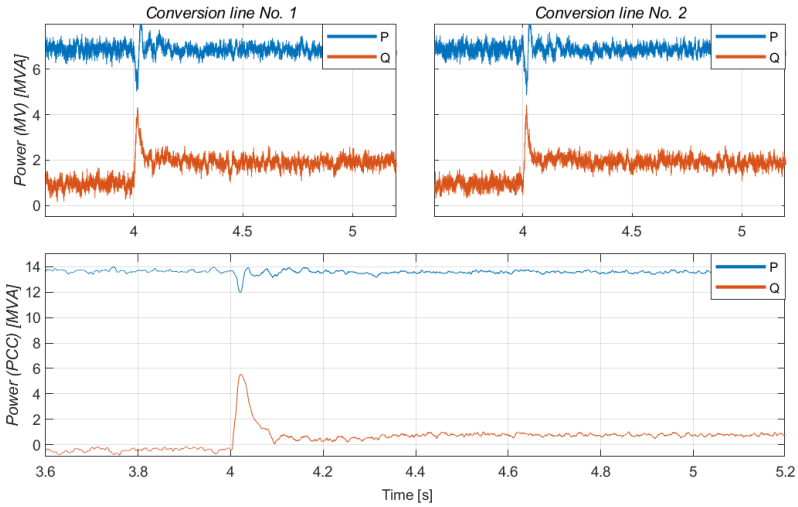

(a) Generated power.

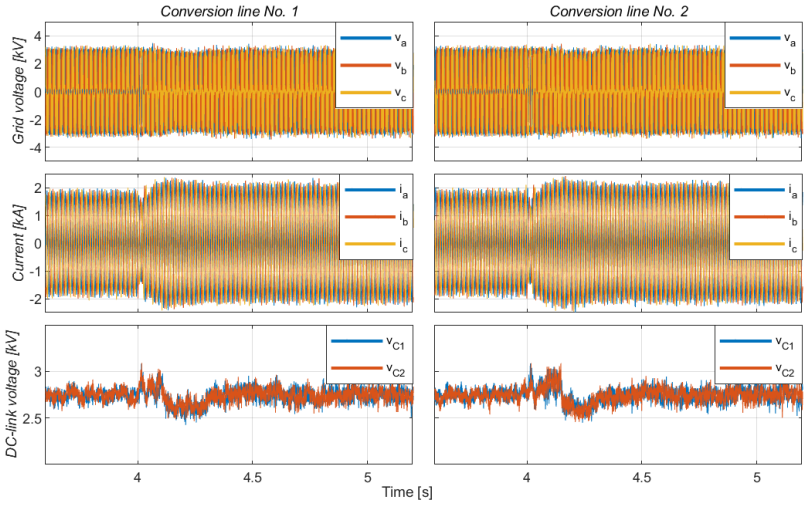

(b) Voltage, current, and DC-link voltage waveforms.

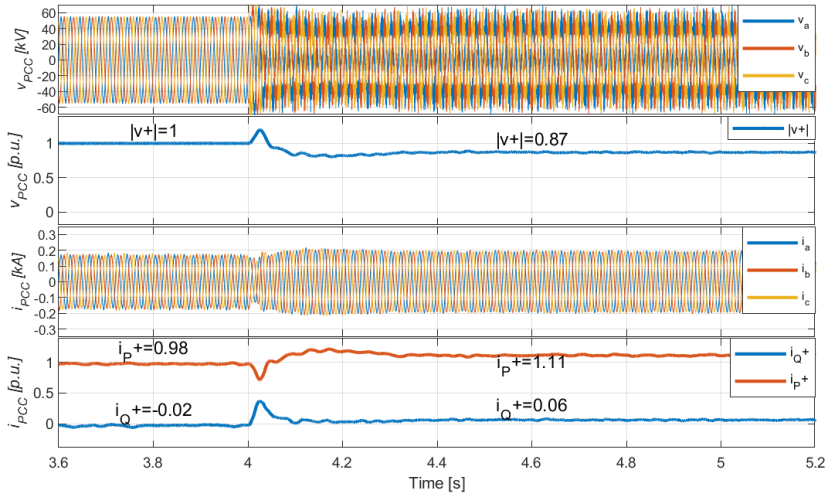

(c) PCC phase voltages and currents with sequence components.

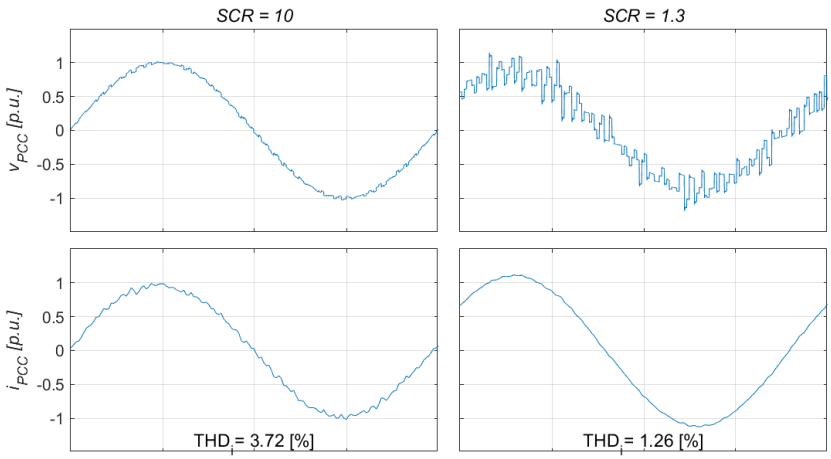

(d) PCC phase voltages and currents waveforms.

Fig. 4.15 Weak grid operation.

4.3 Hardware-in-the-loop (HiL) validation

Real-time simulation is the most efficient and effective tool to meet design and validation requirements for power electronic applications and their integration in power systems. The Ingeteam HiL platform [Fig. 4.16(a)] is composed of the *OP5700* Real-time simulator combined with the *OP5607 Virtex7 FPGA & I/O Expansion Unit.* This platform can address strict time constraints in model computing of power electronics, and perform accurate real-time simulations of the power converter solution. Further, the real-time simulator is interfaced with the actual CCU [Fig. 4.16 (b)]. The CCU incorporates the Web Application [Fig. 4.16(c)], which is a user-friendly software tool used to manage power converter operating condition. The WebbApp operator panel supports different services such as monitoring, configuration, diagnostics, control, data recording, and commissioning either locally or remotely when necessary. The data recording module allows specific data to be captured when a pre-defined trigger condition is met. The recorded data is then stored in CCU internal memory, making it accessible for analyzing the power converter behavior. Therefore, HiL validation assesses the real-time performance of the power converter and the complete coverage in firmware testing. The employed parameterization is obtained from Table 4.4.

(a) Hardware-in-the-Loop (HiL) platform.

(b) Ingeteam Converter Control Unit (CCU).

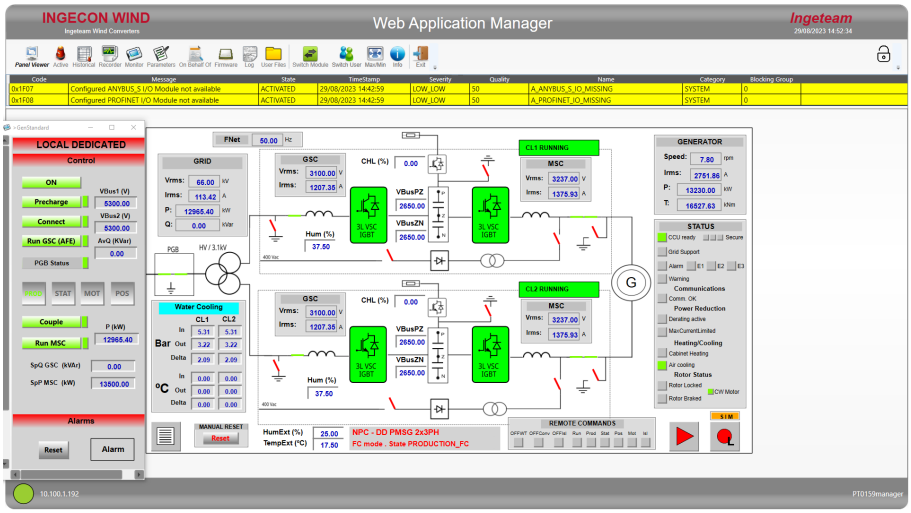

(c) Ingeteam WebApp operator panel.

Fig. 4.16 Experimental setup.

1) Steady state operation

Fig. 4.17 shows the HiL results for the steady state operation of power converter at rated active power P_N. The voltage waveforms between both conversion lines are phase-shifted by 30 degrees due to the transformer configuration, and the switching component can also be observed in Fig. 4.17(a). The implemented MPC algorithm shows good current reference tracking performance, and neutral-point voltage remains balanced. Each of the conversion lines *Conv. line No. 1* and *Conv. line No. 2* provides half of rated active power *P* and reactive power *Q* to compensate the reactive power drawn by step-up power transformer. Fig. 4.17(b) shows the harmonic spectrum of grid current measured at PCC for the two-paralleled conversion line operation. The operating conditions employed is that both conversion lines are operated at rated active power for a grid impedance of SCR = 10. Further, the harmonic limits imposed by the standards are also presented. Results show that harmonic current emissions almost comply with the IEEE 519 requirements.

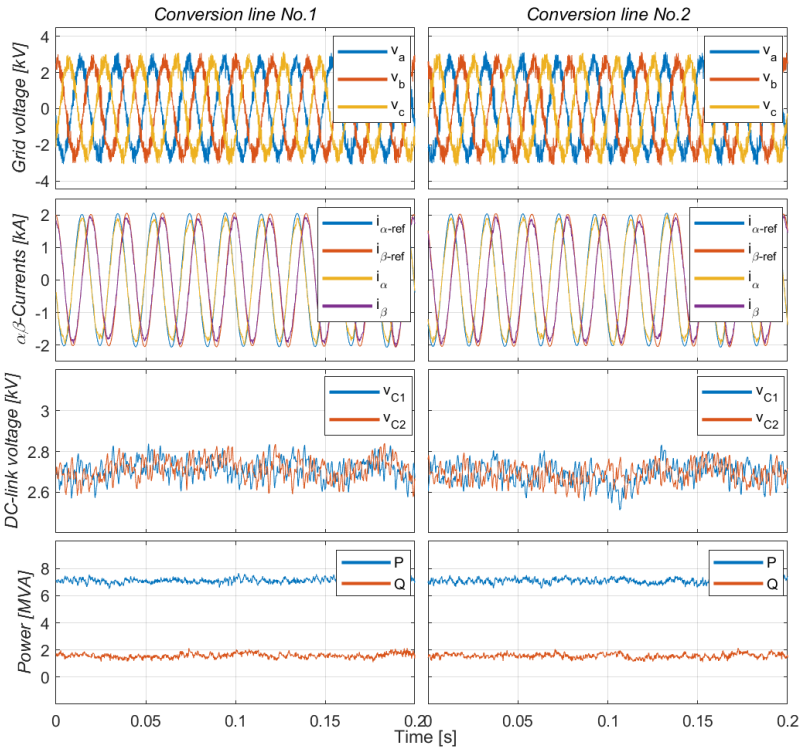

(a) CCU measurements.

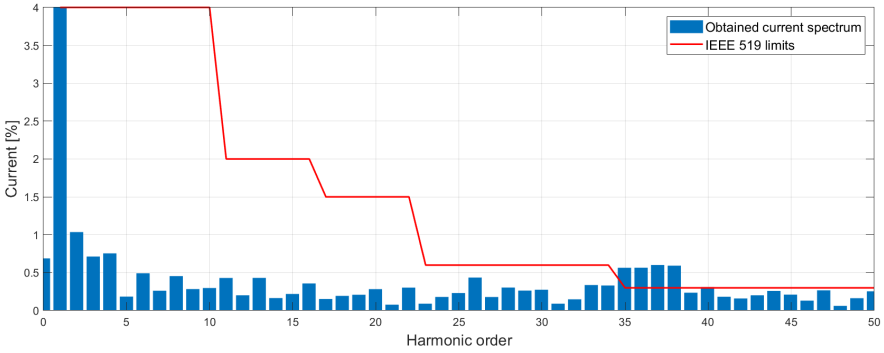

(b) Current harmonic emission of the WECS at PCC.

Fig. 4.17 Experimental results during steady state operation at rated power of 14MW. Source [C4].

2) Fault ride-through operation

Fig. 4.18 presents the HiL results during LVRT operation. The power converter operates steadily at rated active power, and a 200ms grid fault is triggered at the PCC at t = 2.0s. The 3-phase 0% LVRT testcase and 2-phase 0% LVRT testcase are displayed in Fig. 4.18(a) and Fig. 4.18(b), respectively. During both grid fault events, capacitive power is injected, while the active power output is significantly reduced. Consequently, the hysteresis control of the braking chopper is activated to limit the voltage boost in the DC-link and maintain capacitor voltage within operational thresholds. The current reference tracking is sustained for transient grid fault operation and the fast dynamic response is exhibited.

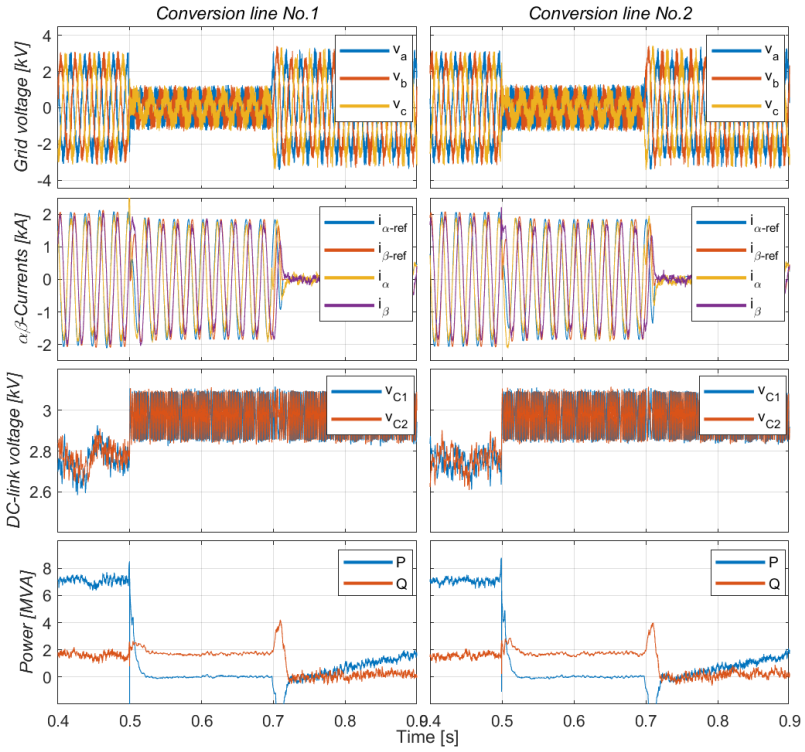

(a) 3-phase 0% LVRT.

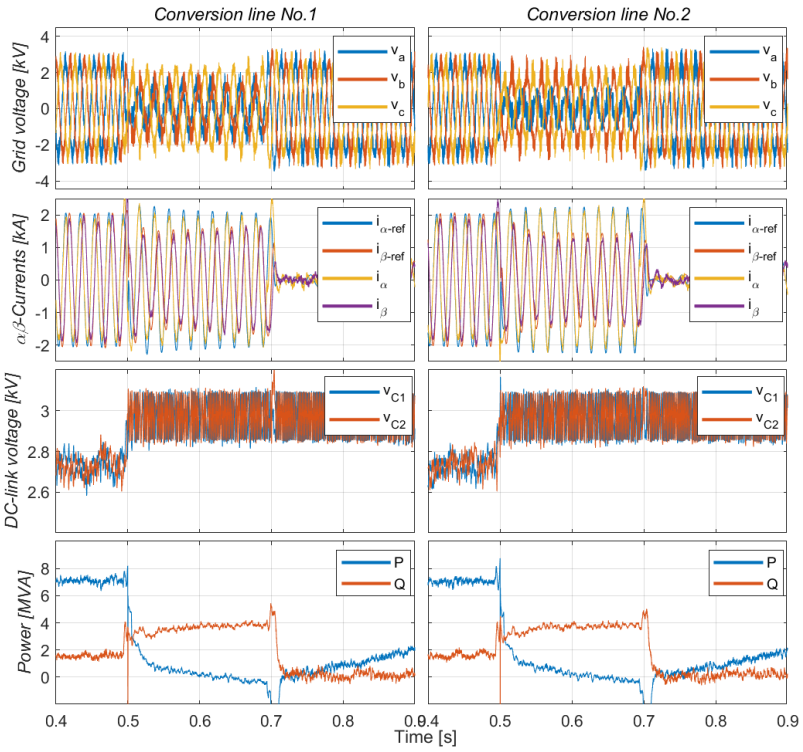

(b) 2-phase 0% LVRT.

Fig. 4.18 Experimental results during fault ride-through operation. Source [C4].

3) Weak grid operation

Fig. 4.19 shows the HiL results for the power converter operating at rated active power P_N under weak grid condition of SCR = 2. Due to limitations in the experimental setup, the value selected for grid impedance cannot be changed dynamically during experiments. The simulation results display the absence of resonance phenomena in output voltage and current, and balanced state of DC-link capacitor voltage. The generated active power is effectively delivered to the power grid and the level of injected reactive power is increased to support voltage drop caused by high-impedance grid. Thus, the capability of FCS-MPC to stably operate the power converter under weak grid condition is exhibited.

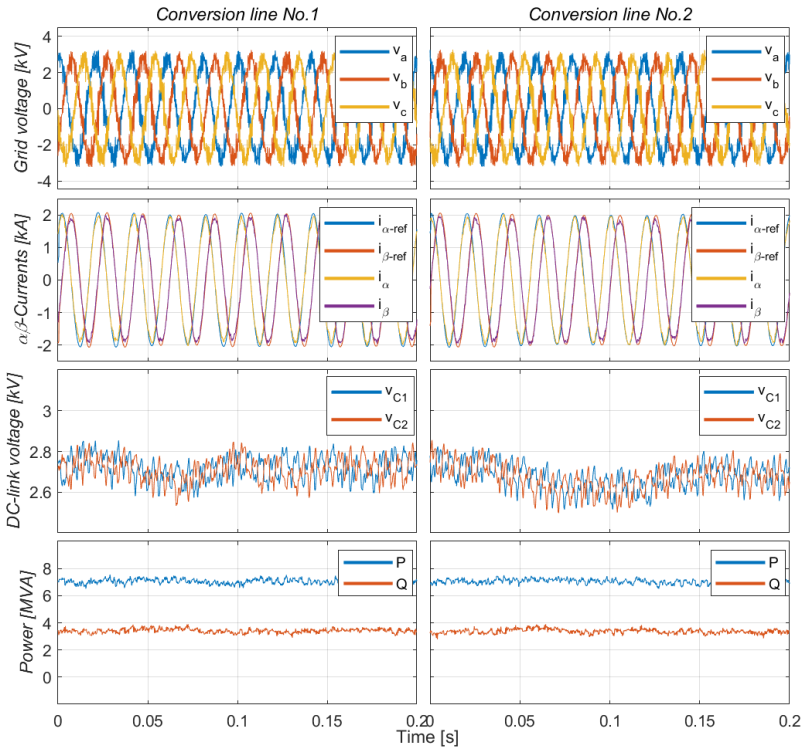

Fig. 4.19 Experimental results during weak grid operation.

4.4 Summary

In this chapter, the application of FCS-MPC in the grid-side controller is investigated and validated for the Ingeteam power converter solution comprising two-paralleled ANPC power conversion lines. The integration procedure of MPC-based control strategy into CCU is detailed, and associated implementation challenges in terms of computational burden and delay compensation are addressed. Further, a novel optimization method for MPC algorithm is developed to improve its computational efficiency. As an emerging and promising control solution, practical implementation of FCS-MPC necessitates comprehensive validation to advance its industrial adoption. Therefore, rigorous SiL and HiL testing have been implemented for system operational performance assessment, focusing on steady-state operation and fault ride-through operation. The proposed MPC successfully achieves precise

current regulation and demonstrates rapid dynamic response, exhibiting its potential applicability for high-power WECS.

5. CONCLUSION

This chapter summarizes the main conclusions in this Industrial PhD Project. Also, the future work is discussed. The aim of this Industrial PhD Project is to develop a novel MPC control strategy to enhance the operating performance of high-power wind power converter. The advantages of FCS-MPC compared to traditional controllers have been investigated, and the incorporation of an efficient FCS-MPC strategy into the CCU of the Ingeteam power converter solution is validated.

5.1 Main contributions

The main contributions of this Industrial PhD Project are summarized as follows.

(1) **An advanced FCS-MPC strategy for high-power 3L-NPC and 3L-ANPC converter is developed.** The proposed control strategy addresses the generation of current reference and establishes a multi-objective cost function for FCS-MPC, covering current regulation, neutral-point voltage balancing, and switching frequency control. A novel approach with online weight tuning is employed for regulating average switching frequency. The robustness of proposed method is validated against variations in operating point and grid conditions. This feature further enables real-time regulation of average switching frequency and resulting impact on power loss of power converter. The fault ride-through capability of the high-power 3L-NPC converter with MPC is successfully demonstrated, exhibiting effective current regulation and fast dynamic response, which satisfy the stringent requirements of most recent grid codes. Robustness of FCS-MPC against variations in grid filter parameters is also examined. The controller is then augmented with an EKF-based parameter observer to furnish immunity and stable performance regardless of parameter variations.

(2) **Stability of 3L-NPC inverter with FCS-MPC is investigated.** The impedance-based stability analysis method is proposed to investigate the stability mechanisms of grid-connected inverter with FCS-MPC. The Impedance Measurement Toolbox is developed to perform frequency-scan technique and obtain the impedance characteristics from EMT simulations, which overcomes the lack of mathematical model of MPC. Impedance characteristic of MPC is analyzed under different controller configuration and operating conditions. The benefits for stability enhancement of reducing sampling time in MPC are revealed as passive region of control system is

extended. The integration into offshore wind farm of wind turbines operated with proposed MPC control strategy is evaluated, and its capability for mitigating the instability phenomena is demonstrated.

(3) **Implementation of the proposed MPC in Ingeteam power converter solution.** The proposed FCS-MPC framework is embedded into existing software package by replacing concerned code segment. Inherent challenges of real-time implementation are effectively addressed, including delay compensation and computational burden optimization through efficient implementation of FCS-MPC algorithm. Moreover, proposed control strategy demonstrates compatibility with ANPC topology. Comprehensive SiL and HiL validation of the entire power converter solution with proposed FCS-MPC strategy is accomplished.

Therefore, this Industrial PhD Project enforces potential benefits of FCS-MPC for high-power wind power converter and contributes to its industrial application. The proposed MPC strategy can improve the long-term reliable operation of high-power wind power converter, facilitate the integration of offshore wind energy, and support power system stabilization. Furthermore, as an emerging control solution, the successful practical implementation and comprehensive validation of FCS-MPC in a real-world power converter solution represent a significant industrial advancement. This milestone showcases the feasibility and capabilities of the proposed control strategy.

5.2 Future Research Perspectives

Several potential research aspects have been identified as future work.

(1) The harmonic control of high-power grid-connected converters operated by FCS-MPC can be further addressed. Combination of FCS-MPC algorithm with selective-harmonic-elimination techniques and their application to paralleled conversion lines can be investigated.

(2) The capability of MPC strategy to regulate average switching frequency and directly conduct specific semiconductors can be further developed for thermal stress reduction to extend lifetime of wind power converter.

(3) The performance benefits and real-time implementation of FCS-MPC with long prediction horizon for high-power converter can be explored.

REFERENCES

[1] Wind Europe, “Offshore Wind in Europe - Key trends and statistics 2018,” Wind Europe, Brussels, Belgium, Feb. 2019.

[2] P. Catalan, Y. Wang, J. Arza, and Z. Chen, “A Comprehensive Overview of Power Converter Applied in High-Power Wind Turbine: Key Challenges and Potential Solutions,” *IEEE Trans. Power Electron.*, vol. 38, no. 5, pp. 6169–6195, May 2023.

[3] H. Polinder, J. A. Ferreira, B. B. Jensen, A. B. Abrahamsen, K. Atallah, and R. A. McMahon, “Trends in Wind Turbine Generator Systems,” *IEEE J. Emerg. Sel. Topics Power Electron.*, vol. 1, no. 3, pp. 174–185, Sep. 2013.

[4] R. McKenna, P. Ostman v.d. Leye, and W. Fichtner, “Key challenges and prospects for large wind turbines,” *Renewable and Sustainable Energy Reviews*, vol. 53, pp. 1212–1221, Jan. 2016.

[5] A. Nabae, I. Takahashi, and H. Akagi, “A New Neutral-Point-Clamped PWM Inverter,” *IEEE Trans. on Ind. Applicat.*, vol. IA-17, no. 5, pp. 518–523, Sep. 1981.

[6] Sangyō Ōyō Bumon, Taehan-Chŏn’gi-Hakhoe, and IEEE Industry Applications Society, Eds., *2012 15th International Conference on Electrical Machines and Systems (ICEMS 2012): Sapporo, Japan, 21 - 24 October 2012 ; [proceedings]*. Piscataway, NJ: IEEE, 2012.

[7] T. Bruckner and S. Bernet, “Loss balancing in three-level voltage source inverters applying active NPC switches,” in *2001 IEEE 32nd Annual Power Electronics Specialists Conference (IEEE Cat. No.01CH37230)*, Vancouver, BC, Canada, 2001, vol. 2, pp. 1135–1140.

[8] O. S. Senturk, L. Helle, S. Munk-Nielsen, P. Rodriguez, and R. Teodorescu, “Power Capability Investigation Based on Electrothermal Models of Press-Pack IGBT Three-Level NPC and ANPC VSCs for Multimegawatt Wind Turbines,” *IEEE Trans. Power Electron.*, vol. 27, no. 7, pp. 3195–3206, Jul. 2012.

[9] J. Chivite-Zabalza, I. Larrazabal, I. Zubimendi, S. Aurtenetxea, and M. Zabaleta, “Multi-megawatt wind turbine converter configurations suitable for off-shore applications, combining 3-L NPC PEBBs,” in *2013 IEEE Energy Conversion Congress and Exposition*, Denver, CO, USA, 2013, pp. 2635–2640.

[10] V. Yaramasu and B. Wu, *Model predictive control of wind energy conversion systems*. New York: Wiley, 2017.

[11] J. Holtz and S. Stadtfeld, “A predictive controller for the stator currentvector of ac machines fed from a switched voltage source,” presented at the Proc. Int.Power Electron. Conf., Tokyo, 1983, pp. 1665–1675.

[12] P. Cortes, M. P. Kazmierkowski, R. M. Kennel, D. E. Quevedo, and J. Rodriguez, “Predictive Control in Power Electronics and Drives,” *IEEE Trans. Ind. Electron.*, vol. 55, no. 12, pp. 4312–4324, Dec. 2008.

[13] A. Linder and R. Kennel, “Model Predictive Control for Electrical Drives,” in *IEEE 36th Conference on Power Electronics Specialists, 2005.*, Aachen, Germany, 2005, pp. 1793–1799.

[14] J. Rodriguez *et al.*, “State of the Art of Finite Control Set Model Predictive Control in Power Electronics,” *IEEE Trans. Ind. Inf.*, vol. 9, no. 2, pp. 1003–1016, May 2013.

[15] S. Kouro, P. Cortes, R. Vargas, U. Ammann, and J. Rodriguez, “Model Predictive Control—A Simple and Powerful Method to Control Power Converters,” *IEEE Trans. Ind. Electron.*, vol. 56, no. 6, pp. 1826–1838, Jun. 2009.

[16] S. Vazquez *et al.*, “Model Predictive Control: A Review of Its Applications in Power Electronics,” *EEE Ind. Electron. Mag.*, vol. 8, no. 1, pp. 16–31, Mar. 2014.

[17] G. A. Papafotiou, G. D. Demetriades, and V. G. Agelidis, “Technology Readiness Assessment of Model Predictive Control in Medium- and High-Voltage Power Electronics,” *IEEE Trans. Ind. Electron.*, vol. 63, no. 9, pp. 5807–5815, Sep. 2016.

[18] P. Karamanakos and T. Geyer, “Guidelines for the Design of Finite Control Set Model Predictive Controllers,” *IEEE Trans. Power Electron.*, vol. 35, no. 7, pp. 7434–7450, Jul. 2020.

[19] Z. Zhang, C. M. Hackl, and R. Kennel, “Computationally Efficient DMPC for Three-Level NPC Back-to-Back Converters in Wind Turbine Systems With PMSG,” *IEEE Trans. Power Electron.*, vol. 32, no. 10, pp. 8018–8034, Oct. 2017.

[20] Z. Liu, Z. Xia, D. Li, Y. Wang, and F. Li, “An Optimal Model Predictive Control Method for Five-Level Active NPC Inverter,” *IEEE Access*, vol. 8, pp. 221414–221423, 2020.

[21] T. Geyer and D. E. Quevedo, “Performance of Multistep Finite Control Set Model Predictive Control for Power Electronics,” *IEEE Trans. Power Electron.*, vol. 30, no. 3, pp. 1633–1644, Mar. 2015.

[22] E. Zafra, S. Vazquez, T. Geyer, R. P. Aguilera, and L. G. Franquelo, “Long Prediction Horizon FCS-MPC for Power Converters and Drives,” *IEEE Open J. Ind. Electron. Soc.*, vol. 4, pp. 159–175, 2023.

[23] P. Cortes *et al.*, “Guidelines for weighting factors design in Model Predictive Control of power converters and drives,” in *2009 IEEE International Conference on Industrial Technology*, Churchill, Victoria, Australia, 2009, pp. 1–7.

[24] M. B. Shadmand, S. Jain, and R. S. Balog, “Autotuning Technique for the Cost Function Weight Factors in Model Predictive Control for Power Electronic Interfaces,” *IEEE J. Emerg. Sel. Topics Power Electron.*, vol. 7, no. 2, pp. 1408–1420, Jun. 2019.

[25] L. M. A. Caseiro, A. M. S. Mendes, and S. M. A. Cruz, “Dynamically Weighted Optimal Switching Vector Model Predictive Control of Power Converters,” *IEEE Trans. Ind. Electron.*, vol. 66, no. 2, pp. 1235–1245, Feb. 2019.

[26] F. Villarroel, J. R. Espinoza, C. A. Rojas, J. Rodriguez, M. Rivera, and D. Sbarbaro, "Multiobjective Switching State Selector for Finite-States Model Predictive Control Based on Fuzzy Decision Making in a Matrix Converter," *IEEE Trans. Ind. Electron.*, vol. 60, no. 2, pp. 589–599, Feb. 2013.

[27] C. A. Rojas, S. Kouro, M. Perez, and F. Villarroel, "Multiobjective Fuzzy Predictive Torque Control of an induction machine fed by a 3L-NPC inverter," in *2015 IEEE International Symposium on Predictive Control of Electrical Drives and Power Electronics (PRECEDE)*, Valparaiso, Chile, 2015, pp. 21–26.

[28] D. Zhou, J. Zhao, and Y. Liu, "Online tuning of weighting factors based on sugeno fuzzy method in predictive torque control of four-switch three-phase inverter-fed IM," in *2016 International Symposium on Power Electronics, Electrical Drives, Automation and Motion (SPEEDAM)*, Capri, Italy, 2016, pp. 734–739.

[29] A. M. Bozorgi, H. Gholami-Khesht, M. Farasat, S. Mehraeen, and M. Monfared, "Model Predictive Direct Power Control of Three-Phase Grid-Connected Converters With Fuzzy-Based Duty Cycle Modulation," *IEEE Trans. on Ind. Applicat.*, vol. 54, no. 5, pp. 4875–4885, Sep. 2018.

[30] O. Machado, P. Martin, F. J. Rodriguez, and E. J. Bueno, "A Neural Network-Based Dynamic Cost Function for the Implementation of a Predictive Current Controller," *IEEE Trans. Ind. Inf.*, vol. 13, no. 6, pp. 2946–2955, Dec. 2017.

[31] T. Dragicevic and M. Novak, "Weighting Factor Design in Model Predictive Control of Power Electronic Converters: An Artificial Neural Network Approach," *IEEE Trans. Ind. Electron.*, vol. 66, no. 11, pp. 8870–8880, Nov. 2019.

[32] M. Novak, U. M. Nyman, T. Dragicevic, and F. Blaabjerg, "Analytical Design and Performance Validation of Finite Set MPC Regulated Power Converters," *IEEE Trans. Ind. Electron.*, vol. 66, no. 3, pp. 2004–2014, Mar. 2019.

[33] M. Novak, H. Xie, T. Dragicevic, F. Wang, J. Rodriguez, and F. Blaabjerg, "Optimal Cost Function Parameter Design in Predictive Torque Control (PTC) Using Artificial Neural Networks (ANN)," *IEEE Trans. Ind. Electron.*, pp. 1–1, 2020.

[34] P. R. U. Guazzelli, W. C. de Andrade Pereira, C. M. R. de Oliveira, A. G. de Castro, and M. L. de Aguiar, "Weighting Factors Optimization of Predictive Torque Control of Induction Motor by Multiobjective Genetic Algorithm," *IEEE Trans. Power Electron.*, vol. 34, no. 7, pp. 6628–6638, Jul. 2019.

[35] L. Wang, T. Zhao, and J. He, "Investigation of Variable Switching Frequency in Finite Control Set Model Predictive Control on Grid-Connected Inverters," *IEEE Open J. Ind. Applicat.*, vol. 2, pp. 178–193, 2021.

[36] "IEEE Recommended Practice and Requirements for Harmonic Control in Electric Power Systems," IEEE Std 519-2014 (Revision of IEEE Std 519-1992), Jun. 2014.

[37] M. A. Perez and J. Rodriguez, "Predictive frequency spectrum shaping of currents in a three phase inverter," in *2013 IEEE International Symposium on Sensorless Control for Electrical Drives and Predictive Control of Electrical*

Drives and Power Electronics (SLED/PRECEDE), München, Germany, 2013, pp. 1–5.

[38] A. Calle-Prado, S. Alepuz, J. Bordonau, P. Cortes, and J. Rodriguez, "Predictive Control of a Back-to-Back NPC Converter-Based Wind Power System," *IEEE Trans. Ind. Electron.*, vol. 63, no. 7, pp. 4615–4627, Jul. 2016.

[39] B. Stickan, P. Rutquist, T. Geyer, and M. Diehl, "Spectrum Shaping Methods for Predictive Control Approaches Applied to a Grid-Connected Power Electronics Converter," in *2019 IEEE 58th Conference on Decision and Control (CDC)*, Nice, France, 2019, pp. 5223–5230.

[40] R. P. Aguilera *et al.*, "Selective Harmonic Elimination Model Predictive Control for Multilevel Power Converters," *IEEE Trans. Power Electron.*, vol. 32, no. 3, pp. 2416–2426, Mar. 2017.

[41] M. Aguirre, S. Kouro, C. A. Rojas, J. Rodriguez, and J. I. Leon, "Switching Frequency Regulation for FCS-MPC Based on a Period Control Approach," *IEEE Transactions on Industrial Electronics*, vol. 65, no. 7, pp. 5764–5773, Jul. 2018.

[42] M. Rivera *et al.*, "Modulated model predictive control (M^2PC) with fixed switching frequency for an NPC converter," in *2015 IEEE 5th International Conference on Power Engineering, Energy and Electrical Drives (POWERENG)*, Riga, Latvia, 2015, pp. 623–628.

[43] F. Donoso, A. Mora, R. Cardenas, A. Angulo, D. Saez, and M. Rivera, "Finite-Set Model-Predictive Control Strategies for a 3L-NPC Inverter Operating With Fixed Switching Frequency," *IEEE Trans. Ind. Electron.*, vol. 65, no. 5, pp. 3954–3965, May 2018.

[44] A. Mora, R. Cardenas-Dobson, R. P. Aguilera, A. Angulo, F. Donoso, and J. Rodriguez, "Computationally Efficient Cascaded Optimal Switching Sequence MPC for Grid-Connected Three-Level NPC Converters," *IEEE Trans. Power Electron.*, vol. 34, no. 12, pp. 12464–12475, Dec. 2019.

[45] T. Geyer, N. Oikonomou, G. Papafotiou, and F. D. Kieferndorf, "Model Predictive Pulse Pattern Control," *IEEE Trans. on Ind. Applicat.*, vol. 48, no. 2, pp. 663–676, Mar. 2012.

[46] H.-C. Chen, P.-T. Cheng, X. Wang, and F. Blaabjerg, "A Passivity-Based Stability Analysis of the Active Damping Technique in the Offshore Wind Farm Applications," *IEEE Trans. on Ind. Applicat.*, vol. 54, no. 5, pp. 5074–5082, Sep. 2018.

[47] Y. Wang, X. Wang, F. Blaabjerg, and Z. Chen, "Eigenvalue-based harmonic stability analysis method in inverter-fed power systems," in *IECON 2015 - 41st Annual Conference of the IEEE Industrial Electronics Society*, Yokohama, 2015, pp. 003277–003282.

[48] Y. Wang, X. Wang, F. Blaabjerg, and Z. Chen, "Harmonic resonance assessment of multiple paralleled grid-connected inverters system," in *2017 IEEE 3rd International Future Energy Electronics Conference and ECCE Asia (IFEEC 2017 - ECCE Asia)*, Kaohsiung, Taiwan, 2017, pp. 2070–2075.

[49] J. Sun, "Impedance-Based Stability Criterion for Grid-Connected Inverters," *IEEE Trans. Power Electron.*, vol. 26, no. 11, pp. 3075–3078, Nov. 2011.

[50] L. Harnefors, X. Wang, A. G. Yepes, and F. Blaabjerg, “Passivity-Based Stability Assessment of Grid-Connected VSCs—An Overview,” *IEEE J. Emerg. Sel. Topics Power Electron.*, vol. 4, no. 1, pp. 116–125, Mar. 2016.
[51] B. Wen, D. Boroyevich, R. Burgos, P. Mattavelli, and Z. Shen, “Inverse Nyquist Stability Criterion for Grid-Tied Inverters,” *IEEE Trans. Power Electron.*, vol. 32, no. 2, pp. 1548–1556, Feb. 2017.
[52] X. Wang and F. Blaabjerg, “Harmonic Stability in Power Electronic-Based Power Systems: Concept, Modeling, and Analysis,” *IEEE Transactions on Smart Grid*, vol. 10, no. 3, pp. 2858–2870, 2019.
[53] A. G. Yepes, A. Vidal, J. Malvar, O. Lopez, and J. Doval-Gandoy, “Tuning Method Aimed at Optimized Settling Time and Overshoot for Synchronous Proportional-Integral Current Control in Electric Machines,” *IEEE Trans. Power Electron.*, vol. 29, no. 6, pp. 3041–3054, Jun. 2014.
[54] T. Geyer, P. Karamanakos, and R. Kennel, “On the benefit of long-horizon direct model predictive control for drives with LC filters,” in *2014 IEEE Energy Conversion Congress and Exposition (ECCE)*, Pittsburgh, PA, USA, 2014, pp. 3520–3527.
[55] R. P. Aguilera and D. E. Quevedo, “Predictive Control of Power Converters: Designs With Guaranteed Performance,” *IEEE Trans. Ind. Inf.*, vol. 11, no. 1, pp. 53–63, Feb. 2015.
[56] B. P. McGrath, D. G. Holmes, and T. Lipo, “Optimized space vector switching sequences for multilevel inverters,” *IEEE Trans. Power Electron.*, vol. 18, no. 6, pp. 1293–1301, Nov. 2003.
[57] P. Karamanakos, T. Geyer, and R. Kennel, “On the Choice of Norm in Finite Control Set Model Predictive Control,” *IEEE Trans. Power Electron.*, vol. 33, no. 8, pp. 7105–7117, Aug. 2018.
[58] B. Wu and M. Narimani, *High-power converters and AC drives*, Second edition. Hoboken, New Jersey: Wiley, 2017.
[59] R. Vargas, P. Cortes, U. Ammann, J. Rodriguez, and J. Pontt, “Predictive Control of a Three-Phase Neutral-Point-Clamped Inverter,” *IEEE Trans. Ind. Electron.*, vol. 54, no. 5, pp. 2697–2705, Oct. 2007.
[60] P. Catalan, Y. Wang, Z. Chen, and J. Arza, “Model Predictive Control Strategy for NPC Converter-based Wind Turbine with Switching Frequency Control,” in *2021 IEEE Southern Power Electronics Conference (SPEC)*, Kigali, Rwanda, 2021, pp. 1–7.
[61] J. Pou, R. Pindado, D. Boroyevich, and P. Rodriguez, “Limits of the Neutral-Point Balance in Back-to-Back-Connected Three-Level Converters,” *IEEE Trans. Power Electron.*, vol. 19, no. 3, pp. 722–731, May 2004.
[62] R. Teodorescu, M. Liserre, and P. Rodríguez, *Grid Converters for Photovoltaic and Wind Power Systems*. Piscataway, NJ, USA: Wiley-IEEE Press, 2011.
[63] A. Luna *et al.*, “Grid Voltage Synchronization for Distributed Generation Systems Under Grid Fault Conditions,” *IEEE Trans. on Ind. Applicat.*, vol. 51, no. 4, pp. 3414–3425, Jul. 2015.
[64] M. G. Taul, X. Wang, P. Davari, and F. Blaabjerg, “An Overview of Assessment Methods for Synchronization Stability of Grid-Connected

Converters Under Severe Symmetrical Grid Faults," *IEEE Trans. Power Electron.*, vol. 34, no. 10, pp. 9655–9670, Oct. 2019.
[65] X. Wang, L. Harnefors, and F. Blaabjerg, "Unified Impedance Model of Grid-Connected Voltage-Source Converters," *IEEE Trans. Power Electron.*, vol. 33, no. 2, pp. 1775–1787, Feb. 2018.
[66] J. I. Garcia, J. I. Candela, A. Luna, and P. Catalan, "Grid synchronization structure for wind converters under grid fault conditions," in *IECON 2016 - 42nd Annual Conference of the IEEE Industrial Electronics Society*, Florence, Italy, 2016, pp. 2313–2318.
[67] J. Ignacio Garcia, J. Ignacio Candela, and P. Catalan, "Pre-filtered synchronization structure for grid-connected power converters to reduce the stability impact of PLL dynamics," *IEEE J. Emerg. Sel. Topics Power Electron.*, pp. 1–1, 2020.
[68] VDE-AR-N 4120, "Technical requirements for the connection and operation of customer installations to the high-voltage network (TAB high-voltage)." 2015.
[69] M. Graungaard Taul, X. Wang, P. Davari, and F. Blaabjerg, "Current Reference Generation Based on Next-Generation Grid Code Requirements of Grid-Tied Converters During Asymmetrical Faults," *IEEE J. Emerg. Sel. Topics Power Electron.*, vol. 8, no. 4, pp. 3784–3797, Dec. 2020.
[70] B. Mahamedi, M. Eskandari, J. E. Fletcher, and J. Zhu, "Sequence-Based Control Strategy With Current Limiting for the Fault Ride-Through of Inverter-Interfaced Distributed Generators," *IEEE Trans. Sustain. Energy*, vol. 11, no. 1, pp. 165–174, Jan. 2020.
[71] O. Goksu, R. Teodorescu, C. L. Bak, F. Iov, and P. C. Kjaer, "Instability of Wind Turbine Converters During Current Injection to Low Voltage Grid Faults and PLL Frequency Based Stability Solution," *IEEE Trans. Power Syst.*, vol. 29, no. 4, pp. 1683–1691, Jul. 2014.
[72] I. Erlich, F. Shewarega, S. Engelhardt, J. Kretschmann, J. Fortmann, and F. Koch, "Effect of wind turbine output current during faults on grid voltage and the transient stability of wind parks," in *2009 IEEE Power & Energy Society General Meeting*, Calgary, Canada, 2009, pp. 1–8.
[73] M. G. Taul, X. Wang, P. Davari, and F. Blaabjerg, "Robust Fault Ride-Through of Converter-based Generation during Severe Faults with Phase Jumps," *IEEE Trans. on Ind. Applicat.*, pp. 1–1, 2019.
[74] S. Vazquez, J. Rodriguez, M. Rivera, L. G. Franquelo, and M. Norambuena, "Model Predictive Control for Power Converters and Drives: Advances and Trends," *IEEE Trans. Ind. Electron.*, vol. 64, no. 2, pp. 935–947, Feb. 2017.
[75] J. Rodriguez *et al.*, "Predictive Current Control of a Voltage Source Inverter," *IEEE Trans. Ind. Electron.*, vol. 54, no. 1, pp. 495–503, Feb. 2007.
[76] V. Yaramasu, M. Rivera, B. Wu, and J. Rodriguez, "Model Predictive Current Control of Two-Level Four-Leg Inverters—Part I: Concept, Algorithm, and Simulation Analysis," *IEEE Trans. Power Electron.*, vol. 28, no. 7, pp. 3459–3468, Jul. 2013.
[77] M. Rivera, V. Yaramasu, J. Rodriguez, and B. Wu, "Model Predictive Current Control of Two-Level Four-Leg Inverters—Part II: Experimental

Implementation and Validation," *IEEE Trans. Power Electron.*, vol. 28, no. 7, pp. 3469–3478, Jul. 2013.
[78] W. Yuan, Y. Wang, D. Liu, F. Deng, and Z. Chen, "Impacts of Inductor Nonlinear Characteristic in Multiconverter Microgrids: Modeling, Analysis, and Mitigation," *IEEE J. Emerg. Sel. Topics Power Electron.*, vol. 8, no. 4, pp. 3333–3347, Dec. 2020.
[79] S. Chandar and S. K. Panda, "Degradation Detection and Diagnosis of Inductors in LCL Filter Integrated With Active Front End Rectifier," *IEEE Trans. Power Electron.*, vol. 33, no. 2, pp. 1622–1632, Feb. 2018.
[80] H. A. Young, M. A. Perez, and J. Rodriguez, "Analysis of Finite-Control-Set Model Predictive Current Control With Model Parameter Mismatch in a Three-Phase Inverter," *IEEE Trans. Ind. Electron.*, vol. 63, no. 5, pp. 3100–3107, May 2016.
[81] F. Auger, M. Hilairet, J. M. Guerrero, E. Monmasson, T. Orlowska-Kowalska, and S. Katsura, "Industrial Applications of the Kalman Filter: A Review," *IEEE Trans. Ind. Electron.*, vol. 60, no. 12, pp. 5458–5471, Dec. 2013.
[82] G. Welch and G. Bishop, "An Introduction to the Kalman Filter," *Proc. Siggraph Course*, vol. 8, Jan. 2006.
[83] R. Schneider and C. Georgakis, "How To NOT Make the Extended Kalman Filter Fail," *Ind. Eng. Chem. Res.*, vol. 52, no. 9, pp. 3354–3362, Mar. 2013.
[84] M. Liserre, R. Teodorescu, and F. Blaabjerg, "Stability of photovoltaic and wind turbine grid-connected inverters for a large set of grid impedance values," *IEEE Trans. Power Electron.*, vol. 21, no. 1, pp. 263–272, Jan. 2006.
[85] W. Cao, "Impedance-Based Stability Analysis and Controller Design of Three-Phase Inverter-Based Ac Systems," University of Tennessee, Knoxville, 2017.
[86] B. Wen, D. Boroyevich, R. Burgos, P. Mattavelli, and Z. Shen, "Analysis of D-Q Small-Signal Impedance of Grid-Tied Inverters," *IEEE Trans. Power Electron.*, vol. 31, no. 1, pp. 675–687, Jan. 2016.
[87] M. Cespedes and Jian Sun, "Impedance Modeling and Analysis of Grid-Connected Voltage-Source Converters," *IEEE Trans. Power Electron.*, vol. 29, no. 3, pp. 1254–1261, Mar. 2014.
[88] A. Rygg, M. Molinas, C. Zhang, and X. Cai, "A Modified Sequence-Domain Impedance Definition and Its Equivalence to the dq-Domain Impedance Definition for the Stability Analysis of AC Power Electronic Systems," *IEEE J. Emerg. Sel. Topics Power Electron.*, vol. 4, no. 4, pp. 1383–1396, Dec. 2016.
[89] T. Suntio, T. Messo, and J. Puukko, *Power Electronic Converters. Dynamics and Control in Conventional and Renewable Energy Applications*. Wiley-VCH, 2017.
[90] N. Nise, *Control Systems Engineering*, Seventh Ed. Wiley, 2015.
[91] S. Shah, P. Koralewicz, V. Gevorgian, H. Liu, and J. Fu, "Impedance Methods for Analyzing Stability Impacts of Inverter-Based Resources: Stability Analysis Tools for Modern Power Systems," *IEEE Electrific. Mag.*, vol. 9, no. 1, pp. 53–65, Mar. 2021.
[92] Y. Wang, X. Wang, F. Blaabjerg, and Z. Chen, "Frequency scanning-based stability analysis method for grid-connected inverter system," in *2017 IEEE*

3rd International Future Energy Electronics Conference and ECCE Asia (IFEEC 2017 - ECCE Asia), Kaohsiung, Taiwan, 2017, pp. 1575–1580.
[93] Shen, Zhiyu, "Online Measurement of Three-phase AC Power System Impedance in Synchronous Coordinates," PhD, Virginia Tech, 2013.
[94] Z. Shen, M. Jaksic, P. Mattavelli, D. Boroyevich, J. Verhulst, and M. Belkhayat, "Three-phase AC system impedance measurement unit (IMU) using chirp signal injection," in *2013 Twenty-Eighth Annual IEEE Applied Power Electronics Conference and Exposition (APEC)*, Long Beach, CA, USA, 2013, pp. 2666–2673.
[95] T. Roinila, M. Vilkko, and J. Sun, "Broadband methods for online grid impedance measurement," in *2013 IEEE Energy Conversion Congress and Exposition*, Denver, CO, USA, 2013, pp. 3003–3010.
[96] T. Roinila, M. Vilkko, and Jian Sun, "Online Grid Impedance Measurement Using Discrete-Interval Binary Sequence Injection," *IEEE J. Emerg. Sel. Topics Power Electron.*, vol. 2, no. 4, pp. 985–993, Dec. 2014.
[97] G. Francis, R. Burgos, D. Boroyevich, F. Wang, and K. Karimi, "An algorithm and implementation system for measuring impedance in the D-Q domain," in *2011 IEEE Energy Conversion Congress and Exposition*, Phoenix, AZ, USA, 2011, pp. 3221–3228.
[98] A. Rygg and M. Molinas, "Apparent Impedance Analysis: A Small-Signal Method for Stability Analysis of Power Electronic-Based Systems," *IEEE J. Emerg. Sel. Topics Power Electron.*, vol. 5, no. 4, pp. 1474–1486, Dec. 2017.
[99] Wilsun Xu, E. E. Ahmed, Xiqin Zhang, and Xian Liu, "Measurement of network harmonic impedances: practical implementation issues and their solutions," *IEEE Trans. Power Delivery*, vol. 17, no. 1, pp. 210–216, Jan. 2002.
[100] S. Grivet-Talocia and B. Gustavsen, *Passive macromodeling: theory and applications*. Hoboken, New Jersey: John Wiley & Sons, Inc, 2016.
[101] C. Yoon, H. Bai, R. N. Beres, X. Wang, C. L. Bak, and F. Blaabjerg, "Harmonic Stability Assessment for Multiparalleled, Grid-Connected Inverters," *IEEE Trans. Sustain. Energy*, vol. 7, no. 4, pp. 1388–1397, Oct. 2016.
[102] B. Wen, R. Burgos, D. Boroyevich, P. Mattavelli, and Z. Shen, "AC Stability Analysis and dq Frame Impedance Specifications in Power-Electronics-Based Distributed Power Systems," *IEEE J. Emerg. Sel. Topics Power Electron.*, vol. 5, no. 4, pp. 1455–1465, Dec. 2017.
[103] C. Bartsch, "FACT-SHEET alpha ventus," Accessed: Feb. 1, 2023. [Online]. Available: www.alpha-ventus.de, 2020.
[104] C. Ruiz, G. Abad, M. Zubiaga, D. Madariaga, and J. Arza, "Wind Turbine Oriented Solutions to Improve Power Quality and Harmonic Compliance of AC Offshore Wind Power Plants," *IEEE Access*, vol. 9, pp. 167096–167116, 2021.
[105] C. Ruiz, G. Abad, M. Zubiaga, D. Madariaga, and J. Arza, "Frequency-Dependent Pi Model of a Three-Core Submarine Cable for Time and Frequency Domain Analysis," *Energies*, vol. 11, no. 10, p. 2778, Oct. 2018.

[106] E. Ebrahimzadeh, F. Blaabjerg, X. Wang, and C. L. Bak, “Harmonic Stability and Resonance Analysis in Large PMSG-Based Wind Power Plants,” *IEEE Trans. Sustain. Energy*, vol. 9, no. 1, pp. 12–23, Jan. 2018.
[107] I. Kortazar, “Offshore Wind Power Converter Product Range Up to 18 MW,” Sept. 2023, [Online]. Available: www.ingeteam.com.
[108] E. Sanz, “Robust Firmware Development For Wind Applications Through HiL/SiL Validations,” Sept. 2023, [Online]. Available: www.ingeteam.com.
[109] M. Zabaleta, “Permanent Magnet Multiphase Machine Modeling and Control for MV Wind Energy Applications,” Ph.D. dissertation, Liverpool John Moores Univ., Liverpool, U.K., 2018.
[110] P. Cortes, J. Rodriguez, C. Silva, and A. Flores, “Delay Compensation in Model Predictive Current Control of a Three-Phase Inverter,” *IEEE Trans. Ind. Electron.*, vol. 59, no. 2, pp. 1323–1325, Feb. 2012.
[111] E. Burguete, “Análisis, diseño y control de convertidores multinivel,” Ph.D. dissertation, Universidad Pública de Navarra, Pamplona, Spain, 2016.
[112] “TR 61000-3-6 Electromagnetic compatibility (EMC) - Part 3-6: Limits - Assessment of emission limits for the connection of distorting installations to MV HV and EHV power systems,” 2008.